Montanuniversität Leoben

Atomic-scale characterization of severely deformed nanocrystalline alloys

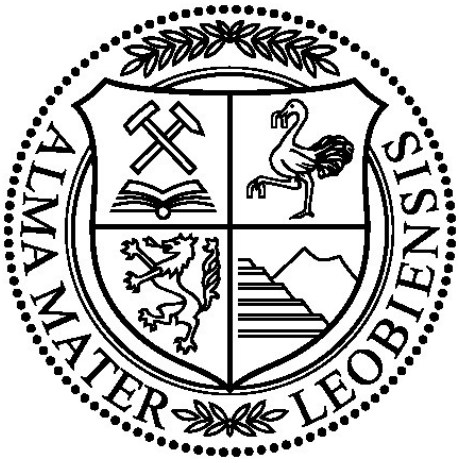

Jinming Guo

Leoben, January 2018

This work was financially supported by the Austrian Science Fund (FWF) under grant P27034 - N20 entitled “Atomic resolution study of deformation-induced phenomena in nanocrystalline materials”.

Erich Schmid Institute of Materials Science
Austrian Academy of Sciences
Jahnstraße 12
A-8700 Leoben

Affidavit

I declare in lieu of oath, that I wrote this thesis and performed the associated research myself, using only literature cited in this volume.

Jinming Guo

Leoben, January 2018

Acknowledgements

I wish to sincerely thank my supervisor Priv.-Doz. Dr. Zaoli Zhang, who gave me the chance to study in Leoben. He conveyed a spirit of genuine enthusiasm in regard to research to me. Without his guidance this dissertation would not have been possible.

In addition, I would like to thank Dr. Julian Rosalie for guiding me on experiments at my initial stage of PhD studies, and cordially thank Prof. Reinhard Pippan for enlightening discussions and his encouragement.

Furthermore, I would like to thank my warm-hearted colleagues at Erich Schmid Institute for their selfless assistance on experiments and fruitful discussions: Andrea Bachmaier, Christoph Gammer, Pradipta Ghosh, Alexander Leitner, Timo Müller, Jozef Keckes, Niraj Chawake, Karoline Kormout and Oliver Renk deserve particular mention. I would also like to thank the technicians: Peter Kutleša, Herwig Felber, Gabriele Felber and Silke Modritsch are gratefully acknowledged for their kind help with the HPT, TEM and metallographic samples preparation.

Thanks are also given to our collaborators: Dr. María Jazmin Duarte and Prof. Gerhard Dehm at Max-Planck Institut für Eisenforschung GmbH in Düsseldorf for APT characterization, Dr. Georg Haberfehlner and Prof. Gerald Kothleitner at Graz University of Technology for STEM EELS mapping experiments, Mr. Lei Li and Prof. Yunbin He at Hubei University, China for XPS measurements and Mr. Yong Zhang at Hunan University, China for DFT calculations.

Finally, I would like to express the deepest appreciation to my family: My mother Dongmei Zhao, my wife Lingjie Zhang, my little daughter Anja Guo and my brother Jinhai Guo. All the support they have provided me over the years was the greatest gift and encouragement for me. My wife, Lingjie has been extremely supportive of me throughout this entire period and has made countless sacrifices to help me to reach this point. During her pregnancy and after the birth of Anja on Mar. 22, 2016, we have overcome extreme difficulties in many aspects of our life. We are growing up as Anja is doing, and she have brought us endless joys and happiness as well as encouragement and definitely will bring more. My mother and brother also deserve special thanks and respect for their continuous support and efforts in China. This journey would not have been possible without their support. Thank you very much.

Jinming Guo

Jan. 1, 2018

Abstract

The usually immiscible composites in thermodynamic equilibrium condition can be forced into a metastable supersaturated state through deformation, which has received enormous scientific attention for the last decades. Severe plastic deformation processing has unique advantages, inducing dissolution of second phases and considerable grain refinement down to nanometer range. The as-generated materials have various processing-induced nanostructural features such as deformation twins, non-equilibrium grain boundaries, dislocation substructures, vacancy agglomerates, solute segregation and clusters. By specifically designing and controlling these features, many nanocrystalline materials show extraordinary mechanical and electrical properties compared to their coarse-grained counterparts.

Despite the extensive studies on nanocrystalline materials, the underlying phenomena are still not well understood at an atomistic scale. For example, the deformation process, mechanism of forced intermixing and influence of light elements on microstructure and properties as well as thermal stabilities are barely reported in literature. To understand these phenomena in nanocrystalline alloys, this thesis mainly include 2 parts on the cases of Cu-Cr and Cu-Fe systems.

In the first part, a dual-phase Cu-Cr composite with different initial phase hardness and ductility was deformed with controllable strains by high pressure torsion. Shear deformation processes were observed at the atomic scale to get insights into the grain refinement and intermixing in the Cu-Cr system at the early stage of deformation. It was found that the hard Cr phase underwent elongation until reaching extremely fine lamellar structures, embedded with 1 – 2 nm thick Cu layers at the phase boundaries. The Cr lamellae then necked and finally fractured via dislocation multiplication, forming almost equiaxed grains with saturated average size of 13.7 nm and reaching stable hardness of 480 – 495 HV after deformation to a strain of 1360. In addition, the dissolved Cu was surprisingly observed as nanoclusters with dimensions of about 2 nm inside the Cr grains, with Cu maintaining a body-centered cubic structure. The phase fraction change associated with Cu dissolution into Cr matrix during continuous deformation was measured and accurately calculated, indicating a negative exponential phase change mode.

In the second part, Cu-Fe was mechanically alloyed directly from blended powders and from vacuum arc-melted bulk respectively which contain different contents of oxygen impurity, by means of high pressure torsion. All investigated compositions formed single-phase face-centered cubic supersaturated solid solutions after extremely straining, reaching strain-saturated states. The comparative investigations on a series of Cu-Fe nanocrystalline alloys reveal that oxygen facilitates grain refinement and lattice expansion, which in turn gives rise to higher hardness and poor ductility. Theoretical calculations indicate that the higher twin density in powder samples can be

attributed to the reduction in stacking fault energy by oxygen, resulting in a mixed deformation mechanism.

The behavior of oxygen during *in-situ* heating of highly-strained Cu-Fe powder alloys was investigated. Contrary to expectations, oxide formation occurred prior to the decomposition of the metastable Cu-Fe solid solution. This oxide formation commenced at relatively low temperatures, forming nano-sized clusters of firstly CuO and later Fe_2O_3.

In summary, this thesis revealed the related deformation-induced phenomena and mechanisms at the atomic scale by taking use of the advanced transmission electron microscopy, and gained insights into the oxygen's behavior in severely deformed nanocrystalline alloys. The findings provided the direct observations of oxide formation and offered a pathway for the design of nanocrystalline materials strengthened by oxide dispersions.

Kurzfassung

Komposite aus im thermodynamischen Gleichgewicht üblicherweise unlöslichen Elementen können durch Verformung in einen metastabilen übersättigten Zustand gezwungen werden. Dieses Phänomen hat in den letzten Jahrzehnten enorme Aufmerksamkeit in der Wissenschaft erregt. Verfahren der Hochverformung haben einzigartige Vorteile, zum Beispiel die Auflösung von Zweitphasen und eine erhebliche Kornfeinung bis in den Nanometer-Bereich. Die auf diese Weise hergestellten Nanostrukturen weisen einige charakteristische Merkmale auf, wie zum Beispiel Verformungszwillinge, Ungleichgewichtskorngrenzen, Versetzungsstrukturen, Leerstellenagglomerate, Segregation gelöster Elemente und Cluster. Spezielles Design und Kontrolle dieser Merkmale ermöglichen die Herstellung vieler nanokristalliner Materialien mit außergewöhnlichen mechanischen und elektrischen Eigenschaften im Vergleich zu ihren grobkörnigen Pendants.

Trotz intensiver Studien an nanokristallinen Materialien sind die zugrundeliegenden Phänomene auf atomarer Ebene nur unzureichend verstanden. Beispielsweise werden auftretende Verformungsprozesse, Mechanismen der Zwangsübersättigung, der Einfluss leichter Elemente sowie die thermische Stabilität in der Literatur kaum behandelt. In der vorliegenden Arbeit wurden diese Phänomene anhand zweier Modelsysteme, Cu-Cr und Cu-Fe, untersucht.

Im ersten Teil wurde ein zwei-phasiger Cu-Cr Komposit, mit unterschiedlicher Härte und Duktilität der ursprünglichen Phasen, mit Hochdrucktorsionsverformung kontrolliert verformt. Prozesse in der Anfangsphase der Scherverformung wurden auf atomarer Ebene untersucht um neue Erkenntnisse bezüglich Kornfeinung und Vermischung zu erlangen. Dabei zeigt sich, dass die härtere Cr-Phase eine längliche Struktur formt, bis sich ein extrem feines lamellares Gefüge, mit 1 – 2 nm dicken Cu-Lagen an den Korngrenzen, einstellt. Anschließend beginnen sich die Cr-Lamellen einzuschnüren bis sie letztendlich brechen. In Folge dieses Verfeinerungsprozesses stellt sich nach einer aufgebrachten Dehnung von 1360 ein globulares Sättigungsgefüge mit einer mittleren Korngröße von 13.7 nm und einer Härte von 480 – 495 HV ein. Die Cu-Phase lag überraschenderweise als Cluster (~2 nm) in den Cr-Körner vor und wies eine kubisch raumzentrierte Struktur auf. Die Änderung des Phasenanteils aufgrund der sukzessiven Lösung von Cu Atomen in der Cr-Matrix während der Verformung wurde gemessen und präzise berechnet.

Der zweite Teil beschäftigt sich mit hochverformten Cu-Fe Legierungen, die entweder direkt durch mechanisches Legieren von Reinelement-Pulvern oder schmelzmetallurgisch im Vakuumlichtbogenofen hergestellt wurden. Die Legierungen enthalten unterschiedliche Sauerstoffanteile, bilden jedoch alle kubisch flächenzentrierte übersättigte Mischkristalle in Sättigungsbereich der Verformung. Die Untersuchungen haben gezeigt, dass Sauerstoff Kornfeinung und Gitterausdehnung begünstigt, das führt wiederum zu höherer Härte und geringer Duktilität. Theoretische

Berechnungen deuten darauf hin, dass die höhere Dichte an Zwillingen in Pulverproben auf die verringerte Stapelfehlerenergie zurückzuführen ist.

Das Verhalten des Sauerstoffs wurde zusätzlich während *in-situ* Heizversuchen untersucht. Entgegen der Erwartungen wurden zuerst Oxide gebildet, bevor eine Entmischung des metastabilen Cu-Fe Mischkristalls auftrat. Die Oxidbildung begann bereits bei relativ niedrigen Temperaturen und bildete dabei nm-große CuO Cluster gefolgt von Fe_2O_3.

Diese Arbeit konnte den Zusammenhang zwischen verformungsinduzierten Phänomenen und Mechanismen auf atomarer Ebene zeigen, indem modernste transmissionselektronmikroskopische Untersuchungsmethoden eingesetzt wurden. Damit konnten völlig neue Erkenntnisse über das Verhalten von Sauerstoff in hochverformten nanokristallinen Legierungen gewonnen werden. Dieses Wissen ermöglicht die direkte Beobachtung von Oxidbildung und bietet neue Wege für das Design nanokristalliner dispersionsverstärkter Materialien.

Contents

1

Introduction and Aim of the Thesis

1.1 Processing nanocrystalline materials via severe plastic deformation

Next-generation high-performance structural materials are required for lightweight design strategies and advanced energy applications. These constantly increasing demands have motivated extensive studies on nanocrystalline materials in the last decades due to their excellent properties compared to their coarse-grained counterparts. The production of nanostructured materials can be realized by processing methods such as rapid quenching, thin film deposition or severe plastic deformation (SPD). To make use of them in structural applications, bulk nanocrystalline materials are requested, which can be easily achieved by SPD techniques.

Among the procedures devised for grain refinement, SPD techniques are of particular interest and can effectively generate novel metallic nanocrystalline materials by drastically refining and alloying normally immiscible composites. These techniques enjoy great popularity owing to their ability to produce considerable grain refinement in fully dense, bulk-scale workpieces, thus giving promise for structural applications. The achievable grain sizes lie within the submicrometer (100 – 1000 nm) and nanometer (< 100 nm) ranges. Several comprehensive reviews have focused on various SPD processing techniques, high pressure torsion (HPT), equal-channel angular pressing, accumulative roll-bonding, high energy ball milling, and so on [1–7].

In this thesis, I mainly fabricate the nanocrystalline materials by high pressure torsion, so the emphasis will be put on this technique in the following sections. HPT refers to the processing of metals whereby samples are subjected to a compressive force and concurrent torsional straining. The scientific origin of processing by HPT can actually be traced to a paper, written by P. W. Bridgman in 1943, entitled “On Torsion Combined with Compression” [8].

However, processing by HPT became of major importance only within the last 20 years when it was recognized that this metal forming process provides an opportunity for achieving exceptional grain refinement, often to the nanometer level, and the exceptionally high strength [2].

The modern HPT process is depicted schematically in Fig. 1, where a disk is held between anvils and strained in torsion under the applied pressure of several GPa. A lower holder rotates and surface friction forces deform the disk by shear. Due to the specific geometric shape of the sample, the main volume of the material is strained in conditions of quasihydrostatic compression under the applied pressure. The equivalent strain ε_{eq} is calculated by equation (1) [2]:

$$\varepsilon_{eq} = \frac{2\pi r \cdot N}{t \cdot \sqrt{3}} \tag{1}$$

where r is the radial distance from center of the disk. t is the thickness of the deformed sample.

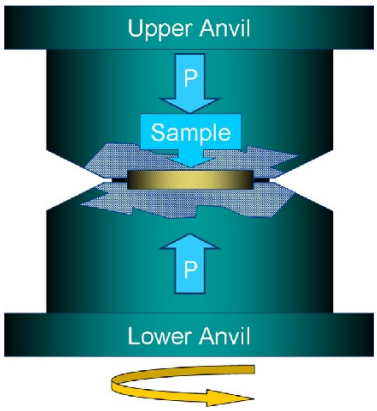

Fig. 1 Schematic diagram of the HPT process [9].

Confined by the principle of the HPT process, there are several fundamental parameters of HPT process: variation in homogeneity across an HPT disk, influence of the applied load on microstructural evolution, influence of the number of rotations and thus the imposed strain and influence of strain hardening and dynamic recovery [2]. An important limitation in HPT is that the imposed strain varies across the sample and, in principle at least, the strain remains at zero at the disk center. As a consequence of this variation, it is reasonable to anticipate that the microstructures produced by HPT will be extremely inhomogeneous as shown in Fig. 2. The total imposed strain, as measured by the number of rotations, is also an important factor in processing by HPT.

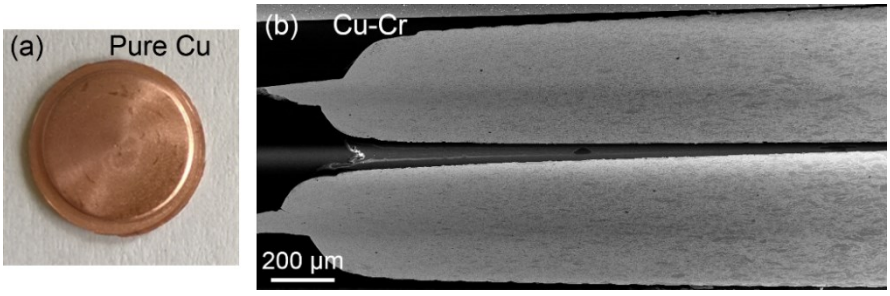

Fig. 2 (a) HPT deformed pure Cu disk. (b) Cross-section graph of HPT-deformed Cu-Cr sample.

1.2 Grain refinement and forced chemical intermixing

How crystal grains deform in a material under stress is important both scientifically, for the understanding of plastic flow in solids, and technologically, for its direct effect on the material strength. Grain size plays an important part: in polycrystals with grain sizes in the micrometer range, strength increases with decreasing grain size. This is known as the Hall-Petch effect [10], and was first explained in terms of the piling up of dislocations, created by the shearing of crystal planes in each grain, at the grain boundaries. As the grains become smaller, the effect of dislocation blocking increases, thereby strengthening the material. The Hall-Petch equation is effective until the grain sizes decreasing to a few nanometers. Fig. 3 shows the schematic diagram of variation of strength with grain size for metals.

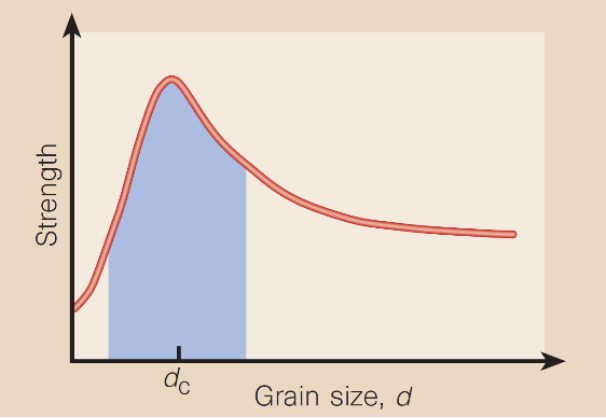

Fig. 3 Variation of strength with grain size for metals. For grain sizes of a few nanometers (region shaded blue), strength first increases and then decreases with decreasing grain size [11].

Although in some cases of nanocrystals with grains in the nanometer range softening phenomenon was observed, for nanocrystalline alloys generated by SPD, it is usually difficult to obtain grains within this scale because the simultaneous recovery process is always accompanying with the grain refinement. Grains are in a dynamic balance between the continuous refinement and attendant recrystallization during SPD, namely, a competition between hardening rate introduced by dislocation generation and the recovery rate arising from dislocation annihilation and recombination.

There exist different micromechanisms proposed for grain refinement in literature. Stacking fault energy (SFE), solid solution hardening and grain boundary migration theories are each supported by different reports and it is still under debates which one dominates the grain refinement process during SPD [5,12–19]. Some reports argue that SFE determines the separation of partial dislocations (Shockley partials and Frank partials with a stacking fault ribbon between them) and thus, influences the dislocation mobility. During plastic deformation, a high SFE (e.g. in Al, Ni, Cu) strongly confines the separation of partial dislocations that facilitates cross-slip to form three dimensional dislocation substructures like cells or subgrains. On the other hand, a large spacing of partial dislocations due to a low SFE (e.g. in Ag) inhibits cross-slip and causes dislocations to arrange themselves in planar arrays. A high plastic strain promotes deformation twinning in low SFE materials [15].

However, some reports suggest that the steady-state grain size is not controlled by the SFE but by atomic-size and modulus mismatch effects of solutes, which control the mobility of edge dislocations [16,19]. For alloys, solute atoms play a role in enhancing the shear stress required for dislocation movement. Labusch suggested a model calculating the shear stress change $\Delta\tau$ based on the atomic size mismatch ε_b and the modulus mismatch ε'_G [20]:

$$\Delta\tau = \frac{G\left[\varepsilon'^{2}_{G}+(15\varepsilon_b)^2\right]^{2/3}c^{2/3}}{\varphi} \quad (2)$$

where G is the shear modulus, c is the solute concentration, $\varphi = 550$ for *fcc* alloys. According to this equation, Edalati *et al*. plotted the steady-state grain size against the term of the influence of atomic size mismatch and modulus mismatch [19], and found a tendency for a decrease of the steady-state grain size with the increasing shear stress.

Another theory is grain boundary migration, which has been observed experimentally, controls the size and shape of grains in the saturation regime [17]. It is known that in the strain saturation regime, the generation of defects, i.e., dislocations, vacancies, and new boundaries, has to be in equilibrium with the annihilation of these defects, which indicates that the continuous refinement rate is equivalent to that of recovery process. Grain boundary migration during deformation embodies the so-called recovery process, which limits further grain refinement during SPD. Segregation at grain boundaries is an effective measure to lower grain boundary energy, and in turn limit grain boundary migration, which is usually called pining of grain boundaries. By appropriate decoration of the grain boundaries, nanocrystalline materials can be engineered to achieve specific microstructures and resultant properties.

It has been documented that grain boundary impurities have a dramatic effect on the stability, strength and ductility of nanocrystalline metals and alloys. Usually grain boundary migration is the dominant process responsible for the limitation in grain refinement by SPD [17]. Therefore, second-phase particles in the nanometer scale can effectively stabilize even finer microstructures. Light elements like oxygen atoms can pin the boundaries, preventing stress-assisted grain growth and resulting in reduced steady-state grain size with increased strength and loss in ductility [21]. The oxygen enrichment at grain boundaries serves to decrease the grain boundary energy γ, as described by Gibbs' adsorption equation [22]:

$$d\gamma = -\Gamma d\mu_{sol.} \quad (3)$$

where Γ is the solute coverage on the grain boundary plane, $\mu_{sol.}$ is the chemical potential of the solute. Eq. (3) can be rewritten in the dilute limit in terms of the solute concentration in the lattice c and the enthalpy of segregation (enrichment) $\Delta H_{seg.}$ as [21,23]:

$$\gamma = \gamma_0 - \Gamma(RT\ln c + \Delta H_{seg.}) \quad (4)$$

where γ_0 is the grain boundary energy of the pure solvent, R is the ideal gas constant, and T is the temperature. Eq. (4) demonstrates the decrease of γ from γ_0 with increasing solute enrichment at the grain boundary, allowing for $\gamma \leq 0$ with sufficiently high combinations of $\Delta H_{seg.}$ and/or Γ. In a nanocrystalline system with solute enrichment at the grain boundary, grain growth would establish a competition between the energy loss due to decreasing grain boundary area and the energy gain owing to the banishment of solutes to the lattice caused by decreased enrichment sites [23]. Therefore, a metastable equilibrium will exist with $\gamma = 0$, which corresponds to a particular grain size, $\Delta H_{seg.}$ and Γ.

Forced chemical intermixing is a concurrent process accompanied with grain refinement during SPD. Various explanations were suggested to understand forced chemical mixing

during co-deformation of phases consisting of non-soluble elements. The first one assumes a purely diffusion-driven mechanism [24,25]. The second one assumes defect-enhanced diffusion (dislocations, vacancies) [26]. The third one is mainly built on interface roughening and plasticity-driven mechanical mixing via shear transfer (dislocations, shear bands) across heterophase interfaces, which is also referred to as dislocation shuffling [27,28].

Many theoretical calculations have discussed the forced mixing under deformation. Shear-induced mixing in heterogeneous Cu alloy systems has been investigated by molecular dynamics simulation [29–31]. The systems comprise single spherical particles within Cu matrices, and are subjected to cyclical shearing as shown in Fig. 4 for strains of $\varepsilon = 6$ and $\varepsilon = 60$ respectively. It was noted that both *fcc* and *bcc* spherical particles become oriented in Cu under prolonged shear deformation. For Cu, Ag, Ni and Fe this alignment enables dislocations to transfer from the Cu matrix to the particle. Mixing in this case can be described as superdiffusive, where the mixing rate depends on the square of the particle radius and not linearly, as would be expected for a diffusive process. Most of the new bonds created during the early stages of mixing are due to distortion of the shape of the particle and the increase in interface area, rather than mixing across the interface. For V and Nb particles a quite different behavior is observed. Dislocations do not transfer across the interface and the particles maintain their initial shape. Pile-up of dislocations at the interfaces, however, results in local relaxations that induce mixing between the particle and matrix. This process results in diffusive mixing, with mixing rate increasing linearly with particle radius. For the Nb particle the introduction of Nb atoms into Cu results in an amorphous shell surrounding the particle.

A consequence of superdiffusive mixing behavior, as described in literature [30,31], is that the number of atoms leaving a precipitate of radius R per unit strain is proportional to R^2 rather than R, which is the case for diffusive processes. Accordingly, the characteristic plastic strain required to dissolve a monodisperse distribution of spherical particles in the absence of thermal diffusion is [30,32]:

$$\Delta\varepsilon = \frac{16}{3}\frac{c_{\mathrm{B}}(1-c_{\mathrm{B}})}{V_{\mathrm{p}}}\frac{R}{b} \tag{5}$$

where c_{B} is the concentration of solute B, V_{p} is the volume fraction of precipitates and b is the Burgers vector.

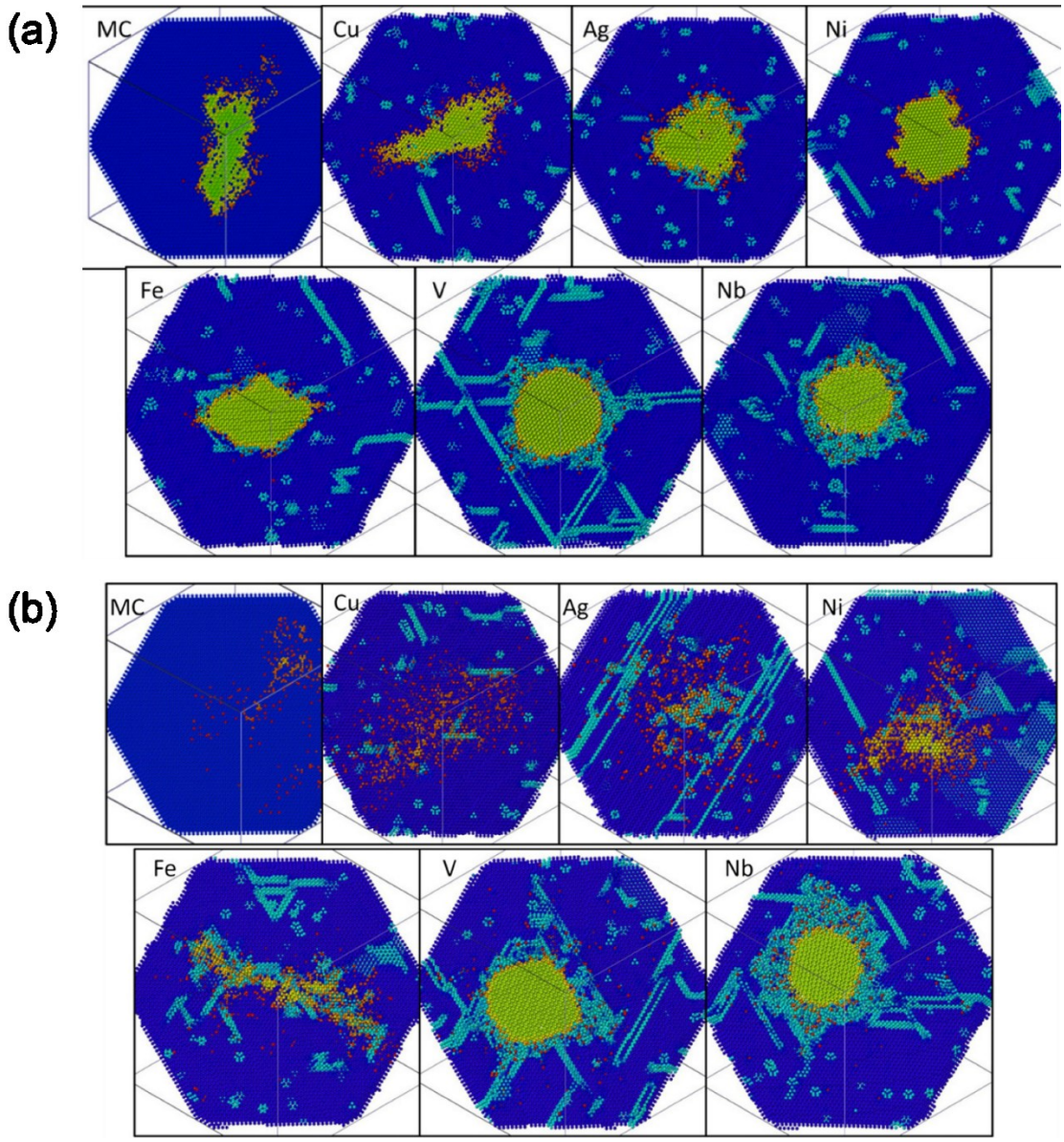

Fig. 4 Morphology of spherical particles in Cu after strains of (a) 6.0 and (b) 60. The left-most configuration is from a Monte Carlo (MC) simulation of a Cu precipitate in a Cu matrix. The rest of the configurations are from molecular dynamics (MD) simulations of precipitates in a Cu matrix. The particle material is indicated in each panel [31].

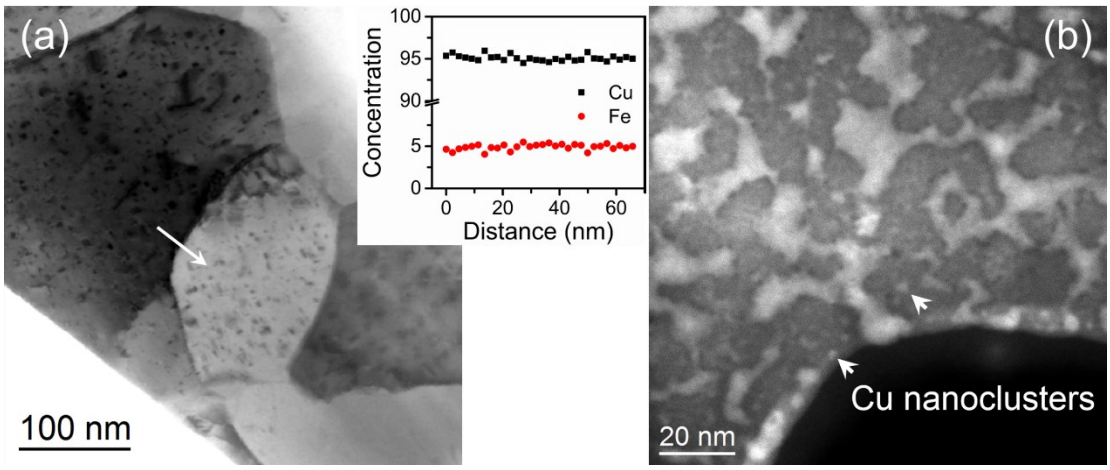

Fig. 5 (a) Transmission electron microscopy (TEM) bright field (BF) image of as-deformed 95 at.%Cu - 5 at.%Fe alloy. The top-right graph shows the energy-dispersive X-ray spectroscopy (EDXS) plots of Cu and Fe respectively along the white arrow line in the image. (b) High angle annular dark field (HAADF) image of as-deformed 57 wt.%Cu - 43 wt.%Cr alloy. The bright area represents Cu phase while the dark area is Cr phase.

As exemplified in Fig. 5, the typical intermixing in immiscible Cu-Fe and Cu-Cr systems are shown. The energy-dispersive X-ray spectroscopy (EDXS) plots of Cu and Fe show the 5 at.%Fe is homogeneously dissolved into the Cu matrix. For the as-deformed 57 wt.%Cu - 43 wt.%Cr alloy, some Cu nanoclusters with sizes of 2 nm are detected inside Cr grains. The detailed discussion on the grain refinement as well as intermixing for both Cu-Fe and Cu-Cr alloys will be presented in following publications.

1.3 A brief introduction to aberration-corrected high resolution transmission electron microscopy

In this thesis, the transmission electron microscope (TEM) is employed to investigate the related phenomena at the atomic scale. In 1931, Max Knoll and Ernst Ruska demonstrated a microscope using electron illumination with magnetic lenses, and their development of a real sense of a working TEM in 1933 showed a greater resolution than that of light. After that, the first commercial TEM came out in 1939, and the rapid development of TEM has strongly facilitated research in different fields. However, the resolution d is still limited by the wavelength of electrons λ and different aberrations, such as spherical aberration C_S and chromatic aberration C_C as shown in the following equation:

$$d = \frac{0.61\lambda}{\alpha} + {C_S}^{1/4} \cdot \lambda^{3/4} + C_C\left(\frac{\Delta E}{E}\right) + \cdots \quad (6)$$

where α is the aperture semi-angle, and the ΔE is the variation of the electron energy E. From this equation, we can see there are two solutions to enhance the resolution: one is to decrease the electron wavelength λ, in other words, to increase the high voltage; another one is to minimize the aberrations.

JEOL (Japan) company produced a high-voltage electron microscope with accelerating voltage of 1.25 MeV. Although it significantly improved the resolution, such high-voltage microscopes were not widely popularized due to its cost, huge size, and strong irradiation damage. However, in late 1990s, a double-hexapole system was constructed which permits to correct the spherical aberration of the objective lens [33,34]. By appropriately exciting the hexapole elements, it is possible to adjust the spherical aberration coefficient to give specific values of the combined system (consisting of objective lens and corrector element) ranging between the aberration value of the original uncorrected instrument over zero towards negative values [35,36]. Tuning the spherical aberration C_S to negative values, results in a novel imaging technique, which is called the negative C_S imaging technique. For the case of thin objects negative C_S images are superior to positive C_S images concerning the magnitude of the obtained contrast, which is due to constructive rather than destructive superposition of fundamental contrast contributions. As a consequence, the image signal obtained with a negative spherical aberration is significantly more robust against noise caused by amorphous surface layers, resulting in a measurement precision of atomic positions which is by a factor of 2–3 better at an identical noise level [37].

Another benefit of C_S-corrected microscope is that the delocalization can be essentially removed and the interface is atomically sharp if the image is taken in the aberration-corrected state at Scherzer defocus [34]. In addition, using an imaging mode based on the adjustment of a negative value of the C_S coefficient of the objective lens of a TEM, it is possible to view the light elements, such as oxygen, nitrogen atoms which, due to their low scattering power, are not previously accessible in conventional microscope, and this allows us to detect local nonstoichiometries or the degree of oxygen-vacancy ordering [38]. All these benefits make the investigation of nanocrystalline alloys at the atomic scale possible.

1.4 Aim of the thesis

As mentioned in previous sections, the atomic-scale deformation process, mechanism of forced chemical intermixing, and influence of light elements or impurities on microstructure and properties as well as thermal stabilities are still not well understood. With the advent of new TEM techniques, the possibility to solve these issues appears. In this thesis, by using the advanced high resolution TEM (HRTEM) and scanning transmission electron microscopy (STEM), we tend to understand some critical phenomena in Cu-Cr and Cu-Fe nanocrystalline alloys at the atomic scale.

First, I deform the dual-phase Cu-Cr composite with controllable strains by high pressure torsion, ranging from strain of 3.4 to more than 4000. With the technique of X-ray diffraction (XRD), the microstructural evolution is detected, such as changes of phase volume, lattice parameter, dislocation density and domain size. Furthermore, the atomic-scale characterizations based on HRTEM, STEM and EDXS, reveal the deformation process and concurrent chemical intermixing. The systematical experiments provide insights into the atomic-scale deformation mechanism as well as the relationship between the dissolution process and applied strain of such ductile-brittle system.

Second, normally immiscible Cu-Fe system was mechanically alloyed directly from blended powders and vacuum arc-melted bulk respectively which contain different levels of content of oxygen impurity, by means of high pressure torsion. By comparing these two systems on aspects of grain size, lattice parameter, twin density and mechanical properties, the oxygen-mediated deformation and grain refinement mechanism is revealed.

In addition, the behavior of oxygen during *in-situ* heating of highly-strained single phase Cu-Fe powder alloys is closely investigated. Nano-sized oxides formation and Fe decomposition of supersaturated solutions are observed at the atomic scale. The finding of oxides formation in single-phase Cu-Fe composites could offer a pathway for the design of nanocrystalline materials strengthened by oxide dispersions.

2

Summary of the Experimental Results

2.1 Cu-Cr system

The 57 wt.%Cu - 43 wt.%Cr composite is deformed by high pressure torsion with controllable strains, ranging from a relatively low strain of 3.4 to extremely high strain of more than 4000. For severely deformed Cu-Cr alloys, the systematical investigation of the dissolution process with the change of applied strain exhibits a negative exponential relationship for immiscible systems via HPT. With the technique of XRD, at the initial deformation stage with low strains, the microstructural evolution is detected, i.e., the changes of phase volume, lattice parameter, dislocation density and domain size. In addition, HRTEM and STEM images reveal the grain refinement and intermixing processes at the atomic scale. The detailed experimental results will be presented in the following two sections.

2.1.1 Microstructural evolution and dissolution process

A commercial coarse-grained 57 wt.%Cu - 43 wt.%Cr bulk material is HPT deformed at room temperature with air cooling. Disks with a diameter of 8 mm and an initial thickness of about 1.0 mm are HPT-deformed with different numbers of rotations N (N = 25, 50, 100, 300, 420, 1000) under a constant pressure of 7.3 GPa and a rotation speed of 0.4 rotation/min.

Fig. 6a shows the fine scanning XRD patterns of 57 wt.%Cu - 43 wt.%Cr raw material and deformed samples with different numbers of rotations, and the peaks of (111) for face-centered cubic (*fcc*) and (110) for body-centered cubic (*bcc*) are separated from the measured curves (black) by accurate fitting with residual value less than 2%. The final overall fitted curve (red) agrees well with the measured curve. Fig. 6b shows the relative intensity ratio of $(111)_{fcc}$ and $(110)_{bcc}$ calculated based on integrated area of each corresponding peak after subtracting the background. The relative intensity ratio of $(111)_{fcc}$ decreases from 0.71 for raw bulk material to 0.38 for the sample deformed with 300 rotations. It then remains constant even the sample is deformed further to 1000 rotations. The relative intensity ratio of $(110)_{bcc}$ increases quickly

when the sample is deformed with the first 100 rotations, and then this value tends to stabilize at the level around 0.62. Based on the principle that the integrated intensity of diffraction peak for each phase in a mixture is proportional to the volume fraction of that phase [39,40], dissolved Cu content at each strain condition can be obtained by comparing the calculated relative intensity ratio with the values of standard blended Cu-Cr powders of different compositions, which is shown in Fig. 6c. The curve shows an obvious negative exponential change mode, with an approaching value of 32 wt.%, indicating the solubility limit of Cu in Cr by HPT is 32 wt.%.

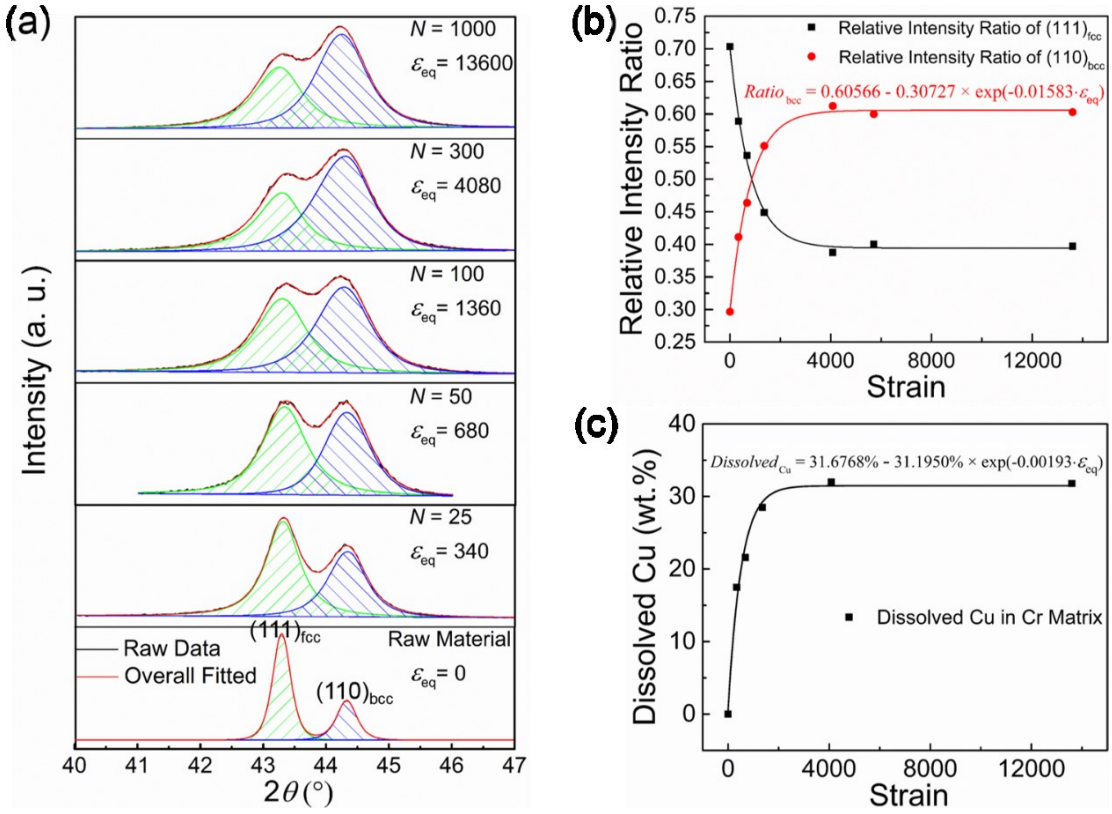

Fig. 6 Phase evolution of HPT deformed samples. (a) XRD patterns of 57 wt.%Cu - 43 wt.%Cr raw material and as-deformed samples with different numbers of rotations in the range of 40˚ – 47˚. (b) Relative intensity ratio changes of $(111)_{fcc}$ and $(110)_{bcc}$ peaks. (c) Dissolved Cu content change as a function of applied strain.

Fig. 7a shows the grain size distribution of Cu-Cr alloys deformed with different numbers of rotations. Fig. 7b exhibits the change of the average grain size with an error bar showing the standard deviation. The average grain size of sample deformed with 25 rotations is 19.5 nm with a relatively wide distribution compared to the sample deformed with 300 rotations with an average grain size of 13.7 nm and a narrower distribution. The grain size change indicates that grain refinement is finished at the initial stage of deformation. Due to the nearly same volume amount of Cu and Cr in this composition of 57 wt.%Cu - 43 wt.%Cr, grinding of each part during HPT deformation is easy to proceed in spite of the large difference of hardness

between Cu and Cr, rather than "swimming" in some compositions with a large proportion of Cu and a little part of Cr.

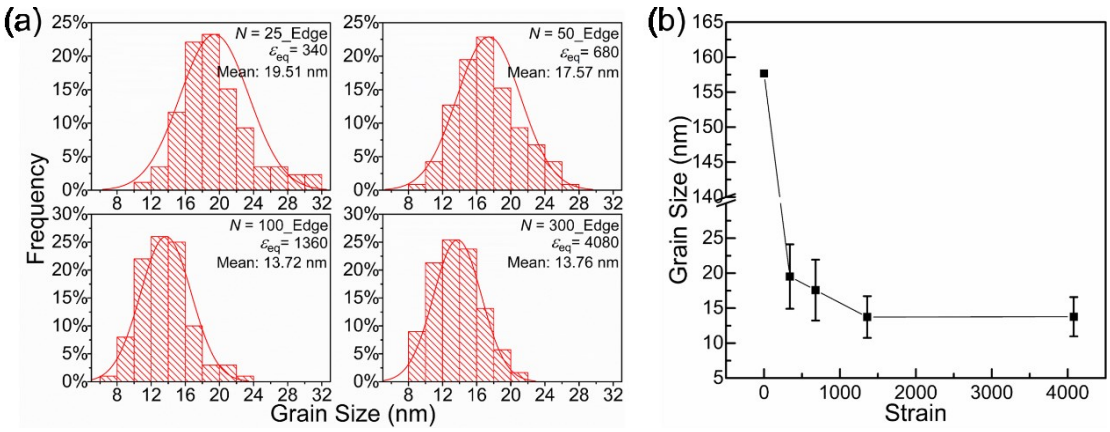

Fig. 7 (a) Histogram distributions of grain size statistics of Cu-Cr alloys deformed with different numbers of rotations. Each histogram is based on measurements of a minimum of 100 grains. (b) Average grain size values of samples deformed with different numbers of rotations with error bar showing standard deviation.

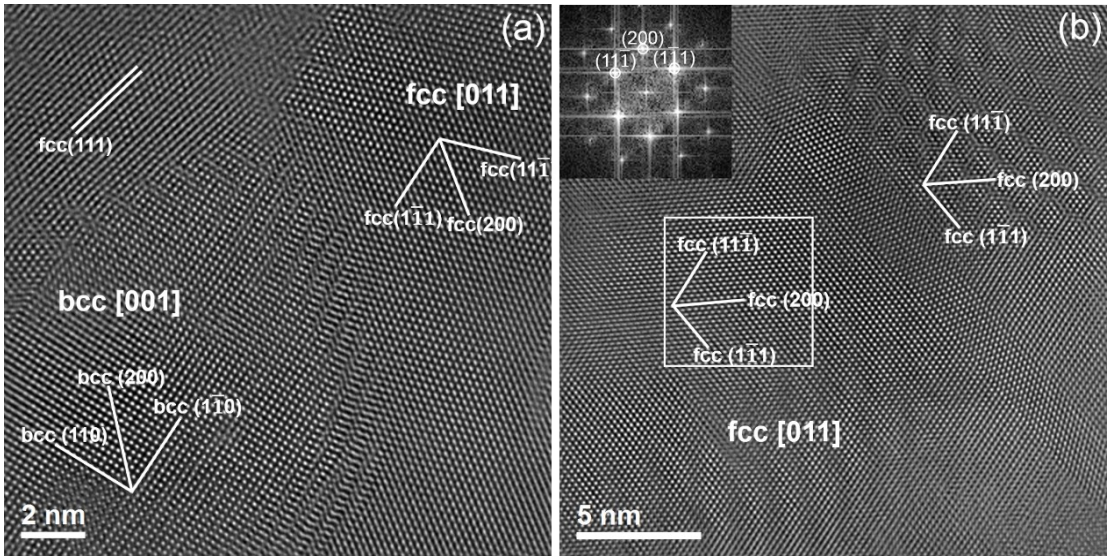

Fig. 8 HRTEM images of 57 wt.%Cu - 43 wt.%Cr alloys after HPT deformation with 100 rotations. (a) Three adjacent grains of Cu and Cr viewed along different zone axes. (b) Nanotwins in a *fcc* grain on zone axis of $[011]_{fcc}$.

Many atomic-scale features unique to nanocrystalline alloys are detected by HRTEM. Fig. 8a shows three adjacent grains of Cu and Cr viewed along different zone axes. The grain at right-hand side is Cu with *fcc* structure and on zone axis of $[011]_{fcc}$ which is parallel to the incident electron beam while the bottom-left grain is Cr with *bcc* structure and on zone axis of

$[001]_{bcc}$. In this image, $(1\bar{1}0)_{Cr}$ plane of Cr grain is strictly parallel to $(1\bar{1}1)_{Cu}$ plane of Cu grain. The top-left grain is Cu with $\{111\}_{Cu}$ planes visible. Fig. 8b shows an atomic-scale twin boundary on a zone axis of $[011]_{fcc}$.

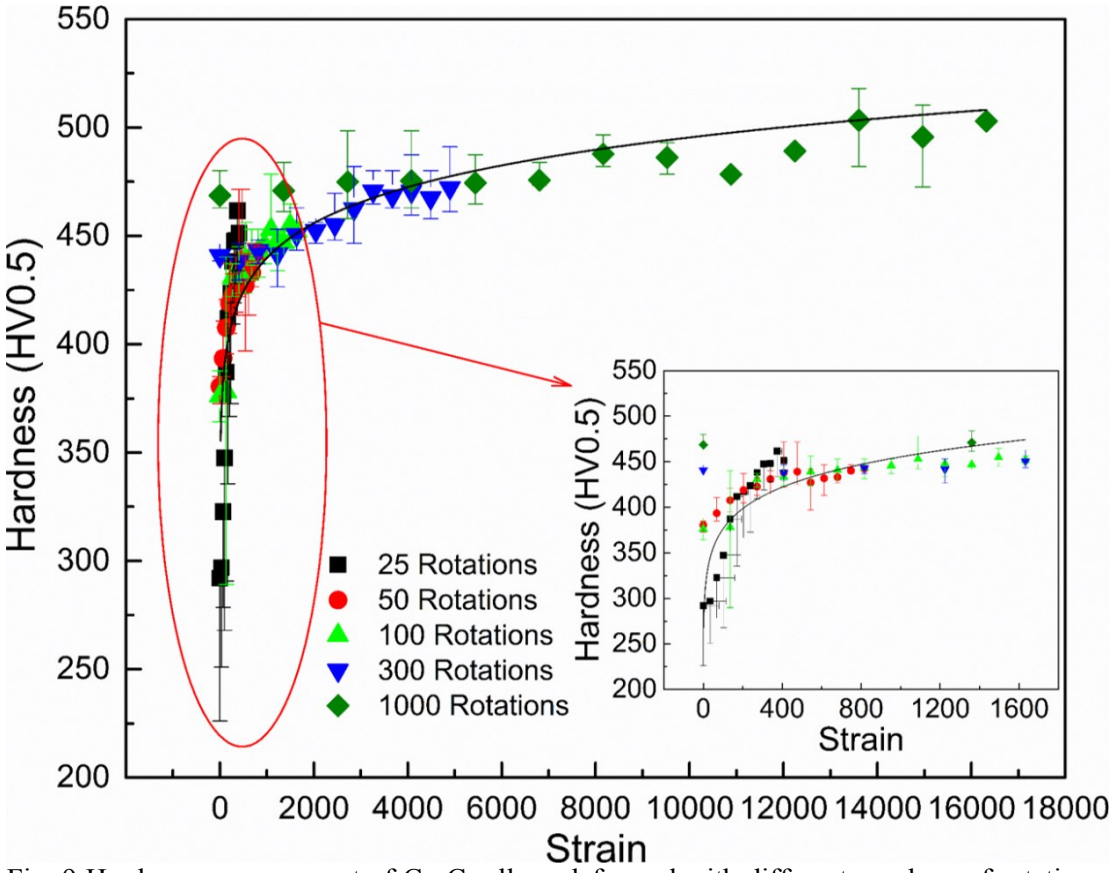

Fig. 9 Hardness measurement of Cu-Cr alloys deformed with different numbers of rotations. The inset shows the enlarged hardness result within a strain range of 0 – 1800.

The hardness of Cu-Cr alloys deformed with different numbers of rotations is measured systematically as shown in Fig. 9. The inset shows the enlarged hardness result within a relatively low strain range of 0 – 1800. Generally, the increment of hardness as a function of strain can be divided into 3 stages. The hardness value increases with increasing strain quickly at the initial stage of deformation for lower strains (less than 400). Here the fast increase of hardness is due to the combination of contributions of grain refinement and formation of solid solutions. For the second stage when the strain increases from 400 to about 4000 (equivalent to the strain of position at radius of 3 mm deformed with 294 rotations), hardness is improved from 440 to 480 (roughly 9%). For the third stage, when the strain reaches about 4000, the dissolution of Cu into Cr becomes saturated which is consistent with the stabilization of hardness value. The hardness value is invariable within the range of 480 – 495 HV even the sample is deformed with extremely high strain to 16000.

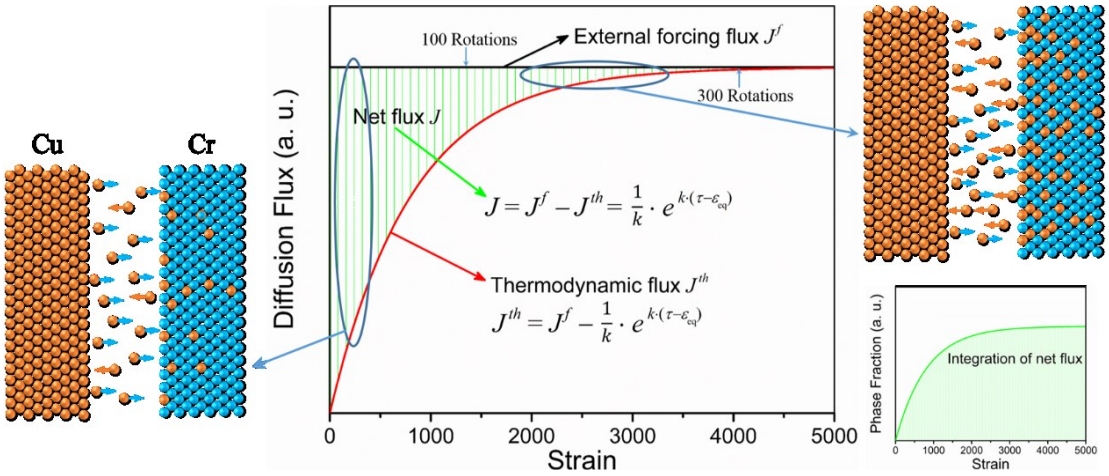

Fig. 10 Schematic diagram of forced mixing and thermodynamic decomposition between Cu and Cr grains under continuous deformation.

A phenomenological model is proposed to interpret the dissolution process based on experimental data. The idea of thermodynamics-related diffusion is employed to describe the inverse flow of dissolved solute atoms during deformation. Net dissolution flux J is a result of competition between external forced mixing and thermodynamic back diffusion, equaling to the difference value between external forced flux J^f and thermodynamic backflow flux J^{th}. Finally we show that J^{th} is a negative exponential function of applied strain $\varepsilon_{\mathrm{eq}}$ as shown in Eq. (7), so it will increase as the increasing strain, but with a finite limit value.

$$J^{th} = J^f - \frac{1}{k} e^{k(\tau-\varepsilon_{\mathrm{eq}})} \tag{7}$$

Fig. 10 shows the schematic diagram of forced mixing and thermodynamic decomposition between Cu and Cr grains. The external forced flux J^f (black line at the top) remains constant during deformation, while the thermodynamic decomposition flux J^{th} (red curve) shows a negative exponential increasing trend. As the leftmost diagram shows, at the initial stage of deformation, because of the small amount of accumulated net Cu solute atoms, the absolute back-diffusion flux is very small but with a high increasing speed. When the sample is deformed with high strains, the back-diffusion flux increases and approaches the level of forced flux due to the large amount of net Cu solute atoms, the dissolution of Cu atoms into Cr matrix saturates as shown in the top-right diagram. The difference value between forced flux and thermodynamic diffusion flux represents the net flux, and the integrated area (green shaded area) indicates the accumulated net Cu solute atoms.

2.1.2 Shear deformation induced grain refinement and intermixing

Dual-phase Cu-Cr composite with different initial phase hardness and ductility is deformed with controllable small strains by high pressure torsion. Shear deformation processes are observed at the atomic scale to get insights into the grain refinement and intermixing in ductile-brittle Cu-Cr system at the early stage of deformation.

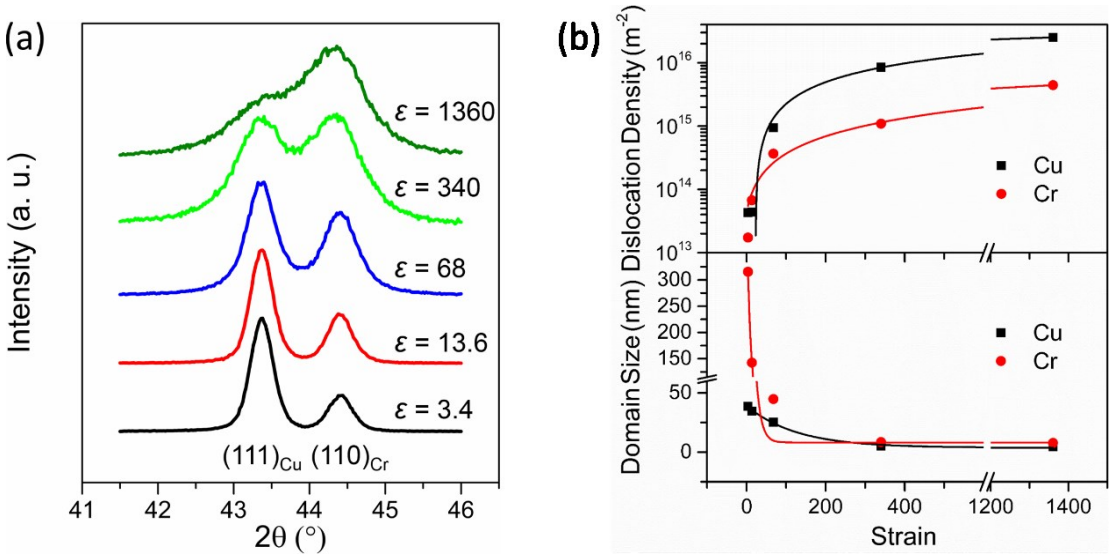

Fig. 11 XRD characterization of raw material and as-deformed composites. (a) XRD patterns focusing on $(111)_{Cu}$ and $(110)_{Cr}$ peaks. (b) Dislocation density and domain size calculated from XRD patterns as a function of applied strain (ε = 3.4, 13.6, 68, 340, 1360).

Fig. 11a shows XRD patterns centered on $(111)_{Cu}$ and $(110)_{Cr}$ peaks of raw material and as-deformed samples. The XRD patterns clearly indicate the relative intensity ratio change between *fcc* and *bcc* structures. Fig. 11b displays the dislocation densities and domain sizes calculated based on the full range XRD patterns according to Williamson-Hall plot. It can be seen that the dislocation densities increase monotonically, accompanied with a fast decrease of domain sizes (which denotes the spacing between incoherent structures) during the first 5 rotations (equivalent strain ε less than 68). Unlike the continuous increase of dislocation densities, domain sizes reach saturation at values of several nanometers after deformation of 25 rotations (ε = 340).

Figs. 12(a - d) show the corresponding bright-field (BF) and high angle annular dark field (HAADF) STEM images of Cu-rich and Cr-rich regions deformed with different numbers of rotations. A Cr-rich region is checked and corresponding BF and HAADF-STEM images are shown in Figs. 12(a, b). Large area EDXS measurement indicates that the whole tip is composed of about 90 at.% Cr and 10 at.% Cu. The Cr grains show lamellar structures aligned along the radial direction of HPT disk, with a thickness of about 30 – 100 nm. Furthermore, large numbers of dislocations are visible in the Cr lamellae. Unexpectedly, in HAADF-STEM images very thin layers with thickness of 1 – 2 nm and brighter contrast exist between two Cr lamellae, which are identified as the Cu phase. In contrast to the Cr-rich areas, the Cu-rich regions show much finer grains for both Cu and Cr phases with equiaxed structures as shown in Fig. 12c. Some scattered Cr grains are embedded in the Cu matrix, and the grain sizes of Cu and Cr are mainly in the range of about 20 – 40 nm and 40 – 60 nm respectively.

When the Cu-Cr composite is deformed with 25 rotations (ε = 340), the microstructures become equiaxed and more homogeneous for both Cu and Cr phases as shown in Fig. 12d. However, particularly interesting is the occurrence of less than 2 nm sized Cu clusters with

bright contrast inside the Cr grains. These embedded Cu nanoclusters could still retain a *bcc* structure because no any heterogeneous phase is observed in HRTEM images inside Cr grains.

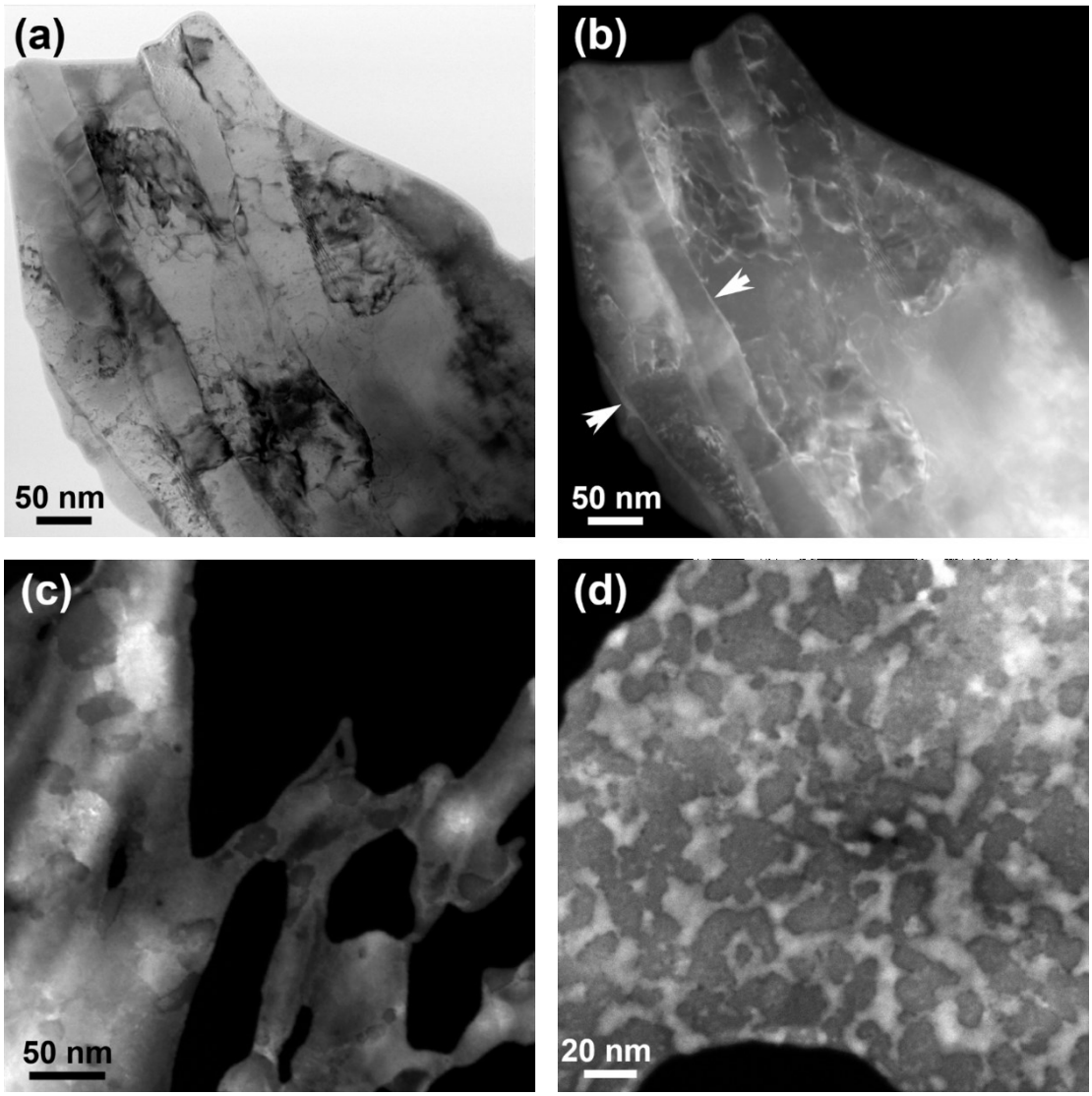

Fig. 12 (a, b) Corresponding BF-STEM and HAADF-STEM images of a Cr-rich region deformed with 5 rotations. (c) HAADF-STEM image of a Cu-rich region deformed with 5 rotations. (d) HAADF-STEM image of a Cr-rich region deformed with 25 rotations.

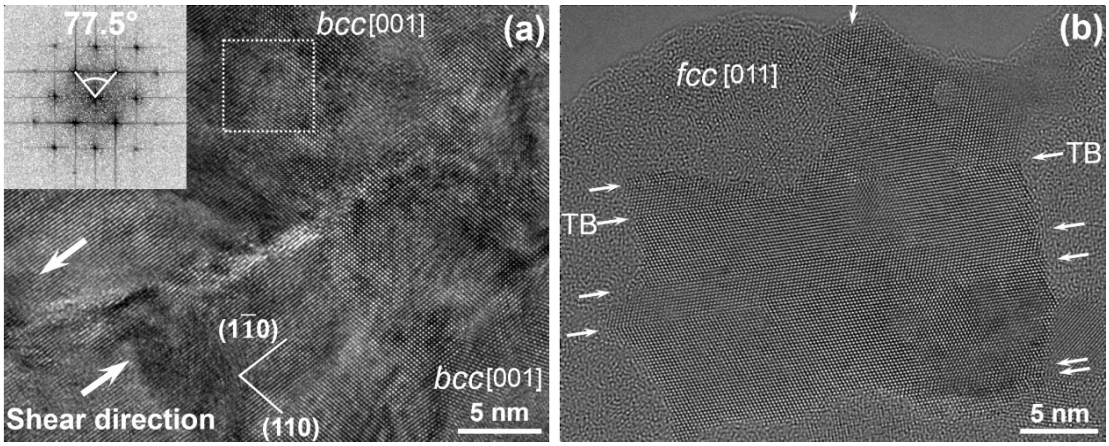

Fig. 13 Atomic structural characterizations of as-deformed sample with 25 rotations. (a) HRTEM image of two neighboring Cr grains. (b) HRTEM image displaying a Cu grain with many nanotwins, dislocations and stacking faults. Twin boundary is abbreviated as TB and indicated by white arrows.

The HRTEM image shown in Fig. 13a covers two neighboring Cr grains. The both two grains are on zone axes close to $[001]_{bcc}$. However, the lattices of these two grains are clearly subjected to a shear distortion along the interface. In addition, many dislocations can be found locating at the interface of two subgrains. Fig. 13b displays a clear HRTEM image focusing on one Cu grain with many defects, i.e., nanotwins, dislocations and stacking faults. It can be seen that there are many nanotwins present with thickness of only several atomic layers.

2.2 Cu-Fe system

One particular concern raised during the consolidation and straining processes is the unavoidable contamination from gaseous species, especially oxygen, which generates discrepant microstructures and properties [41]. We show that high pressure torsion can fragment the oxides formed during the mixing of powders precursors and eventually cause oxygen dissolution in matrix. Those dissolved oxygen atoms as interstitials in the matrix lead to lattice expansion and dramatic decrease of stacking fault energy locally. Such oxygen-mediated microstructure gives rise to enhanced strength at the expense of ductility, and superior structural stability. In addition, TEM is used to investigate the behavior of oxygen during *in-situ* heating of highly-strained Cu-Fe alloys at the atomic scale. Contrary to expectations, oxide formation occurs prior to the decomposition of the metastable Cu-Fe solid solution. This oxide formation commences at relatively low temperatures, forming nano-sized clusters of firstly CuO and later Fe_2O_3.

2.2.1 Oxygen-mediated deformation and grain refinement

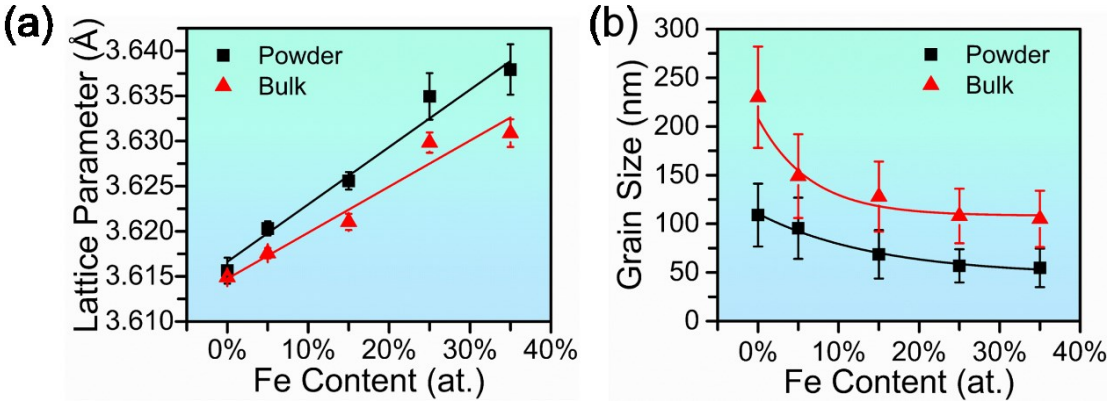

Fig. 14 Microstructural characterizations of as-deformed Cu-Fe alloys. (a) Lattice parameter and (b) grain size changes as a function of Fe content.

The lattice parameters calculated for both powder and bulk samples increase with increasing Fe content (see Fig. 14a), i.e., Fe dissolution facilitates the expansion of the *fcc* matrix. Simultaneously, oxygen impurities also play a big role on the lattice parameter of the as-deformed alloys. Powder samples which have higher oxygen concentrations possess larger lattice parameters compared to bulk samples with the same compositions. The obtained average grain sizes based on large population statistics are shown in Fig. 14b for all compositions. It is quite evident that Fe solutes can significantly refine the grains, that is, higher Fe concentration results in finer grains. Especially, for samples with Fe additions of less than 15 at.%, the refinement effect is extremely pronounced. In addition, powder sample has an obviously smaller grain size as compared to the same composition sample deformed from arc-melted bulk material.

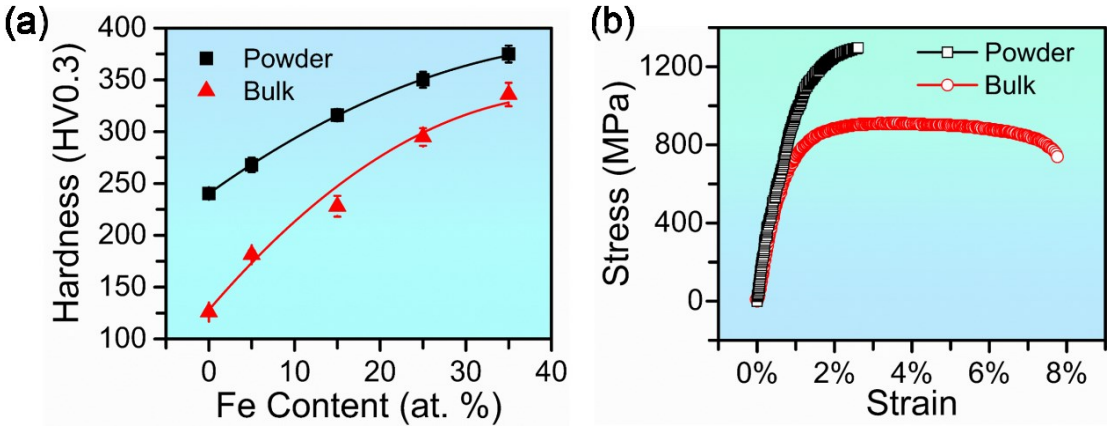

Fig. 15 Mechanical properties of as-deformed Cu-Fe alloys. (a) Hardness change as a function of Fe content. (b) Tensile experiment results of 75Cu-25Fe powder and bulk samples.

The hardness values of all Cu-Fe alloys deformed from powders and arc-melted bulk with various Fe contents are shown in Fig. 15a. The hardness improvement with increasing Fe content is found for both powder and bulk samples. The bulk sample shows a significantly

lower hardness compared to the powder sample with the same Fe content. The stress-strain curves shown in Fig. 15b provide the maximum stress and strain to fracture of 75Cu-25Fe powder and bulk samples. The powder sample has an ultimate tensile strength of about 1300 MPa and a failure strain of 2.6%, while for the bulk sample the ultimate strength and failure strain are 910 MPa and 7.8%. Hence, the pronounced influence of oxygen on the tensile properties contributes to a 43% higher ultimate tensile strength while it deteriorates the ductility by about 67%.

Fig. 16 displays the overview image and O distribution of a 75Cu-25Fe powder sample obtained by atom probe tomography (APT). The overview image shows a mixture of Fe and O clusters embedded in the Cu matrix due to thermal decomposition. It can be seen from the bottom APT image that in addition to a rather homogeneous oxygen distribution some clusters with sizes of 3 – 8 nm exist at the grain boundaries. APT shows a strong evidence that oxygen atoms can be dissolved by SPD into the matrix. Quantification of the oxygen content provides a value of 0.310 at.% O for the powder sample while 0.047 at.% O are contained in the bulk sample. The residual proportion of oxygen enriched at grain boundaries is mainly responsible for the grain refinement by lowering grain boundary energy. Grain refinement is mainly responsible for increasing hardness and strength while deteriorating the ductility.

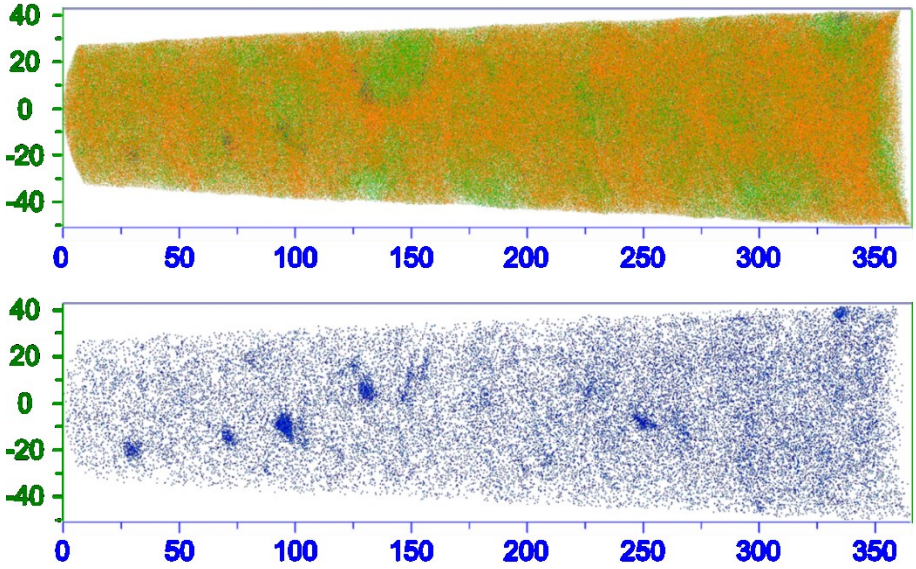

Sample	Powder	Bulk
O Content (at.%)	0.310	0.047

Fig. 16 APT results of annealed 75Cu-25Fe powder sample. Upper image is an overview image containing Fe and O clusters, and the bottom image shows the O-rich distribution. The O contents in powder and bulk samples are listed in the table.

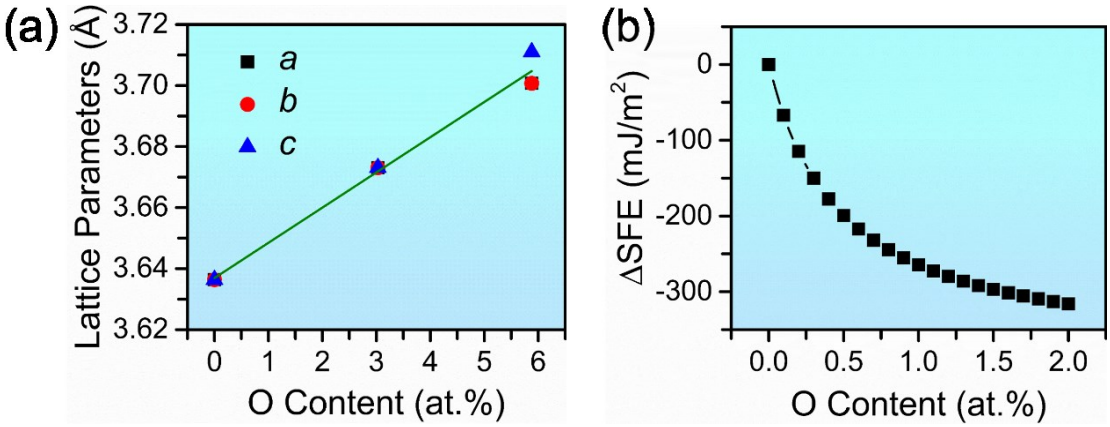

Fig. 17 DFT calculations of the (a) lattice parameter and (b) SFE changes as a function of O content, respectively.

In order to confirm the oxygen effect on the lattice expansion shown in Fig. 14a, density functional theory (DFT) calculations are carried out to obtain the relationship between lattice parameters and different contents of interstitial oxygen in the *fcc* matrix. Here to simplify the explanation, a pure Cu unit cell containing 32 atoms is employed as a reference, followed by introducing 1 (3.03 at.%) and 2 (5.88 at.%) interstitial oxygen atoms, respectively. The calculated results of lattice parameter as a function of oxygen concentration are displayed in Fig. 17a. Generally, it can be seen that the lattice parameters increase linearly as the increment of oxygen concentration, while the lattice distortion appears with *c* axis elongating faster than *a* and *b* axes at the oxygen concentration of 5.88 at.%. To investigate the oxygen's influence on the SFE, we conduct DFT calculation of the SFE change as a function of oxygen concentration as shown in Fig. 17b. It can be clearly seen that the intrinsic SFE decreases greatly as the oxygen content increases. This calculation gives evidence of that the dissolved oxygen can drastically decrease the SFE of Cu-based nanocrystalline alloys.

2.2.2 Atomic-scale observation of oxygen's behavior

In-situ heating experiments are conducted in the TEM to characterize in detail the microstructural and compositional stabilities of the HPT deformed 75Cu-25Fe powder alloy.

The integrated profiles of diffraction patterns recorded on the same area, obtained using PASAD [42] are shown in Fig. 18. All peaks in the profiles are indexed to planes of *fcc* matrix, Fe precipitates or oxides based on the interplanar spacing. It is worth noting that at the left-hand side of $(111)_{fcc}$ peak, i.e., the larger interplanar spacing values than that of $(111)_{fcc}$, some weak peaks corresponding to oxides (marked as $(101)_{CuO}$, $(112)_{Fe2O3}$ and $(110)_{CuO}$) appear when the temperature reaches 260 °C. At an even higher temperature of 340 °C additional $(200)_{Fe}$ and $(211)_{Fe}$ peaks from Fe can also be clearly observed.

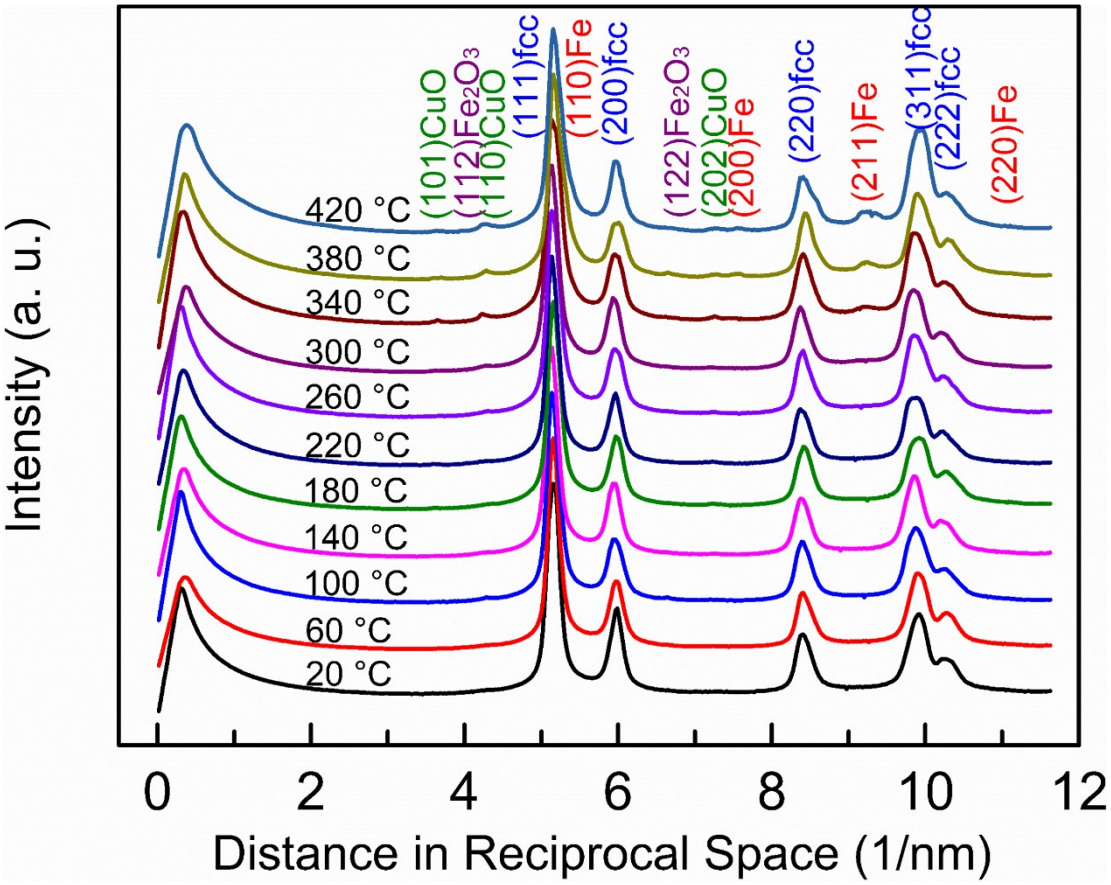

Fig. 18 Integrated profiles of diffraction patterns recorded on the same area.

Electron energy loss spectroscopy (EELS) mapping is implemented to detect the elemental distributions of *ex-situ* sample annealed at 420 °C as shown in Fig. 19. From the Fe L mapping in Fig. 19d, it can be seen that Fe grains that have grown due to the decomposition usually have rounded corner shapes, with grain size of about 20 – 50 nm. By comparing the Fe_L mapping, we can see that the dark areas are corresponding to the Fe grains in Fig. 19a, where some small Fe grains are marked with white circles. Fig. 19b shows the O_K mapping, oxides form during annealing have dimensions from several nanometers to tens of nanometers. Except some oxides precipitates are present at the grain boundaries, many small oxide clusters form inside the grains. The Fe concentration histogram shown in Fig. 19e is extracted along a red arrow in Fig. 19d from a pure Fe grain to the Cu matrix. It can be seen that after *ex-situ* annealing at 420 °C, the residual Fe in Cu matrix is about 18 – 20 at.%.

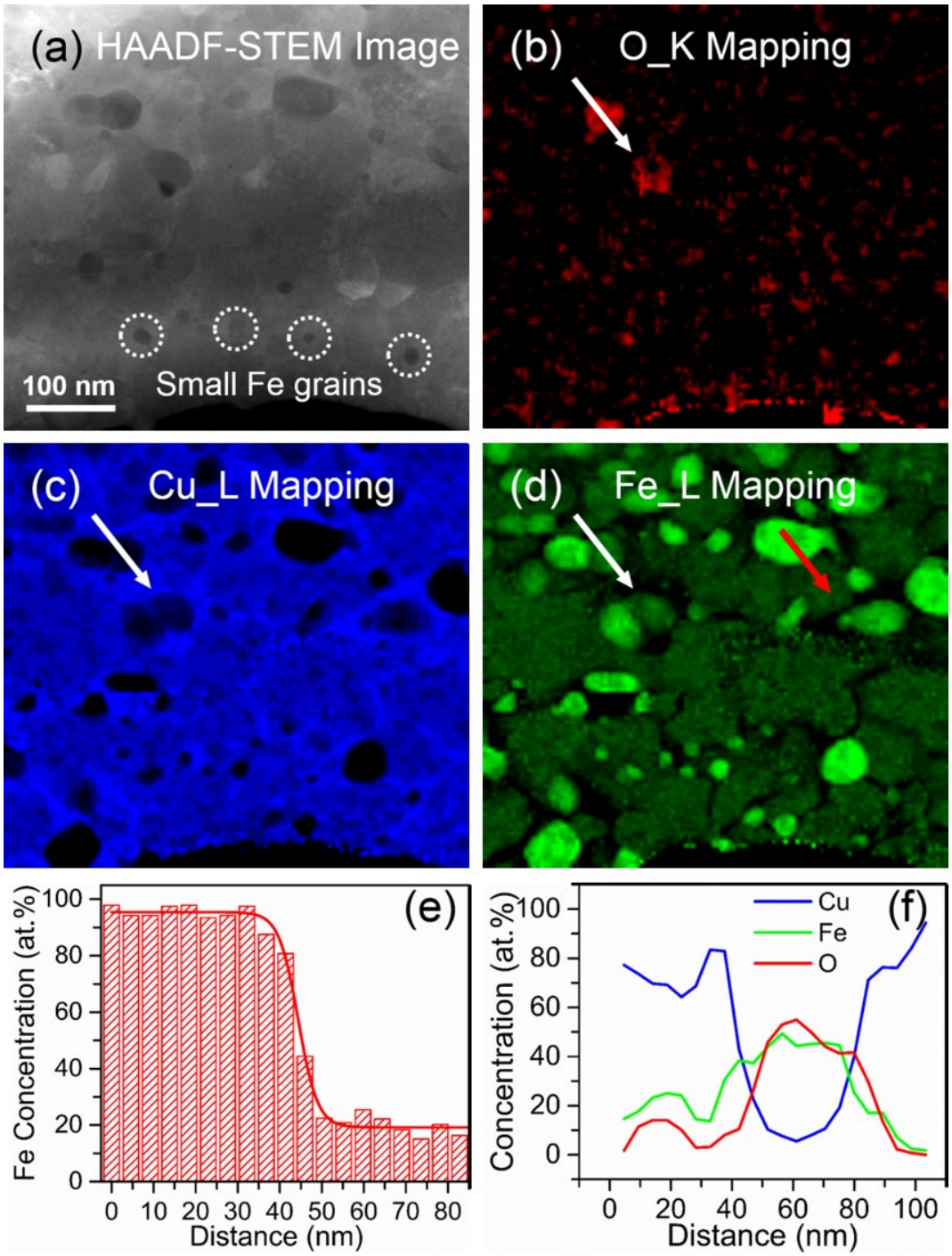

Fig. 19 Electron energy loss spectroscopy (EELS) elemental mapping of *ex-situ* annealed sample at 420 °C. (a) HAADF-STEM image. (b) O_K mapping. (c) Cu_L mapping. (d) Fe_L mapping. (e) Fe concentration histogram obtained from line scan along red arrow displayed in (d). (f) Cu, Fe and O composition profiles extracted from line scan of the same position indicated by the white arrows in (b-d).

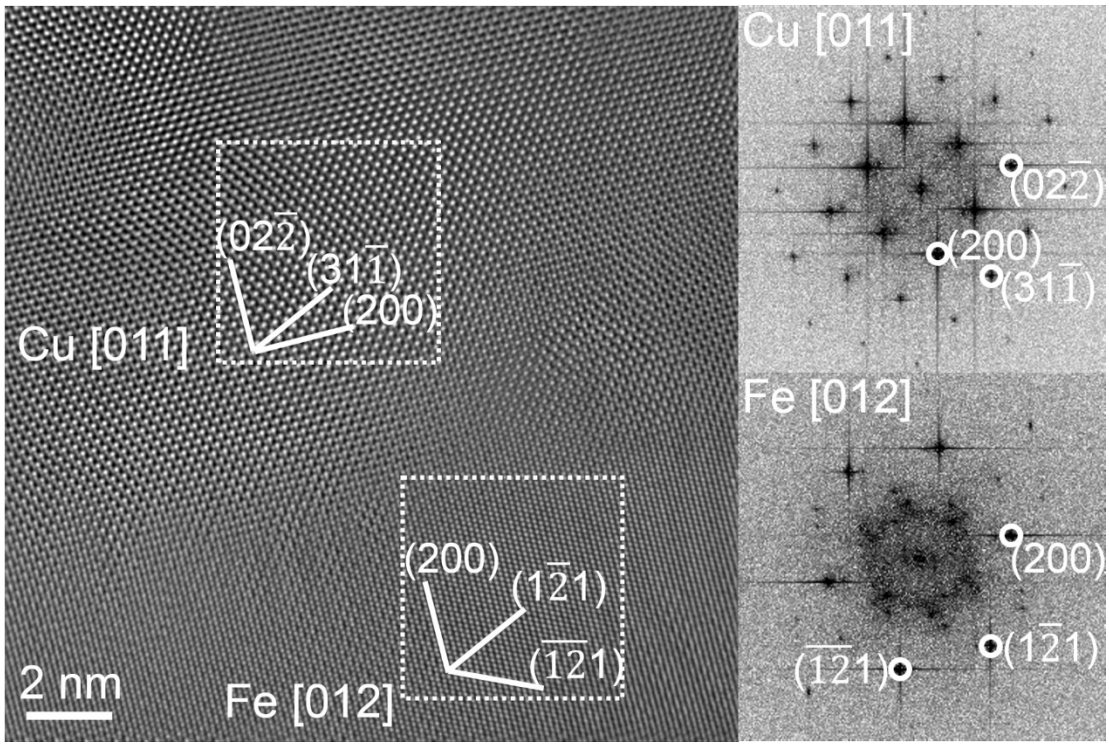

Fig. 20 HRTEM image of the sample *ex-situ* annealed at 420 °C showing the neighboring Cu and Fe grains on zone axes of $[011]_{Cu}$ and $[012]_{Fe}$ respectively. The two FFT images are calculated based on the Cu and Fe areas marked with white frames.

Fe grain nucleation and growth occur due to thermal decomposition in the 75Cu-25Fe alloy. Fig. 20 displays a HRTEM image of the sample *ex-situ* annealed at 420 °C showing neighboring Cu and Fe grains along $[011]_{Cu}$ and $[012]_{Fe}$ zone axes, respectively. Evidently, the neighboring Cu and Fe grains have an orientation relationship of $(02\bar{2})_{Cu}$ // $(200)_{Fe}$, which is different from the typical K-S relationship commonly observed for the interface between *fcc* and *bcc* structures, i.e., $(111)_{fcc}$ // $(110)_{bcc}$ [43].

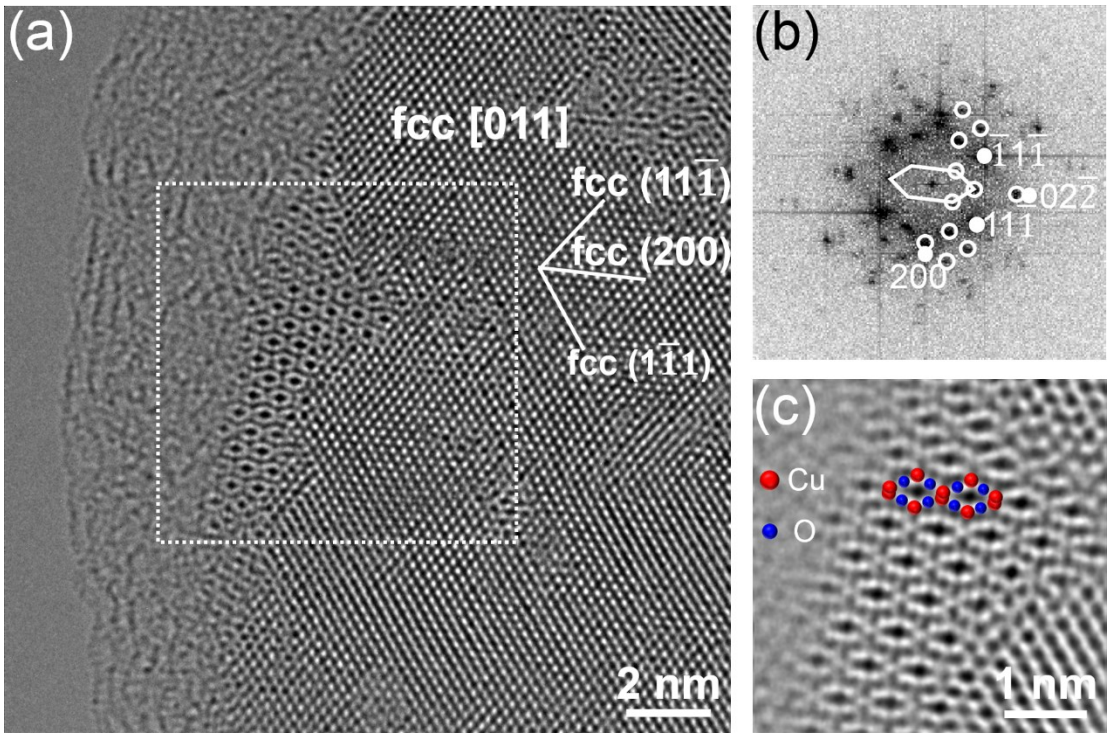

Fig. 21 Lattice matching relationship between CuO and *fcc* matrix. (a) HRTEM image of CuO developed from *fcc* matrix on $[011]_{fcc}$ zone axis. (b) FFT image calculated from the white frame area in (a). (c) Enlarged filtered CuO HRTEM image.

Fig. 21 shows a HRTEM image of CuO developing within the *fcc* matrix after annealing at 420 °C. The *fcc* matrix shows a lattice structure on a $[011]_{fcc}$ zone axis, while CuO is exactly on the $[001]_{CuO}$ zone axis. The FFT calculated from the area within the white frame in Fig. 21a and an enlarged filtered CuO HRTEM image are displayed in Fig. 21b and Fig. 21c respectively. In the FFT image, it can be clearly seen that the matching relationship between CuO and the *fcc* matrix is $(\bar{4}00)_{CuO}$ // $(200)_{fcc}$ and $(020)_{CuO}$ // $(02\bar{2})_{fcc}$, with a corresponding lattice mismatch of 6.2% and 10.4% in each direction.

Fig. 22 shows a schematic diagram of oxidation process at the atomic scale. After severe deformation of the 75Cu-25Fe alloy, the oxygen atoms are randomly distributed at the centers of octahedra as interstitials in the *fcc* lattice as shown in Fig. 22a [44–47]. The oxygen atoms are activated by heating and diffuse in the *fcc* lattice. The schematic diagram of the activation process of O atoms is shown in Fig. 22b, where the configurations of the initial state, transition state and final state are displayed respectively. The activated oxygen atoms then diffuse through the *fcc* lattice, forming O-rich nanoclusters [46,47] as shown in Fig. 22c. Because of the existence of ample point defects, such as vacancies, solute atoms and O interstitials in severely deformed alloys, the formation energy of O-rich nanoclusters is greatly decreased due to the bound state of high-stability O-Vacancy pairs [46]. The binding energy of O with one nearest-neighbor Fe vacancy is about -1.45 eV [46,47]. At the next stage, oxides nucleate when the external heating energy is imposed on the O-rich area. According to the experimental results, the nucleation of oxides starts at 60 °C when the sample is heated for 10 min. Our theoretical calculation shows that the formation enthalpies of CuO and Fe_2O_3 are lower than

those of their counterparts, Cu_2O and FeO, respectively. Thus, from the viewpoint of the formation enthalpy, it may explain the formation of CuO and Fe_2O_3 rather than other oxides with different valences. The reason why CuO is observed prior to Fe_2O_3 is most likely ascribed to the large volume of Cu in the alloy. The finally formed CuO lattice along $[001]_{CuO}$ zone axis embedded in the *fcc* matrix on zone axis of $[011]_{fcc}$ is illustrated in the schematic diagram of Fig. 22d.

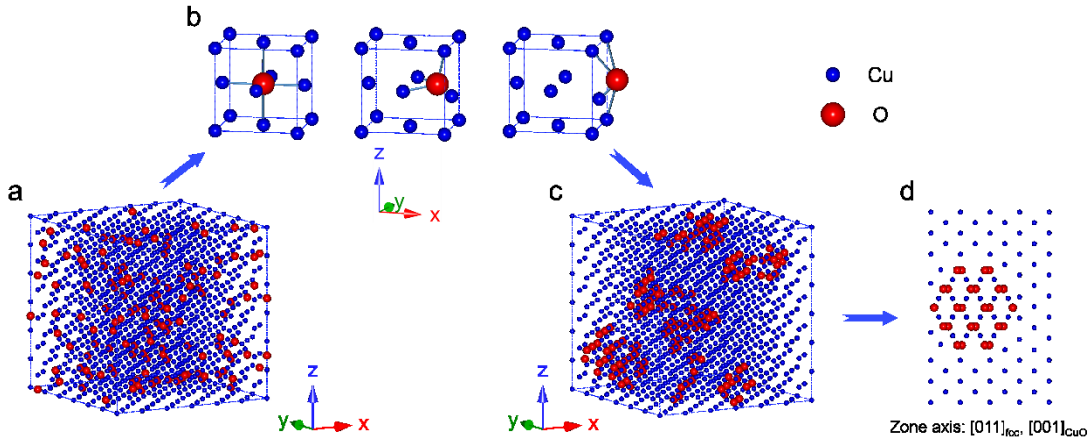

Fig. 22 Schematic diagram of the oxidation process. (a) As-deformed state with oxygen randomly distributed in *fcc* matrix. (b) Oxygen movement from one octahedral center to another. (c) O-rich nanoclusters formation inside the *fcc* matrix. (d) Formed CuO on zone axis of $[001]_{CuO}$ embedded inside *fcc* matrix on zone axis of $[011]_{fcc}$.

3

Conclusions

57 wt.%Cu - 43 wt.%Cr is HPT deformed with controllable strains, including deformation to extremely high strains. A nanocrystalline alloy is formed with average grain size less than 20 nm and a good homogeneity. The main conclusions can be summarized as follows:

1. The dissolution-induced phase change is driven by continuous deformation. The phase fraction change of as-deformed Cu-Cr alloys shows an obvious negative exponential trend. In the saturated state, about 32 wt.% (27.8 at.%) of Cu can be fully dissolved into Cr matrix forming a *bcc* structure. Only about 3 wt.% (3.6 at.%) Cr can be dissolved into Cu phase even the sample is deformed with 100 rotations (strain of 1360).
2. The grain refinement of 57 wt.%Cu - 43 wt.%Cr sample is accomplished during the initial stage of deformation. When the sample is deformed with 25 rotations (strain of 340), the average grain size decreases dramatically from micron-scale to less than 20 nm. Only a slight further refinement to average size of 13.7 nm occurs even the sample is deformed to 100 rotations.
3. A hardness value of 480 – 495 is obtained when the deformation reaches 100 rotations or even higher. At the initial stage, the fast increase of hardness mainly comes from the grain refinement. For later stage, the slight increment is mainly due to increased amount of dissolved Cu into Cr matrix.
4. A kinetic dissolution model is proposed based on the idea of that final solubility is determined by the competition of external forced mixing and thermodynamic decomposition.

Furthermore, the low-strain deformed ductile-brittle Cu-Cr alloy is also systematically investigated. Our observations offer the direct evidence seemingly supporting the dislocation-shuffling mechanism in forced chemical intermixing of non-equilibrium system under severe plastic deformation. Some key points are summarized:

5. The solubility of both elements is strongly dependent on the Cu- or Cr-rich regions.

6. Cu clusters of dimensions of less than 2 nm are found inside the Cr grains, and retain a *bcc* lattice structure.
7. The atomic-scale distortion of Cr lattice induced by shear deformation has been detected directly, giving rise to formation of small angle grain boundary due to dislocation accumulation at the interface.

In the Cu-Fe system, the oxygen effects on nanocrystalline alloys have been systematically investigated. Cu-Fe nanostructured alloys with different compositions are prepared by HPT from blended powders (high oxygen content) and arc-melted bulk (low oxygen content). The following conclusions can be drawn:

8. It is found that oxygen introduced during the powder pre-mixing can be partially dissolved into the matrix via extreme deformation.
9. The residual proportion of oxygen enriched at grain boundaries can effectively facilitate the grain refinement predominantly by lowering grain boundary energy.
10. Grain boundary migration is the dominant mechanism in current alloys, assisted by the effects of lowering SFE, solid solution hardening and "interstitial oxygen hardening".
11. Grain refinement is mainly responsible for increasing hardness and strength while deteriorating the ductility.
12. The dissolved interstitial oxygen atoms can effectively lower SFE of nanocrystalline alloy locally.

In addition, aberration-corrected HRTEM and associated techniques are employed to investigate the behavior of oxygen during *in-situ* heating of highly-strained Cu-Fe alloys. The main conclusions are:

13. Oxide formation occurs prior to the decomposition of the metastable Cu-Fe solid solution. This oxide formation commences at relatively low temperatures, forming nano-sized clusters of firstly CuO and later Fe_2O_3.
14. The orientation relationship between these clusters and the matrix differs from that observed in conventional steels.
15. The matching relationship between CuO and the *fcc* matrix is $(\bar{4}00)_{CuO}$ // $(200)_{fcc}$ and $(020)_{CuO}$ // $(02\bar{2})_{fcc}$.

References

[1] R.Z. Valiev, T.G. Langdon, Principles of equal-channel angular pressing as a processing tool for grain refinement, Prog. Mater. Sci. 51 (2006) 881–981.

[2] A.P. Zhilyaev, T.G. Langdon, Using high-pressure torsion for metal processing: Fundamentals and applications, Prog. Mater. Sci. 53 (2008) 893–979.

[3] T.G. Langdon, The processing of ultrafine-grained materials through the application of severe plastic deformation, J. Mater. Sci. 42 (2007) 3388–3397.

[4] R.Z. Valiev, The new trends in fabrication of bulk nanostructured materials by SPD processing, J. Mater. Sci. 42 (2007) 1483–1490.

[5] Y. Estrin, A. Vinogradov, Extreme grain refinement by severe plastic deformation: A wealth of challenging science, Acta Mater. 61 (2013) 782–817.

[6] Y. Saito, H. Utsunomiya, N. Tsuji, T. Sakai, Novel ultra-high straining process for bulk materials – development of the accumulative roll-bonding (ARB) process, Acta Mater. 47 (1999) 579–583.

[7] T.G. Langdon, Twenty-five years of ultrafine-grained materials: Achieving exceptional properties through grain refinement, Acta Mater. 61 (2013) 7035–7059.

[8] P.W. Bridgman, On torsion combined with compression, J. Appl. Phys. 14 (1943) 273–283.

[9] M. Kawasaki, R.B. Figueiredo, T.G. Langdon, An investigation of hardness homogeneity throughout disks processed by high-pressure torsion, Acta Mater. 59 (2011) 308–316.

[10] E.O. Hall, The deformation and ageing of mild steel: discussion of results, Proc. Phys. Soc. B 64 (1951) 747–753.

[11] S. Yip, The strongest size, Nature 391 (1998) 532–533.

[12] F.A. Mohamed, S.S. Dheda, On the minimum grain size obtainable by high-pressure torsion, Mater. Sci. Eng. A 558 (2012) 59–63.

[13] Y.H. Zhao, X.Z. Liao, Y.T. Zhu, Z. Horita, T.G. Langdon, Influence of stacking fault energy on nanostructure formation under high pressure torsion, Mater. Sci. Eng. A 410–411 (2005) 188–193.

[14] L. Balogh et al., Influence of stacking-fault energy on microstructural characteristics of ultrafine-grain copper and copper-zinc alloys, Acta Mater. 56 (2008) 809–820.

[15] C.X. Huang et al., The effect of stacking fault energy on equilibrium grain size and tensile properties of nanostructured copper and copper-aluminum alloys processed by equal channel angular pressing, Mater. Sci. Eng. A 556 (2012) 638–647.

[16] K. Edalati, Z. Horita, High-pressure torsion of pure metals: Influence of atomic bond parameters and stacking fault energy on grain size and correlation with hardness, Acta Mater. 59 (2011) 6831–6836.

[17] R. Pippan et al., Saturation of fragmentation during severe plastic deformation, Annu. Rev. Mater. Res. 40 (2010) 319–343

[18] E. Bruder et al., Influence of solute effects on the saturation grain size and rate

sensitivity in Cu-X alloys, Scr. Mater. 144 (2018) 5–8.

[19] K. Edalati et al., Influence of dislocation-solute atom interactions and stacking fault energy on grain size of single-phase alloys after severe plastic deformation using high-pressure torsion, Acta Mater. 69 (2014) 68–77.

[20] R. Labusch, Statistical theories of solid solution hardening. Acta Metall. 20 (1972) 917–927.

[21] F. Tang, D.S. Gianola, M.P. Moody, K.J. Hemker, J.M. Cairney, Observations of grain boundary impurities in nanocrystalline Al and their influence on microstructural stability and mechanical behaviour, Acta Mater. 60 (2012) 1038–1047.

[22] J. W. Gibbs, The collected works of J.W. Gibbs. Longmans, Green and Co. (1928).

[23] P.C. Millett, R.P. Selvam, A. Saxena, Stabilizing nanocrystalline materials with dopants, Acta Mater. 55 (2007) 2329–2336.

[24] J. Eckert, J.C. Holzer, C.E. Krill III, W.L. Johnson, N. Fe, Reversible grain size changes in ball-milled nanocrystalline Fe-Cu alloys, J. Mater. Res. 7 (1992) 1980–1983.

[25] J. Eckert, J.C. Holzer, C.E. Krill III, W.L. Johnson, Mechanically driven alloying and grain size changes in nanocrystalline Fe-Cu powders, J. Appl. Phys. 73 (1993) 2794–2802.

[26] E. Ma, H.W. Sheng, J.H. He, P.J. Schilling, Solid-state alloying in nanostructured binary systems with positive heat of mixing, Mater. Sci. Eng. A 286 (2000) 48–57.

[27] D. Raabe, S. Ohsaki, K. Hono, Mechanical alloying and amorphization in Cu-Nb-Ag in situ composite wires studied by transmission electron microscopy and atom probe tomography, Acta Mater. 57 (2009) 5254–5263.

[28] D. Raabe et al., Metallic composites processed via extreme deformation: Toward the limits of strength in bulk materials, MRS Bull. 35 (2010) 982–991.

[29] P. Bellon, R.S. Averback, Nonequilibrium roughening of interfaces in crystals under shear: Application to ball milling, Phys. Rev. Lett. 74 (1995) 1819–1822.

[30] P. Bellon et al., Crossover from superdiffusive to diffusive mixing in plastically deformed solids, Phys. Rev. Lett. 99 (2007) 110602.

[31] Y. Ashkenazy, N.Q. Vo, D. Schwen, R.S. Averback, P. Bellon, Shear induced chemical mixing in heterogeneous systems, Acta Mater. 60 (2012) 984–993.

[32] S.N. Arshad et al., Dependence of shear-induced mixing on length scale, Scr. Mater. 68 (2013) 215–218.

[33] H. Rose, Outline of a spherically corrected semiaplanatic medium-voltage transmission electron-microscope, Optik 85 (1990) 19–24.

[34] M. Haider et al., Electron microscopy image enhanced, Nature 392 (1998) 768–769.

[35] M. Lentzen et al., High-resolution imaging with an aberration-corrected transmission electron microscope, Ultramicroscopy 92 (2002) 233–242.

[36] J.H. Chen, H.W. Zandbergen, D. Van Dyck, Atomic imaging in aberration-corrected high-resolution transmission electron microscopy, Ultramicroscopy 98 (2004) 81–97.

[37] C.L. Jia, L. Houben, A. Thust, J. Barthel, On the benefit of the negative-spherical-

aberration imaging technique for quantitative HRTEM, Ultramicroscopy 110 (2010) 500–505.

[38] C.L. Jia, M. Lentzen, K. Urban, Atomic-resolution imaging of oxygen in perovskite ceramics, Science 299 (2016) 870–873.

[39] A.K. De et al., Quantitative measurement of deformation-induced martensite in 304 stainless steel by X-ray diffraction, Scr. Mater. 50 (2004) 1445–1449.

[40] Y. Xu, S.H. Zhang, M. Cheng, H.W. Song, In situ X-ray diffraction study of martensitic transformation in austenitic stainless steel during cyclic tensile loading and unloading, Scr. Mater. 67 (2012) 771–774.

[41] E. Ma, Alloys created between immiscible elements, Prog. Mater. Sci. 50 (2005) 413–509.

[42] C. Gammer, C. Mangler, C. Rentenberger, H.P. Karnthaler, Quantitative local profile analysis of nanomaterials by electron diffraction, Scr. Mater. 63 (2010) 312–315.

[43] D. Tian, F. Jona, P.M. Marcus, Structure of ultrathin films of Fe on Cu {111} and Cu {110}, Phys. Rev. B 45 (1992) 11216–11221.

[44] D.E. Jiang, E.A. Carter, Carbon dissolution and diffusion in ferrite and austenite from first principles, Phys. Rev. B 67 (2003) 214103.

[45] C. Barouh, T. Schuler, C.C. Fu, M. Nastar, Interaction between vacancies and interstitial solutes (C, N, and O) in α-Fe: From electronic structure to thermodynamics, Phys. Rev. B 90 (2014) 054112.

[46] C.L. Fu, M. Krčmar, G.S. Painter, X.Q. Chen, Vacancy mechanism of high oxygen solubility and nucleation of stable oxygen-enriched clusters in Fe, Phys. Rev. Lett. 99 (2007) 225502.

[47] T. Schuler, C. Barouh, M. Nastar, C.C. Fu, Equilibrium vacancy concentration driven by undetectable impurities, Phys. Rev. Lett. 115 (2015) 015501.

4

List of Appended Papers

Paper I

J. Guo, J. Rosalie, R. Pippan, Z. Zhang

On the phase evolution and dissolution process in Cu-Cr alloys deformed by high pressure torsion

Scripta Materialia 133 (2017) 41–44.

Paper II

J. Guo, J. Rosalie, R. Pippan, Z. Zhang

Revealing the microstructural evolution in Cu-Cr nanocrystalline alloys during high pressure torsion

Materials Science and Engineering A 695 (2017) 350–359.

Paper III

J. Guo, R. Pippan, Z. Zhang

Insights into shear deformation induced grain refinement and intermixing in ductile-brittle Cu-Cr composite via high pressure torsion

Will be submitted to ***Scripta Materialia***.

Paper IV

J. Guo, G. Haberfehlner, J. Rosalie, L. Li, M.J. Duarte, G. Dehm, G. Kothleitner, Y. He, R. Pippan, Z. Zhang

In-situ atomic-scale observation of oxidation and decomposition processes in nanocrystalline alloys

Nature Communications, accepted, in press.

Paper V

J. Guo, M.J. Duarte, Y. Zhang, G. Dehm, R. Pippan, Z. Zhang

Oxygen-mediated deformation and grain refinement in nanocrystalline alloys

Will be submitted to ***Nature Communications***.

Remarks

In the appended papers, myself, Jinming Guo, performed all experiments, the data analyses and the composition of the publications with the following exceptions:

- In **paper I**

  Dr. Julian Rosalie helped taking SEM images.

- In **paper II**

  Dr. Julian Rosalie helped taking SEM images.

- In **paper III**

  Prof. Reinhard Pippan participated with helpful discussions.

- In **paper IV**

  Dr. Georg Haberfehlner and Prof. Gerald Kothleitner conducted STEM EELS mapping experiments. Dr. María Jazmin Duarte and Prof. Gerhard Dehm carried out the APT characterization. Mr. Lei Li and Prof. Yunbin He performed XPS measurements.

- In **paper V**

  Dr. María Jazmin Duarte and Prof. Gerhard Dehm carried out the APT characterization. Mr. Yong Zhang performed theoretical calculations. Dr. Andrea Bachmaier conducted tensile experiments, and Dr. Christoph Gammer recorded diffraction contrast images.

- My supervisor, Dr. Zaoli Zhang participated in all the papers by giving the basic ideas for the publications and with helpful discussions during their preparation.

5

Collection of Publications

I

On the phase evolution and dissolution process in Cu-Cr alloys deformed by high pressure torsion

Jinming Guo, Julian Rosalie, Reinhard Pippan, Zaoli Zhang

Erich Schmid Institute of Materials Science, Austrian Academy of Sciences, 8700 Leoben, Austria

Abstract

Normally immiscible 57 wt.%Cu - 43 wt.%Cr compounds were mechanically alloyed by means of high pressure torsion with large and controllable strains. A strain-saturated state in 57 wt.%Cu - 43 wt.%Cr bulk was achieved after 100 rotations deformation (effective strain 1360), with a stable grain size of 13.7 nm and largest solubility of 32 wt.% Cu in Cr matrix. The phase fraction change between face-centered cubic and body-centered cubic due to Cu dissolution during continuous deformation was captured and accurately calculated, indicating a negative exponential phase change mode. A phenomenological dissolution mechanism based on the kinetic competition between mixing under sustained external forcing and thermal diffusion induced decomposition was proposed, which was well compliant with the phase evolution observed from experimental results.

Keywords

Severe plastic deformation, high pressure torsion, Cu-Cr nanocrystalline, dissolution process

Severe plastic deformation (SPD) has drawn intensive attention for the last two decades due to its superior advantages in developing novel ultra-fine nanocrystalline materials even out of "immiscible" composites [1]. Of the various SPD methods [1], high pressure torsion (HPT) is one of the most efficient mechanical alloying techniques where a disk is subjected to a high applied pressure and concurrent torsional straining [2–5]. For alloys, Cu-Cr was thought one of the promising compounds among non-equilibrium systems in potential applications requiring high strength, good electrical and thermal conductivity, and excellent oxidation and corrosion resistance [6]. The reported results have shown that supersaturated solid solutions of up to 15 at.% (17.7 wt.%) Cu in the body-centered cubic (bcc) Cr phase with grain size of 10 – 20 nm were formed after 25 revolutions of deformation [7,8]. To date mechanical alloying of Cu-Cr system by either HPT process or ball milling, has found a solubility limit of Cu atoms into Cr of 15 at.%. Such relatively low solubility may limit the further improvement of strength or other properties for bulk materials [7,9].

As already known, alloys generated in so-called "immiscible" systems at room temperature are non-equilibrium, unstable phases. Even for those systems with liquid miscibility, the thermodynamic driving force for diffusion is dominated by the positive heat of mixing, so that the diffusing atomic fluxes will generally proceed in the direction which causes chemical segregation and phase decomposition. Kinetic models have been proposed to describe the alloying process as a competition between sustained external forcing during plastic deformation and decomposition due to thermal diffusion [10,11]. But up to now, for severely deformed alloys, experiments on the quantitative investigation of phase evolution during deformation have not been attempted, and further detailed understanding of the relationship between the extent of dissolution and applied strain is still lacking.

In this work, micrometer-sized staring bulk of nominal 57 wt.% - 43 wt.%Cr (57Cu-43Cr) was deformed with different high-strained revolutions, from 25 rotations to even 1000 rotations in accordance with strain of 340 to 13600. Simultaneously, phase fractions at different deformation conditions were well calculated and a possible model was proposed based on above-mentioned kinetic model from the phenomenological point of view to describe the dissolution process in details.

The initial bulk material with nominal composition of 57 wt.%Cu - 43 wt.%Cr (volume and atom fraction of about 50%.) was produced by PLANSEE (Reutte, Austria). Disks with a diameter of 8 mm and an initial thickness of about 1.0 mm were HPT-deformed with different numbers of rotations N (N = 25, 50, 100, 300, 420, 1000) under a constant pressure of 7.3 GPa and a rotation speed of 0.4 rotation/min. X-ray diffraction (XRD) was conducted on all samples using Smartlab X-Ray Diffractor (Rigaku, Japan) with Cu $K_{\alpha 1}$ radiation (λ = 1.540593 Å). Here it should be emphasized that the X-ray beam width for all the measurements in this work was limited to 2 mm using an incident slit, covering a large area of HPT deformed disks from a radius of 2 mm to 4 mm. Transmission electron microscopy (TEM) and scanning transmission electron microscopy (STEM) characterizations were carried out using a field emission gun transmission electron microscope (JEOL JEM-2100F, Japan) equipped with an imaging spherical aberration corrector and an Oxford INCA Energy TEM 200 energy-dispersive X-ray spectroscopy (EDXS) system. All microstructural investigations were undertaken at radius of 3.0 mm from the torsional axis of the HPT deformed disks.

Fig. 1a shows the fine scanning XRD patterns of 57 wt.%Cu - 43 wt.%Cr raw material and deformed samples with different numbers of rotations, and the peaks for $(111)_{fcc}$ and $(110)_{bcc}$ are separated from the measured curves (black) by accurate fitting with residual value less than 2%. The final overall fitted curve (red) is nearly the same as measured curve. Fig. 1b shows

the relative intensity ratio of $(111)_{fcc}$ and $(110)_{bcc}$ calculated based on integrated area of each corresponding peak after subtracting the background [12]. The relative intensity ratio of $(111)_{fcc}$ clearly decreased from 0.71 for raw bulk material to 0.38 for the sample deformed with 300 rotations. It then remained constant even when the sample was deformed further to 1000 rotations. From the relationship between relative intensity ratio and corresponding strain, the relative intensity ratio of $(110)_{bcc}$ increased quickly when the sample was deformed in the first 100 rotations, and then this value tended to stabilize at the level around 0.62. Based on the principle that the integrated intensity of diffraction peak for each phase in a mixture is proportional to the volume fraction of that phase [13,14], dissolved Cu content at each strain condition can be obtained by comparing the calculated relative intensity ratio with the values of standard blended Cu-Cr powders of different compositions, which is shown in Fig. 1c. The curve shows an obvious negative exponential change mode, with an approaching value of 32 wt.%, indicating the solubility limit of Cu in Cr by HPT is 32 wt.%.

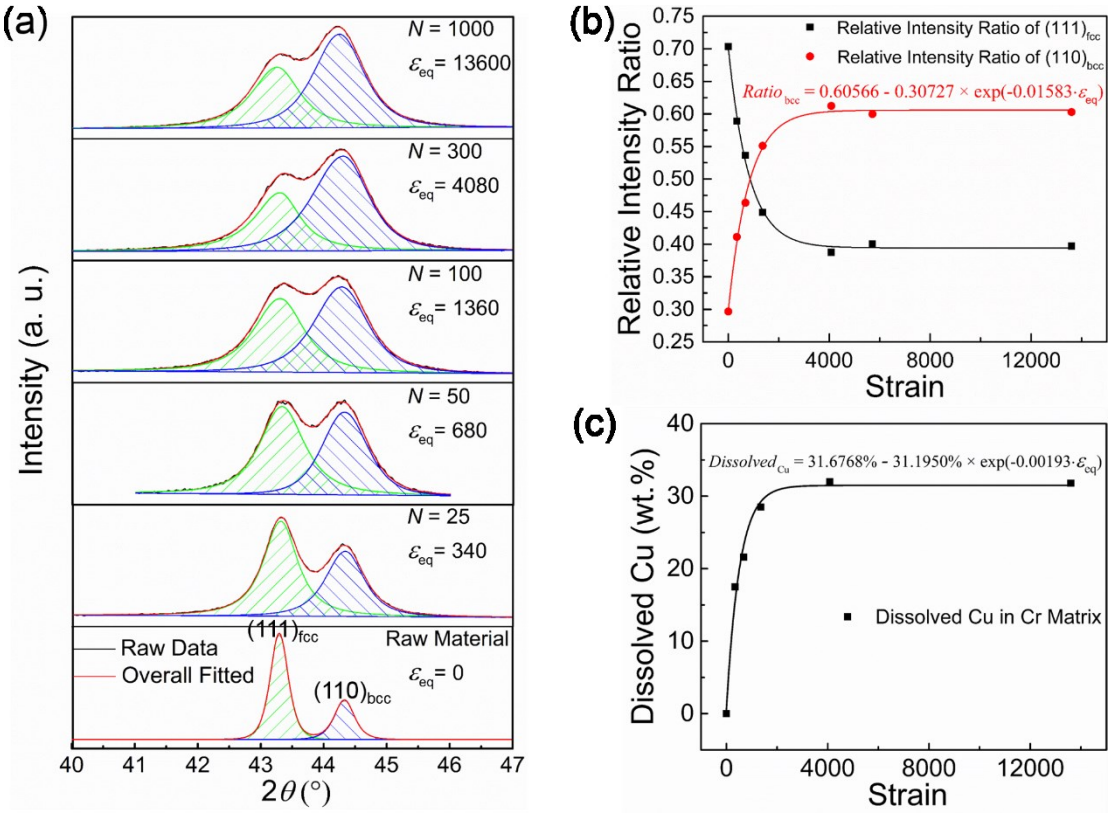

Fig. 1. Phase evolution of HPT deformed samples. (a) XRD patterns of 57 wt.%Cu - 43 wt.%Cr raw material and as-deformed samples with different numbers of rotations in the range of 40˚ – 47˚. (b) Relative intensity ratio changes of $(111)_{fcc}$ and $(110)_{bcc}$ peaks with different numbers of rotations. (c) Dissolved Cu content change as a function of applied strains.

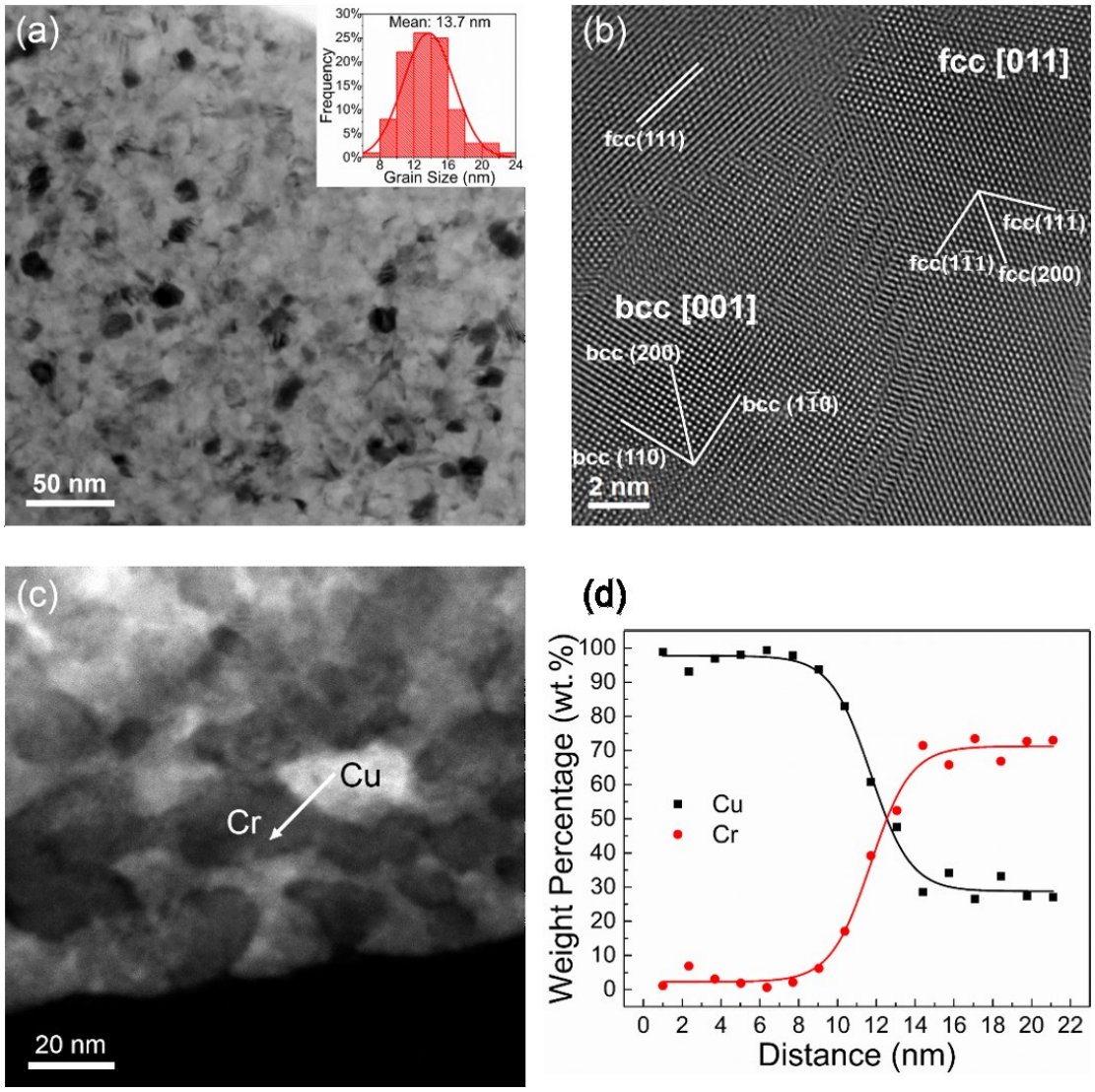

Fig. 2. Microstructures characterization of HPT deformed sample with 100 rotations. (a) TEM bright field image. (b) HRTEM image displaying three adjacent grains of Cu and Cr with different zone axis. (c) High angle annular dark field STEM image. (d) Weight percentage concentration profile measured across Cu and Cr grains along the white arrowline shown in STEM image (c).

Figs. 2a-d show the microstructure characterization of 57Cu-43Cr deformed with 100 rotations. Fig. 2a is a TEM bright field image where grains are equiaxed and randomly distributed, with almost spherical shape. This also facilitates statistic measurement of grain size regarding the grain as a sphere and the diameter of the sphere is the calculated grain size [15]. The inset in top-right corner is histogram showing the grain size with narrow distribution indicating the average grain size is about 13.7 nm, which is based on a statistical measurement of more than 100 grains. Fig. 2b shows HRTEM image of three adjacent grains of Cu and Cr with different zone axes. The grain in right side is Cu with fcc structure and on zone axis of [011] which is parallel to the incident electron beam while the bottom-left grain is chromium

with bcc structure and on zone axis of [001]. In this image, $(1\bar{1}0)_{Cr}$ plane of Cr grain is strictly parallel to $(1\bar{1}1)_{Cu}$ plane of Cu grain, which is the typical matching relationship of bcc and fcc structure with $\{110\}_{bcc}//\{111\}_{fcc}$ [16–18]. In the top-left corner, the grain is not well on zone axis, but $\{111\}_{Cu}$ planes can still be distinguished from the results of spacing measurement. Fig. 2c shows the high angle annular dark field STEM image, displaying dark areas as Cr grains and bright areas as Cu grains. Fig. 2d shows the weight percentage concentration profile measured across Cu and Cr grains along the white arrowline shown in STEM image Fig. 2c. The spacing between two measurement ponits for EDXS line-scan is 1.4 nm with a electron probe size of 0.5 nm. EDXS measurement shown here was obtained at the extremely thin area of edge part to insure no overlapping of grains (beam broadening effect is negligible). The concentration profile in Fig. 2d shows that about 30.5 wt.% (26.4 at.%) of Cu has been dissolved into Cr grains, simultaneously Cu grains contain about 3.9 wt.% (4.7 at.%) of dissolved Cr.

For the observed negative exponential Cu dissolution in Fig. 1c, here a phenomenological model was proposed to interpret dissolution process based on our experimental data. The idea of thermodynamics-related diffusion was employed to describe the inverse flow of dissolved solute atoms during deformation. Net dissolution flux J is a result of competition between external forcing mixing and thermodynamic back diffusion, equaling to the difference value between external forcing flux J^f and thermodynamic backflow flux J^{th} as shown in equation (1):

$$J = J^f - J^{th} \tag{1}$$

In the whole deformation process, the forcing flux J^f is a constant, and the thermodynamic self-diffusion is positively related to the concentration of solute atoms which equals to accumulation of net flux J. Based on this assumption, equation (2) can be drawn as follows:

$$dJ^{th} = \kappa(J^f - J^{th})d\varepsilon_{\mathrm{eq}} \tag{2}$$

where dJ^{th} means the change of thermodynamic diffusion in a strain interval of $d\varepsilon_{\mathrm{eq}}$ due to the accumulation of solute atoms, and κ is a coefficient. After integration of each side as shown in following part, we can obtain the equation (3) of J^{th}, which shows the change of thermodynamic diffusion as a function of strain $\varepsilon_{\mathrm{eq}}$, where τ is a strain constant:

$$J^{th} = J^f - \frac{1}{k}e^{k(\tau-\varepsilon_{\mathrm{eq}})} \tag{3}$$

Eq. (3) shows that J^{th} is a negative exponential function of applied strain $\varepsilon_{\mathrm{eq}}$, so it will increase with increasing strain, but with an approaching value. Fig. 3 shows the schematic diagram of forced mixing and thermodynamic decomposition between Cu and Cr grains. The external forcing flux J^f (black line in the top) remains constant during deformation, while the thermodynamic decomposition flux J^{th} (red curve) shows a negative exponential increasing trend. As the leftmost diagram shows, in the beginning stage of deformation, because of the little amount of accumulated net Cu solute atoms, the absolute back-diffusion flux is very small but with a high increasing speed. When the sample is deformed with high strains, the back-diffusion flux approaches the level of forcing flux due to the large amount of net Cu solute atoms, so the dissolution of Cu atoms into Cr matrix gets saturated as shown in the top-right diagram. The difference between forcing flux and thermodynamic diffusion flux represents net flux, and the integrated area (green shaded area) indicates the accumulated net Cu solute atoms. Mathematically, a negative exponential formula can be obtained from the integration of another

negative exponent. So the final dissolved Cu content involving the integration of net flux J should also show a negative exponential increasing, as shown in the bottom-right inset in Fig. 3, which fits well with the experimental data in Fig. 1c.

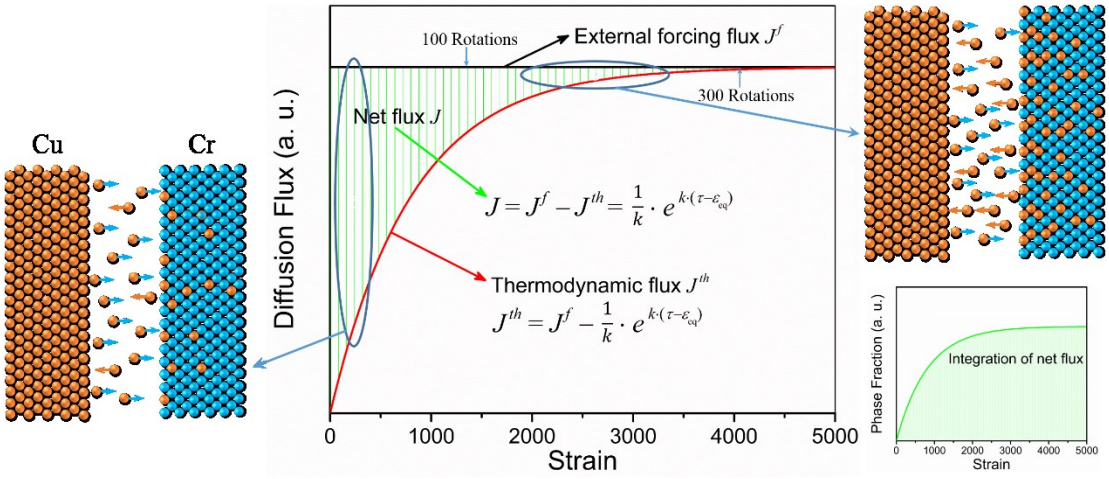

Fig. 3. Schematic diagram of forced mixing and thermodynamic decomposition between Cu and Cr grains under continuous deformation.

In summary, 57 wt.%Cu - 43 wt.%Cr nanocrystalline alloy was formed with average grain size less than 20 nm and good homogeneity by HPT deformation with extremely high strains. This work showed that about 32 wt.% (27.8 at.%) of Cu can be fully dissolved into Cr matrix to form bcc structure using HPT method. The phase fraction change of deformed Cu-Cr alloy showed an obvious negative exponential trend. A kinetic dissolution model was proposed in this work based on the idea of that final solubility was determined by the competition of external forcing mixing and thermodynamic decomposition. The obtained negative exponential formula fits well with experimental result. This model facilitates the understanding of dissolution process.

Acknowledgements

We gratefully acknowledge the financial support by the Austrian Science Fund (FWF): No. P27034 - N20. Peter Kutleša, Gabriele Moser, Herwig Felber and Silke Modritsch at Erich Schmid Institute of Materials Sciences, Austrian Academy of Sciences, are gratefully acknowledged for their help with the HPT, TEM and metallographical samples preparation.

References

[1] R.Z. Valiev, R.K. Islamgaliev, I.V. Alexandrov, Prog. Mater. Sci. 45 (2000) 103–189.

[2] A.P. Zhilyaev, T.G. Langdon, Prog. Mater. Sci. 53 (2008) 893–979.

[3] A.P. Zhilyaev, G.V. Nurislamova, B.K. Kim, M.D. Baró, J.A. Szpunar, T.G. Langdon, Acta Mater. 51 (2003) 753–765.

[4] A. Vorhauer, R. Pippan, Scr. Mater. 51 (2004) 921–925.

[5] M. Kawasaki, R.B. Figueiredo, T.G. Langdon, Acta Mater. 59 (2011) 308–316.

[6] R.K. Islamgaliev, K.M. Nesterov, J. Bourgon, Y. Champion, R.Z. Valiev, J. Appl. Phys. 115 (2014) 1–5.

[7] X. Sauvage, P. Jessner, F. Vurpillot, R. Pippan, Scr. Mater. 58 (2008) 1125–1128.

[8] A. Bachmaier, G.B. Rathmayr, M. Bartosik, D. Apel, Z. Zhang, R. Pippan, Acta Mater. 69 (2014) 301–313.

[9] C. Aguilar, V.deP. Martinez, J.M. Palacios, S. Ordoñez, O. Pavez, Scr. Mater. 57 (2007) 213–216.

[10] P. Bellon, R.S. Averback, Phys. Rev. Lett. 74 (1995) 1819–1822.

[11] C. Gente, M. Oehring, R. Bormann, Phys. Rev. B. 48 (1993) 13244–13252.

[12] L.M. Wang, Z.B. Wang, K. Lu, Acta Mater. 59 (2011) 3710–3719.

[13] A.K. De, D.C. Murdock, M.C. Mataya, J.G. Speer, D.K. Matlock, Scr. Mater. 50 (2004) 1445–1449.

[14] Y. Xu, S.H. Zhang, M. Cheng, H.W. Song, Scr. Mater. 67 (2012) 771–774.

[15] D.G. Morris, M.A. Muñoz-Morris, Acta Mater. 50 (2002) 4047–4060.

[16] M. Liang, Y. Lu, Z. Chen, C. Li, G. Yan, C. Li, P. Zhang, IEEE Trans. Appl. Supercond. 20 (2010) 1619–1621.

[17] N.A. Mara, D. Bhattacharyya, R.G. Hoagland, A. Misra, Scr. Mater. 58 (2008) 874–877.

[18] D. Tian, F. Jona, P.M. Marcus, Phys. Rev. B 45 (1992) 11216–11221.

II

Revealing the microstructural evolution in Cu-Cr alloys during high pressure torsion

Jinming Guo, Julian Rosalie, Reinhard Pippan, Zaoli Zhang

Erich Schmid Institute of Materials Science, Austrian Academy of Sciences, 8700 Leoben, Austria

Abstract

Usually immiscible Cu-Cr compounds in equilibrium condition were mechanically processed via high pressure torsion with large and controlled strains. A systematical investigation on 57 wt.%Cu - 43 wt.%Cr was carried out to get insights into the microstructural evolution of Cu-Cr nanocomposites and their dissolution process, as well as to determine the solid solubility limit of Cu and Cr elements under severe deformation. Microstructural evolution was captured with grain refinement from micron-size down to less than 20 nm as the increase of strains. A strain-saturated state in 57 wt.%Cu - 43 wt.%Cr bulk was achieved after 100 rotations deformation (effective strain 1360), with a stable grain size of 13.7 nm and invariable hardness of 480 – 495 HV. Fine scanning of X-ray diffraction and sub-nanometer scale measurements of energy-dispersive X-ray spectroscopy showed that 32 wt.% Cu could be fully dissolved into Cr matrix , and conversely solubility of Cr in Cu was determined to be about 3 wt.% after an enough amount of deformation. The phase fraction change associated with Cu dissolution into Cr matrix during continuous deformation was captured and accurately calculated, indicating a negative exponential phase change mode. A phenomenological intermixing mechanism based on the kinetic competition between external forcing mixing and thermal-diffusion induced decomposition was proposed, which was well accordant with the phase evolution observed from experimental results.

Keywords

High pressure torsion, Cu-Cr nanocrystalline alloy, dissolution process, X-ray diffraction, transmission electron microscopy

1. Introduction

Severe plastic deformation (SPD) has been quite arrestive for the last two decades due to its superior advantages in fabrication of novel nanocrystalline bulk materials even out of "immiscible" composites [1], such as Cu-based binary systems [2,3] including Cu-Fe [4–8], Cu-Cr [9–12], Cu-Nb [13–15], Cu-Ta [16] and Al-based systems including Al-Mg [17–21], Al-Zn [18,19], which possess a lot of excellent mechanical, thermal or electrical properties. Of the various SPD methods [1], for instance, equal-channel angular pressing [17,20,22], accumulative roll-bonding [23,24], high energy ball milling [25,26], bundling and drawing [13,14] and so on, high pressure torsion (HPT) is one of the most efficient mechanical alloying techniques where a disk is subjected to a high applied pressure and concurrent torsional straining [27–30]. In practice, this metal forming process provides an opportunity for achieving exceptional grain refinement in applicable bulk materials, often to the nanometer level. Due to the large grain refinement and chemical intermixing that occurs during processing, this technique poses another route to produce binary or even polynary alloys with very high mechanical strength.

Among non-equilibrium systems, Cu-Cr was widely investigated and thought of as a promising alloys in potential applications. Sauvage *et al.* processed a Cu-Cr composite containing 43 wt.% Cr by high pressure torsion and found that the grain size of the unprocessed composite was reduced from 40 – 60 μm to 10 – 20 nm after 25 revolutions of deformation under a pressure of 6 GPa [9]. It was found that super saturated solid solutions (SSSSs) of up to 15 at.% (17.7 wt.%) Cu in the body-centered cubic (bcc) Cr phase were formed but no formation of SSSSs of Cr in the face-centered cubic (fcc) Cu phase was observed. Bachmaier *et al.* obtained similar results for grain refinement, hardness increase and the formation of Cu SSSSs in Cr matrix [10]. To date mechanical alloying of Cu-Cr system by either HPT process or ball milling, has given a solubility limit of Cu atoms into Cr of 15 at.%, which may limit the further improvement of comprehensive properties for bulk materials [9,26]. A detailed understanding of the relationship between the dissolution volume and applied strain is still lacking.

As already known, alloys fabricated from such "immiscible" systems at room temperature are non-equilibrium with metastable phases. Because the thermodynamic driving force for diffusion is dominated by the positive heat of mixing even for those systems with liquid miscibility, so that the thermo-diffusing atomic fluxes will generally proceed in the direction which causes chemical segregation and phase decomposition. For solid-state alloying, nanostructuring to alter the energetics of systems and external driving force are two key strategies to form a stable alloys from "immiscible" systems [4,31]. Kinetic models have been proposed to describe the alloying process as a competition between external forcing mixing during plastic deformation and decomposition due to thermal diffusion [32,33].

Motivated by the promising properties of high content of Cu dissolved Cu-Cr bulk nanocrystalline materials, a series of investigations were conducted on micrometer-sized staring bulk of nominal 57 wt.% - 43 wt.%Cr with different high-strained revolutions, from 25 rotations to even 1000 rotations in accordance with strain of 340 to 13600. Simultaneously, the concurrent phase fraction change accompanied with microstructure evolution during deformation was well calculated and it showed a negative exponential transition mode. Here a possible intermixing model was proposed based on above-mentioned kinetic model from the phenomenological point of view to describe the dissolution process in detail, and it fitted well with experimental results.

2. Experimental

A commercial coarse-grained Cu-Cr bulk material was HPT deformed at room temperature with air cooling. The initial bulk material with nominal composition of 57 wt.%Cu - 43 wt.%Cr (volume and atom fraction of about 50%.) was produced by PLANSEE (Reutte, Austria). Left image in Figure 1 shows a backscattered electron image of the raw material with Cu (bright) and Cr (dark) particles having an average size of about 50 µm distributed homogeneously. Disks with a diameter of 8 mm and an initial thickness of about 1.0 mm were HPT-deformed with different numbers of rotations N (N = 25, 50, 100, 300, 420, 1000) under a constant pressure of 7.3 GPa and a rotation speed of 0.4 rotation/min. The schematic diagram of HPT is shown in the middle image of Fig. 1 All data shown in this paper is either presented as a function of strain ε_{eq} or given for a certain ε_{eq} (radius r = 3.0 mm from the disk center), respectively. ε_{eq} is calculated by equation (1) [10,27]

$$\varepsilon_{eq} = \frac{2\pi r \cdot N}{t \cdot \sqrt{3}} \quad (1)$$

where r is the radial distance from center of the disk. t is the thickness of deformed sample. The thickness value t was taken as 0.8 mm for all samples.

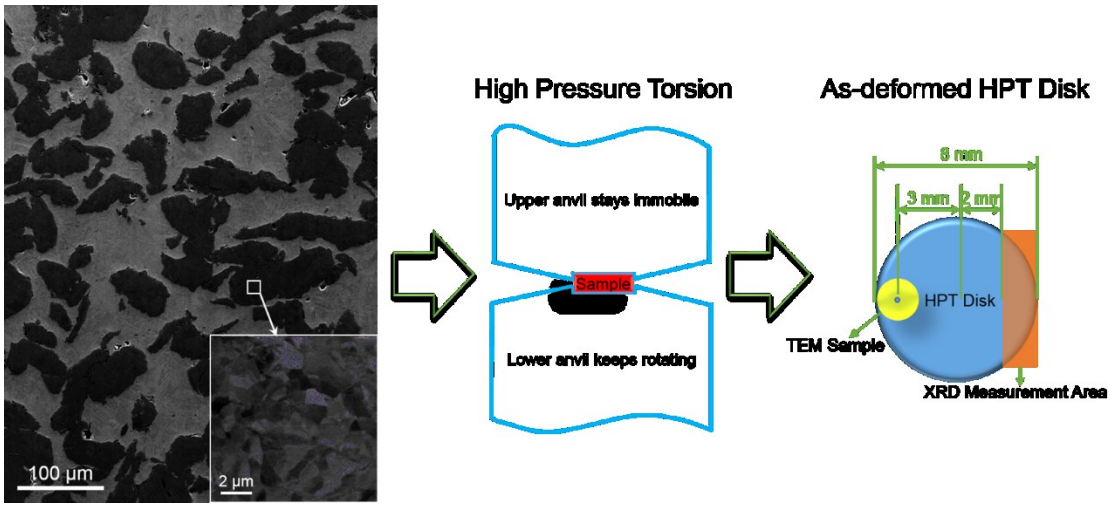

Fig. 1. Schematic diagram of HPT deformation. The left part shows the backscattered electron image of raw bulk material of 57 wt.%Cu - 43 wt.% Cr.

X-ray diffraction (XRD) was conducted on all samples using a Smartlab X-Ray Diffractometer (Rigaku, Japan) with Cu $K_{\alpha 1}$ radiation (λ = 1.540593 Å). A series of Cu-Cr powder compacts were produced for use as external standards in XRD experiments. Commercially-available powders from Alfa Aesar (Karlsruhe, Germany) of Cu (Purity 99.9%) and Cr (Purity 99.9%) were mixed and then compacted with a pressure of 7.3 GPa for 10 seconds. One such powder compact (with a composition of 30 wt.%Cu - 70 wt.%Cr) was also subjected to HPT using a two-stage method. The detailed information for this two stages method can be found in Ref. [5].

Here we emphasize that the X-ray beam width for all the measurements in this work was limited to 2 mm using an incident slit, covering a large area of HPT deformed disk from radius of 2 mm to 4 mm as shown in right schematic diagram of Fig. 1. The beam height was set to 1 mm, which indicates the beam will be elongated in the X-ray reflection direction to 1.41 mm – 3.24 mm for scanning range of 40˚ – 100˚ and to 2.77 mm – 3.24 mm for 40˚ – 47˚ measurement. Therefore, the X-ray actually covered a large area of disk from radius of 2 mm to 4 mm, and its results can represent the average effect of HPT disk in macro-scale, rather than localized measurement. The X-ray scanning speed is 0.4 ˚/min with step of 0.02˚.

Transmission electron microscope (TEM) and scanning transmission electron microscope (STEM) were used to characterize in detail the microstructure of the deformed material. All microstructural investigations were undertaken at radius of 3.0 mm from the torsional axis of the HPT deformed disks (as shown in right schematic diagram of Fig. 1). The (S)TEM samples were cut from the HPT disks, and then mechanically thinned and polished to a thickness of about 50 μm, followed by mechanical dimpling. Subsequently the samples were ion-milled using a Gatan Precision Ion Polishing System until perforation with voltage of 4 kV and angle of 4˚ – 6˚. (S)TEM studies were carried out using a field emission gun transmission electron microscope (JEOL JEM-2100F, Japan) equipped with an imaging spherical aberration corrector and an Oxford INCA Energy TEM 200 energy-dispersive X-ray spectroscopy (EDXS) system. In STEM mode, high angle annular dark field (HAADF) detector with a spot size of 0.7 nm was used to record HAADF-STEM images. EDXS for nanoscale compositional analysis was also carried out in STEM mode. The chemical compositions obtained from EDXS were analyzed using commercial INCA system or DigitalMicrograph software. The electron beam was perpendicular to the shear plane of the disks for all microstructural investigations shown in this work. Vickers microhardness measurements were conducted on a Buehler Mircomet 5100 using a load of 500 g (HV0.5). Indents were made across the radii of the disks with a spacing of 300 μm between the indents, and average values of six individual measurements with the same strain on deformed disks for each deformation condition are reported in this work.

3. Results

3.1 Phase evolution

Fig. 2a shows the X-ray diffraction (XRD) patterns of 57 wt.%Cu - 43 wt.%Cr raw material and deformed samples with different numbers of rotations. All the curves are normalized by the intensity of the highest peak, either $(111)_{Cu}$ or $(110)_{Cr}$. For all HPT-deformed samples, the structure is a two-phase mixture of face-centered cubic (fcc) and body-centered cubic (bcc) structures. The relative intensity ratio between $(111)_{Cu}$ and $(110)_{Cr}$ obviously changed with increasing number of rotations. The relative peak intensities for each phase matched well with standard polycrystalline diffraction peaks generated by the PowderCell programme. This means that grains of the HPT-deformed Cu-Cr alloys are randomly oriented and the influence of the texture on the X-ray can be neglected. If the grains of each phase are randomly oriented, quantitative estimation of phase fractions by XRD is feasible, based on the principle that the integrated intensity of diffraction peak for each phase in a mixture is proportional to the volume fraction of that phase [34,35]. In order to accurately calculate the integrated area of relevant peaks for each sample, the peaks of $(111)_{Cu}$ and $(110)_{Cr}$ are separated from the measured curves by accurate fitting with residual value less than 2%. The relative intensity ratio of $(111)_{Cu}$ and $(110)_{Cr}$ is then calculated according to following equation (2):

$$R_{Cu} = \frac{I_{Cu}}{I_{Cu}+I_{Cr}} \quad (2)$$

where R_{Cu} represents the relative intensity ratio of Cu peak, and I_{Cu} as well as I_{Cr} means the integrated area of each corresponding peak after subtracting the background [36].

The results calculated for the relative intensity ratio of $(111)_{Cu}$ and $(110)_{Cr}$ are plotted in Fig. 2b. The relative intensity ratio of $(111)_{Cu}$ decreased obviously from 0.71 for raw bulk material to 0.38 for the sample deformed with 300 rotations. It then remained constant even the sample was deformed further to up to 1000 rotations. From the relationship between relative intensity ratio and number of rotations (and corresponding strain), the relative intensity ratio of $(110)_{Cr}$ increases quickly when the sample was deformed in the first 100 rotations, and then this value tended to stabilize with the level around 0.62. Fig. 2c shows the lattice parameters calculated from the fine scanning of $(111)_{Cu}$ and $(110)_{Cr}$ peaks, using the relationship of that lattice constant equals to $\sqrt{2}$ times of the spacing of (110) plane and $\sqrt{3}$ times of the spacing of (111) regarding the structure as cubic phase. Generally, both of the lattice parameters of Cu phase and Cr phase are increased as the increasing of numbers of rotations. The dissolution of Cu and Cr atoms into each counterparts causes the expansion of each cubic lattice, which is in agreement with the lattice change reported for Cu-Cr alloys in the literatures [2,3].

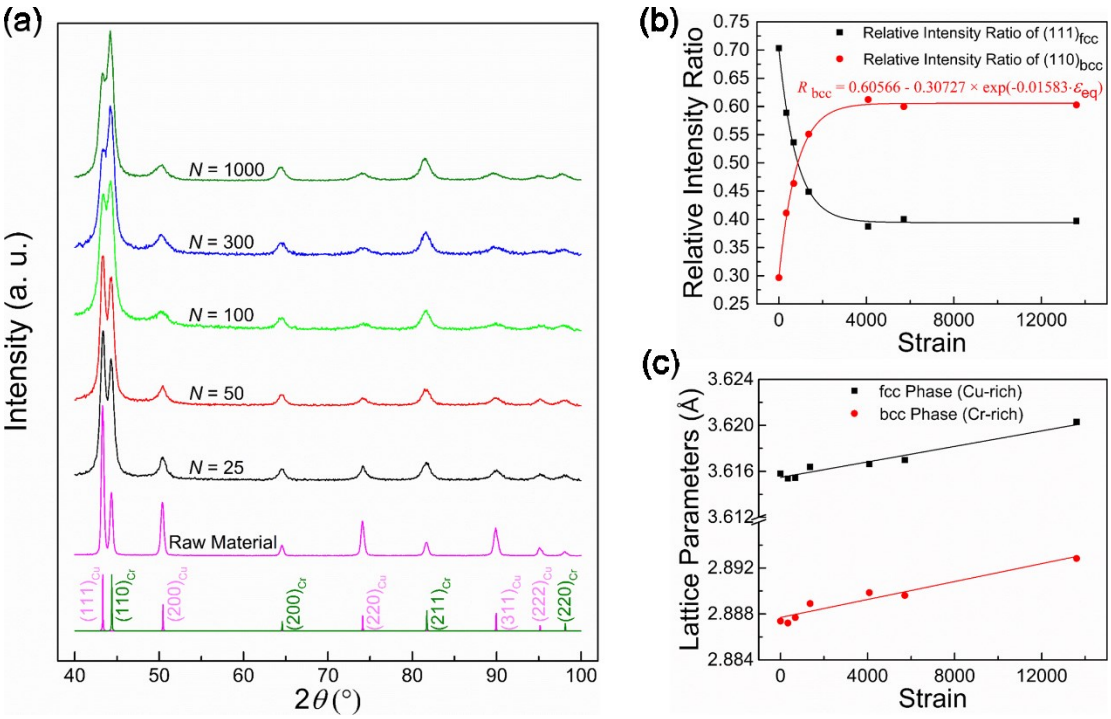

Fig. 2. (a) XRD patterns of 57 wt.%Cu - 43 wt.%Cr raw material and as-deformed samples with different numbers of rotations. (b) Relative intensity ratio changes of $(111)_{Cu}$ and $(110)_{Cr}$ with different numbers of rotations. (c) Lattice parameters of Cu and Cr phase calculated from $(111)_{Cu}$ and $(110)_{Cr}$ diffraction peaks.

To investigate the relationship between relative intensity ratio and dissolution of Cu, namely, what percentage of Cu has been dissolved into Cr matrix after different numbers of rotations,

XRD spectra of blended powders with different ratios of x wt.%Cu - (1-x) wt.%Cr (x = 5, 15, 35, 65, 85) were measured to calculate the relative intensity ratio changes of $(111)_{Cu}$ and $(110)_{Cr}$ peaks with different compositions. The XRD measurement curves and calculated ratios were plotted in Supplementary Fig. S1a and Fig. S1b respectively. The curve in Supplementary Fig. S1b was used as a reference in this work to calculate the quantity of each phase in the deformed alloys. Table 1 shows the percentage of residual Cu phase in the first row and the already dissolved percentage of Cu phase in the second row. Finally, after HPT deformation with 300 rotations or even higher, 32 wt.% (27.8 at.%) Cu can be fully dissolved into the Cr phase bcc structure. The confirmation results with blended powders of 30 wt.%Cu - 70 wt.%Cr will be addressed later to show the accuracy of calculation of this method.

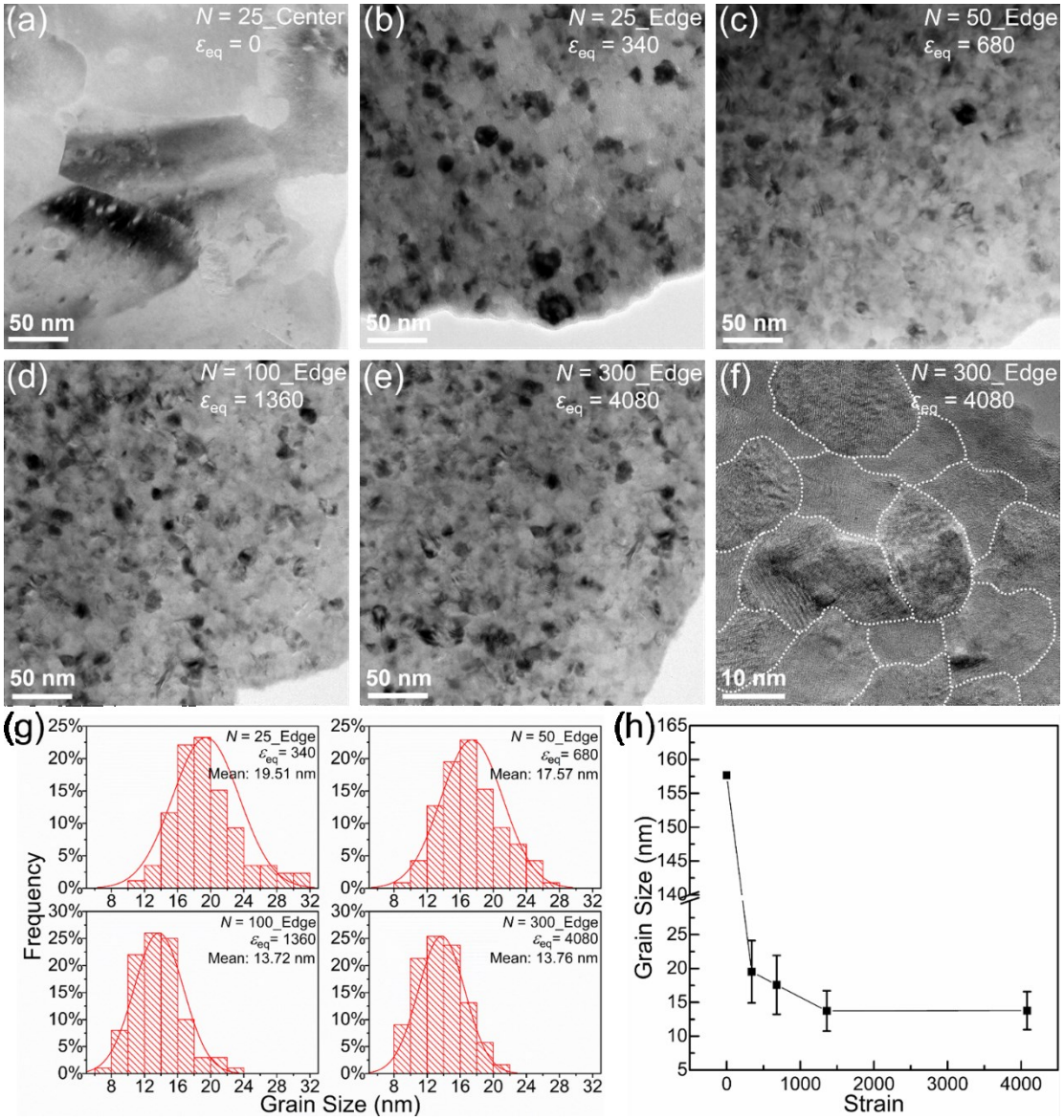

Fig. 3. TEM bright field images taken at the same magnification (images a – e), and high magnification image of edge part of deformed sample with 300 rotations (image f). For the

TEM sample made from the center part of HPT deformed disk with 25 rotations, the perforation of TEM sample was exactly in the center of HPT disk. For all the TEM samples made from the edge part of HPT deformed disks, the perforation of TEM samples were exactly at the radius of 3 mm of HPT disks. (g) Histogram distributions of grain size statistics of Cu-Cr alloys deformed with different numbers of rotations. Each histogram was based on measurements of a minimum of 100 grains. (h) Average grain size values of samples deformed with different numbers of rotations with error bar of standard deviation.

3.2 Microstructure characterization

Figs. 3a-f show the TEM bright field images of Cu-Cr samples deformed with different numbers of rotations. The average grain size can be observed to be decreased as the increasing of numbers of rotations. For all the samples deformed by HPT, grains are equiaxed and randomly distributed, and with almost spherical shape. This also facilitates statistic measurement of grain size regarding the grain as a sphere and the diameter of the sphere is the calculated grain size [17]. It is worth noting that the average grain size in the central part of HPT deformed disk with 25 rotations is in the order of 100 nm to 200 nm based on the TEM images. Theoretically, the grain size in the center of HPT disk should be the same with starting bulk material in micron scale in ideal case if the torsional axis is in perfect condition without deviation and the perforation of TEM sample is small enough and in the exact center of HPT disk. In practice, the center of HPT disk may be also slightly deformed due to the little deviation of torsional axis [29,37,38]. Anyway, it will not affect the results mentioned in this work. For other edge part samples, the average grain size is quickly decreased to the order of 10 - 20 nm rather than amorphization reported in 30 at.%Cu - 70 at.%Cr alloy generated by ball milling [39].

Fig. 3g shows the grain size distribution of Cu-Cr alloys deformed with different numbers of rotations. Fig. 3h shows the change of average grain size with an error bar of standard deviation. The average grain size of sample deformed with 25 rotations is 19.5 nm with a relatively wide distribution compared with the sample deformed with 300 rotations with average grain size of 13.7 nm and narrower distribution. The grain size change indicates that grain refinement was finished in the initial stage of deformation. Due to the nearly same volume amount of Cu and Cr in this composition of 57 wt.%Cu - 43 wt.%Cr, grinding of each part during HPT deformation is easy to proceed in spite of the large difference of hardness between Cu and Cr, rather than swimming in some compositions with large proportion of Cu and little part of Cr.

Fig. 4 shows the high resolution TEM (HRTEM) images of HPT deformed 57 wt.%Cu - 43 wt.%Cr alloy with 100 rotations. Fig. 4a shows three adjacent grains of Cu and Cr with different zone axes. The grain in right side is Cu with fcc structure and on the zone axis of [011] which is parallel to the incident electron beam while the bottom-left grain is chromium with bcc structure and on the zone axis of [001]. In this image, $(1\bar{1}0)_{Cr}$ plane of Cr grain is strictly parallel to $(1\bar{1}1)_{Cu}$ plane of Cu grain, which is the typical matching relationship of bcc and fcc structure with $\{110\}_{bcc}//\{111\}_{fcc}$ [13,40,41]. In the top-left corner, the grain is not well on zone axis, but $\{111\}_{Cu}$ planes can still be distinguished from the results of spacing measurement. Fig. 4b shows a grain of Cu with fcc [001] zone axis. Form this image, $(200)_{Cu}$, $(220)_{Cu}$ and $(020)_{Cu}$ can be observed here according to Fast Fourier Transform (FFT) in upper-left corner derived from the area marked with white frame. For the FFT image, except the main spots indexed with the zone axis of $[001]_{fcc}$, there are some weak spots close to the central spot. After checking

the interplanar spacing represented by these spots, oxides of CuO, Cu_2O and Cr_2O_3 can be recognized with structure of monoclinic, cubic and hexagonal structure respectively [42,43]. $(011)_{CuO}$, $(101)_{CuO}$, $(110)_{Cu2O}$ and $(110)_{Cr2O3}$ have been indexed in the FFT. Fig. 4c shows a typical small angle grain boundary between two Cr grains with matching plane of (110). From FFT images calculated from the white frames of both left and right part, these two Cr grains both possess bcc structures with zone axis of [111]. Compared with clear atom columns of right Cr grain, the left image doesn't show distinct interplanar planes except $(110)_{Cr}$ plane, even though all spots with zone axis of $[111]_{bcc}$ in FFT can be observed. This may be caused due to a tiny in-plane tilt of (110) plane in left grain. At grain boundary, dislocations can be observed directly marked in the white circles. Based on HRTEM image, this grain boundary can be deduced to be a typical symmetrical tilt boundary with a splitting angle of 13.3˚. The relationship of spacing *d* and distance between two dislocations fits well with $\sin\theta = \frac{d}{a}$ [14]. One should note that at the bottom right of this image which is marked with a white ellipse, there is one part of right grain which shows planes almost on $[001]_{bcc}$ zone axis. But the rest part of right grain crossed the white dash line shows obvious $[111]_{bcc}$ zone axis. This coexistence of two subareas with zone axes of $[111]_{bcc}$ and $[001]_{bcc}$ inside one Cr grain should be due to the deformation-induced local transition from <001>-oriented bcc structure to <111>-oriented lattice, which is similar as phase transition in bcc molybdenum caused by *in-situ* straining [44]. Fig. 4d shows an atomic-scale twin boundary with a zone axis of fcc [011]. At the top-right part of the image, there are some areas with different contrast and latticed shape (Moiré fringes), probably due to the grain overlapping.

3.2 Hardness measurements

To check the mechanical properties, hardness of Cu-Cr alloys deformed with different numbers of rotations was measured systematically as shown in Fig. 5. The inset shows the enlarged hardness results with relatively low strain range of 0 – 1800. Generally, the increment of hardness as a function of strain can be divided into 3 stages. The hardness value increased with increasing strain quickly in the initial stage of deformation with a lower strain less than 400. Here the fast increasing of hardness was due to the combination of contributions of grain refinement and formation of solid solutions. According to the calculation of dissolution process, about 18 wt.% Cu was dissolved into Cr matrix when the given strain was about 400 (equivalent to the strain of position at radius of 3 mm deformed with 29 rotations). But the average grain size was reduced fast from more than 150 nm to less than 20 nm. When the strain reached about 400, the hardness value increased to about 440 from the initial value of about 280 for the center point of HPT disk deformed with 25 rotations correlated with the average grain size of about 158 nm. For the second stage when the strain increased from 400 to about 4000 (equivalent to the strain of position at radius of 3 mm deformed with 294 rotations), about 9% of hardness value was improved from 440 to 480. From the calculation of grain size, the average grain size was reduced to about 19.5 nm when the sample was deformed with 25 rotations. The equivalent strain at the radius of 3 mm for the sample deformed with 25 rotations was about 340. Then as the increase of strain, the grains were only slightly refined within the range of 13.7 – 19.5 nm. But the dissolution of Cu into Cr matrix was finally improved from 18 wt.% at the strain of 400 to about 32 wt.% at the strain of 4000. So for the second stage of relative small increment of hardness, the main contribution for the 9% improvement of hardness should come from the formation of solid solution of bcc structure of Cu-Cr composite. Simultaneously, we can roughly deduce that in the initial stage of deformation the main contribution of hardness increasing should come from the grain refinement due to the large

increasing of hardness with about 57% increment. For the third stage, when the strain reached about 4000, the dissolution of Cu into Cr became saturated which was consistent with the stabilization of hardness value. The hardness value was invariable within the range of 480 – 495 HV even the sample was deformed with extremely high strain to 16000 which had never been tried before. For the solubility limit, total 32 wt.% Cu can be dissolved into Cr matrix. The grains were also refined uniformly with average size of 13.7 nm after deformation with large strains. So the maximum of dissolution and grain refinement caused the highest hardness value of about 495 for 57 wt.%Cu - 43 wt.%Cr composites obtained by mechanical alloying.

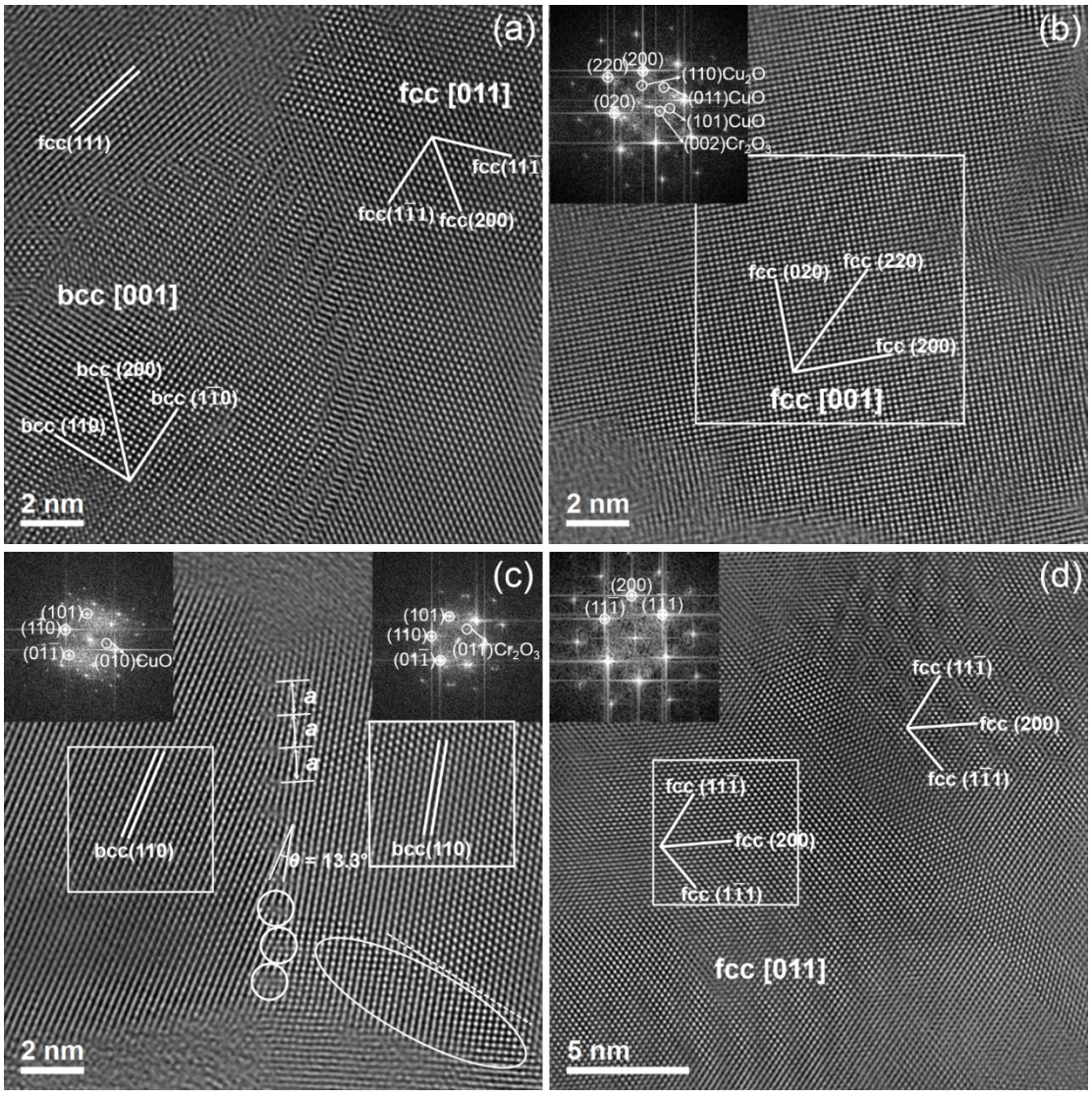

Fig. 4. HRTEM images of 57 wt.%Cu - 43 wt.%Cr alloys after HPT deformation with 100 rotations. (a) Three adjacent grains of Cu and Cr with different zone axis. (b) Cu grain with fcc structure on zone axis of [001]. (c) Small angle grain boundary in two Cr grains with matching plane of $(110)_{bcc}$. (d) Twin boundary in atomic scale in nano-size with zone axis of $[011]_{fcc}$.

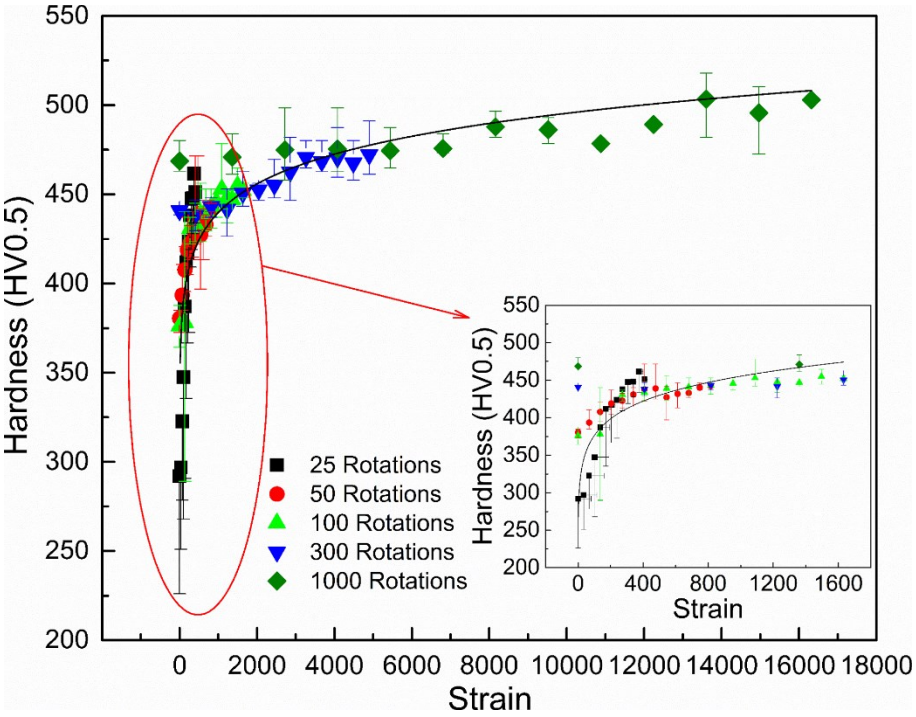

Fig. 5. Hardness measurements of Cu-Cr alloys deformed with different numbers of rotations. The inset shows the enlarged hardness results with a strain range of 0 – 1800.

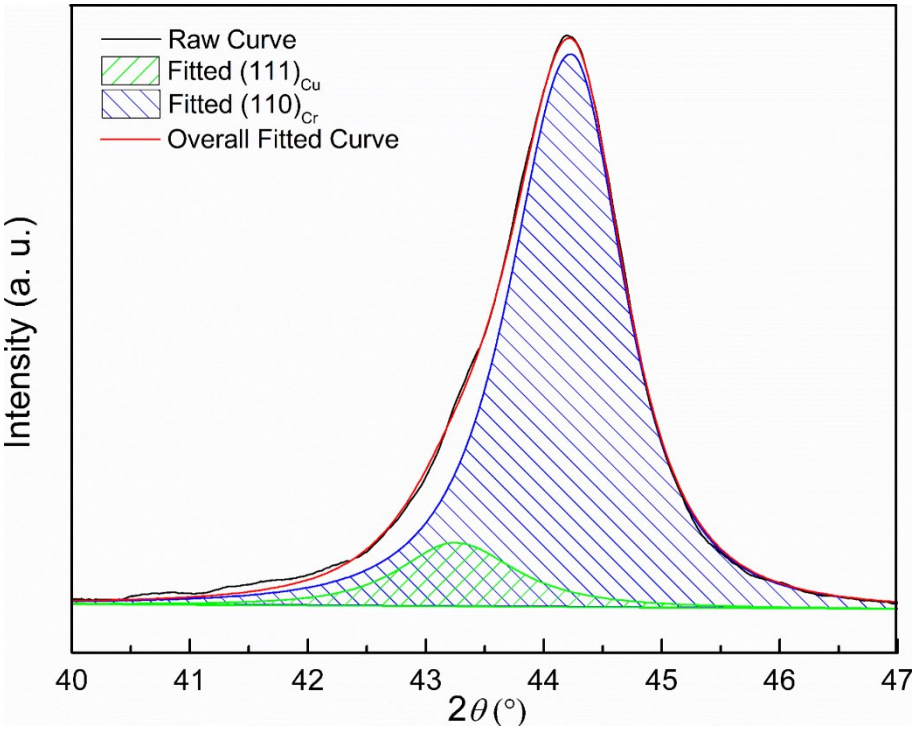

Fig. 6. XRD curve of fine scanning in range of 40˚ – 47˚ for the sample of 30 wt.%Cu - 70 wt.%Cr deformed with 50 rotations at the second stage.

3.4 Verification experiments of blended powders of 30Cu-70Cr and melted bulk of 95Cu-5Cr

As mentioned in the experimental part, nominal 30 wt.%Cu - 70 wt.%Cr composition was deformed using powders as raw material with two-stage method. Fig. 6 shows the fine scanning XRD curve measured from the edge part of the disk of 30 wt.%Cu - 70 wt.%Cr deformed with 50 rotations at the second stage. The measured curve only displayed one broadened peak. But due to the slightly unsymmetrical shape of the peak, the fine fittings of $(111)_{Cu}$ and $(110)_{Cr}$ were carried out to separate the measured curve. The overall fitted curve (red) accorded well with the measurement result (black), meaning good accuracy of fitting. Then the relative intensity ratio of $(111)_{Cu}$ can be easily calculated based on the fitting result. Referring to Supplementary Fig. S1b (the relationship between relative intensity ratio of $(111)_{Cu}$ and weight percentage of Cu phase in blended powders), about 3 wt.% (2.5 at.%) Cu can be identified as residual phase in the composite. That is, about 27 wt.% Cu in the composite was successfully dissolved into Cr matrix after the second stage of deformation with 50 rotations. As described in Ref. [5], the total strain after two stages HPT deformation, should be multiplication of strain of each stage. For the first stage of this sample, the strain is about 40 calculated from equation (1) considering 8 mm of the sample thickness and 9 mm of the distance at radius. For the second stage, the strain at the radius of 3 mm with 50 rotations is about 680. So theoretically the total strain at point of 3 mm far away in radius should be 27200. The reason for that 3 wt.% residual Cu was still detected according to XRD in the deformed composite even after deformation with strain of 27200, is that, the starting materials were powders rather than melted bulk material like 57 wt.%Cu - 43 wt.%Cr. The 30 wt.%Cu - 70 wt.%Cr is extremely hard due to the large fraction of Cr, the processing anvils were easily damaged during deformation, so no higher strain was tried. Anyhow, current XRD result is sufficient to show that at least about 27 wt.% Cu can be dissolved into Cr by HPT method although the needed strain is different due to the difference of starting materials.

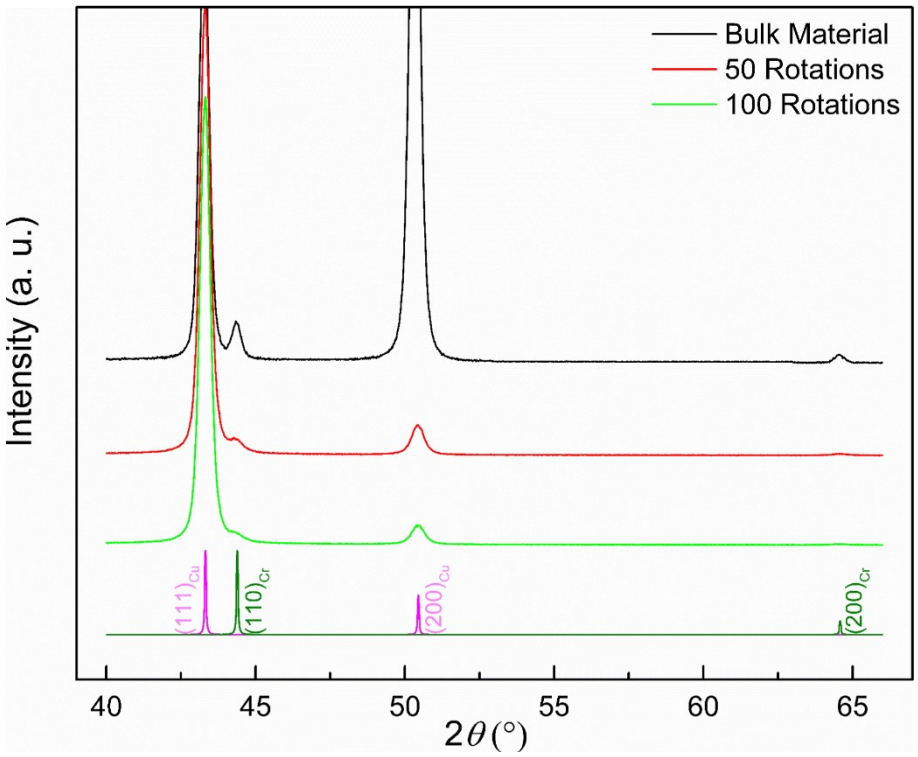

Fig. 7. XRD curves in range of 40˚ – 66˚ for the raw bulk material and samples of 95 wt.%Cu - 5 wt.%Cr alloy deformed with 50 and 100 rotations.

The dissolution limit of Cu into Cr was determined based on HPT deformation of 57 wt.%Cu - 43 wt.%Cr. The same method was used on the composite of 95 wt.%Cu - 5 wt.%Cr to determine the solubility limit of Cr into Cu. Fig. 7 shows the XRD curves of the bulk material and deformed samples with 50 and 100 rotations. All the curves were normalized by $(111)_{Cu}$. The melted bulk material was thinned down by rolling, so the sample showed partial (200) texture. After HPT deformation, the texture disappeared and the Cr peak obviously decreased. Compared to the curve measured from the sample deformed with 50 rotations, the intensity of Cr peaks from 100 rotations deformed sample reduced further but these peaks still can be observed. After referring to Supplementary Fig. S1b, about 2 wt.% of Cr phase was left, which meant about 3 wt.% (3.6 at.%) Cr has been successfully dissolved into Cu matrix to form fcc structure. This result is consistent with the value of Cr solubility in Cu of 4 at.% (3.3 wt.%) in Cu-Cr thin films deposited by molecular beam epitaxy [45].

Table 1

Residual percentage of Cu phase and dissolved percentage of Cu phase after different numbers of rotations.

Rotations	$N = 25$	$N = 50$	$N = 100$	$N = 300$	$N = 1000$
Residual Cu (wt.%)	35.5	31.1	24.5	21.0	21.2
Dissolved Cu (wt.%)	17.5	21.9	28.5	32.0	31.8

4. Discussion

4.1 Chemical composition verification

To verify the exact compositions of HPT deformed Cu-Cr alloys, we performed sub-nanometer scale EDXS measurements on the samples deformed with different strains. Fig. 8a shows one HAADF-STEM image of 57Cu-43Cr alloy deformed with 100rotations where the dark areas are Cr grains and the bright areas represent Cu grains. Systematical line-scan of EDXS measurements can be implemented across Cu and Cr grain boundaries. Fig. 8b and Fig. 8d show the HAADF-STEM images of 57Cu-43Cr alloys deformed with 25 rotations and 100 rotations respectively. Fig. 8c and Fig. 8e show the weight percentage concentration profiles measured across Cu and Cr grains along the white arrowline showed in STEM images Fig. 8b and Fig. 8d respectively. The spacing between two measurement ponits for EDXS line-scan is 1.4 nm with a electron probe size of 0.7 nm. All EDXS measurements shown here were obtained at the extremely thin area of edge part to insure no overlapping of grains (beam broadening effect is negligible). For sample deformed with 25 rotations, the concentration profile in Fig. 8c obviously shows that in Cr grains the average amount of Cu is about 19.6 wt.% (16.6 at.%), while in the Cu grain side, the dissolved Cr amount is about 3.8 wt.% (4.6 at.%). When 57Cu-43Cr was deformed with 100 rotations, the concentration profile in Fig. 8e shows that about 30.5 wt.% (26.4 at.%) of Cu stoms has been dissolved into Cr grains, simultaneously Cu grains contain about 3.9 wt.% (4.7 at.%) Cr dissolved inside. In addition, 10 point measurements at respective Cu and Cr grains were performed in the sample deformed with 100 rotations to confirm the results, as showed in Supplementary Table S1. The average amount of Cu atoms in Cr grains is about 30.6 wt.% (26.5 at.%) and Cr amount dissolved into Cu grains is about 4.1 wt.% (4.9 at.%), which is fully consistent with the results showed in EDXS line-scan. Compared with the results showed in Table 1, the dissolved amount of Cu into Cr should be 17.5 wt.% (14.8 at.%) and 28.5 wt.% (24.6 at.%) when the samples were deformed with 25 rotations and 100 rotations respectively according to the XRD method. The results obtained from different methods have a little difference, but with the same change trend, that is, larger strains cause higher dissolution amount. The main reason of this small difference may be due to the different scales of these two methods. Anyway these results are quite convictive information to understand the strain-dependent dissolutions of 57Cu-43Cr systems.

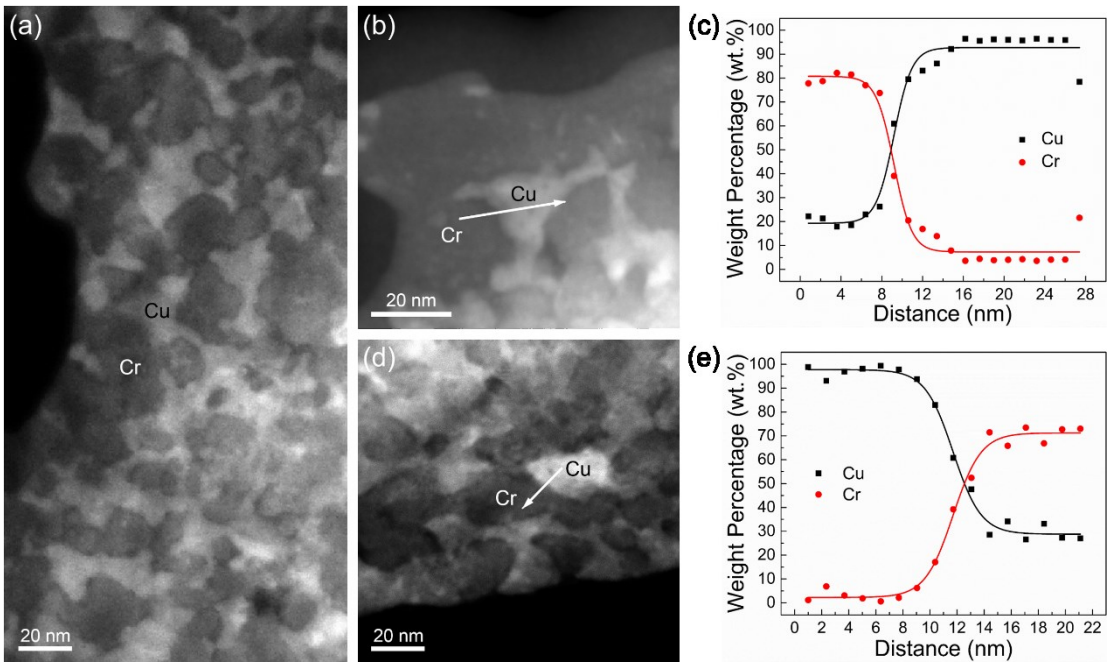

Fig. 8. HAADF-STEM images of HPT deformed samples of 57Cu-43Cr alloy: (a, b) 25 rotations. (d) 100 rotations. Concentration profiles of EDXS line-scan measurements across Cu and Cr grains along the white arrowline showed in STEM images: (c) 25 rotations. (e) 100 rotations.

4.2 Dissolution process of HPT deformed Cu-Cr alloys

As mentioned in introduction part, for the dissolution process of alloys generated by mechanical alloying, there were many discussions about the non-equilibrium state from different points of view. Ma *et al.* [31,46] and Martin [47] have discussed the dissolution process quantitatively in non-equilibrium state to determine the largest solubility (For details, see discussion in Supplementary). Even though the phenomenological model in their work is relatively rough and based on the ball milling process, but it can empirically explain the increase of solubility due to the external forcing. But this description cannot intuitionally tell the dissolution process of the alloys under continuous deformation. Actually some literatures reported the alloying process could be a competition between mixing under sustained external forcing and decomposition due to thermal diffusion [31,32,46–48]. Based on our experimental results, we have proposed an empirical formula to mimic the details and influencing parameters of dissolution process based on our experimental data [49]. The idea of thermodynamics-related diffusion was employed to describe the inverse flow of dissolved solute atoms during deformation. In our previous work [49], the thermodynamic diffusion flux J^{th} was deduced with a relationship of applied strain ε_{eq} (Equation (3) in literature [49]):

$$J^{th} = J^{f} \cdot \frac{1}{k} e^{k(\tau - \varepsilon_{eq})} \tag{3}$$

Eq. (3) shows that J^{th} is a negative exponential function of applied strain ε_{eq}, where κ and τ are coefficients, and J^{f} means external forcing mixing flux. So it will increase as the increasing of strain, but with an approaching value. Two boundary conditions should be

considered for this equation. First, when ε_{eq} is 0, J^{th} should equal to 0, which means $J^f = \frac{1}{k}e^{k\tau}$. Second, when $\varepsilon_{eq} \to +\infty$, $J^{th} = J^f$, that is, the approaching value is J^f and the system has arrived a balanced state with equivalent speed between forcing mixing and thermodynamic diffusion.

The external forcing flux J^fkeeps constant during deformation, while the thermodynamic decomposition flux J^{th} shows a negative exponential increasing trend. When the sample is deformed with high strains, the back-diffusion flux increases close to the level of forcing flux due to the large amount of net Cu solute atoms, so the dissolution of Cu atoms into Cr matrix gets saturated (Refer to Fig. 3 in literature [49]). So the final percentage of Cr phase R_{Cr} which involves the integration of net flux J can be also given in a negative exponential increasing, as shown in equation (4):

$$R_{Cr} = C\text{-}A \cdot e^{-\omega \cdot \varepsilon_{eq}} \quad (4)$$

where *A* and *C* are positive constants. In Fig. 2b, the experimental data of Cr phase percentage in the deformed alloys was well fitted by negative exponential formula. The equation (4) derived from our diffusion model accords well with previous fitting formula in Fig. 2b. Namely, C = 0.60566, A = 0.30727 and ω = 0.01583.

Here a model without consideration of the solid solution in equilibrium condition was proposed to describe the dissolution process in non-equilibrium state due to the negligible solubility for the "immiscible" Cu-Cr alloy even at eutectic melting temperature of 1075 °C [2]. The final equation (4) is in consistent with the experimental results perfectly to describe the dissolution process. Even though the exact implications of constants A, C, ω and k were not given yet, but it doesn't affect the understanding of dissolution process from the phenomenological point of view with this model. Based on previous discussion of solubility of already balanced system from the standpoint of energetics, these parameters should be related to enthalpy and chemical potential of the system. One may have a query that if so called "backflow" diffusion of solute atoms is such significant, why the supersaturated solid solution does not decompose when HPT was removed? Straumal *et al.* interpreted the reason was due to low bulk diffusivity without HPT [18]. Sauvage *et al*. discussed in specific conditions of the HPT process the diffusion coefficient would increase for four orders of magnitude compared with that under the condition without strain [8], basing on the calculation result of that the vacancy migration energy might be lowered by 30% even subjected to a compressive strain of 5% [50]. According to these explanations, the relatively stable phases after HPT may be attributed to that the solute atoms are "frozen" in the bulk and cannot reach the grain boundaries.

This model can be extended to phenomenologically explain the deformation process in other fcc-bcc "immiscible" systems, such as Cu-Fe and Cu-Mo systems. However, two points should be noted: First, for this phenomenological descriptions it is assumed that the phase boundary area is always constant during the process. Actually, in the initial stage of deformation, the refinement is much faster than the supersaturation process, hence, the refinement produce numerous boundaries during the deformation. Our result showed that the grains were refined quickly down to 19.5 nm even with the deformation of 25 rotations, and only a slight refinement to 13.7 nm occurred when the sample was further deformed with 100 rotations. So our proposed model simplified the dissolution process by treating the boundary area unchanged, without consideration of boundary area increasing due to grain refinement in the starting stage of deformation. Second, flux changes of thermodynamic back-diffusion are only

caused by the strain-dependent accumulation of net Cu solute atoms, not by the difference of diffusion coefficient. Our previous investigation on the atomic-scale intermixing of HPT deformed Cu-Cr alloy has confirmed that Cu diffusion coefficient only has a small variation at different temperatures [51]. So here the employment of unchanged diffusion coefficient should be reasonable from empirical point of view.

5. Conclusion

57 wt.%Cu - 43 wt.%Cr was HPT deformed with controllable strains, especially with extremely high strains. Finally, a nanocrystalline alloy was formed with average grain size less than 20 nm and a good homogeneity. Comprehensive characterization methods, including XRD, (HR)TEM, STEM and EDXS were employed to systematically observe and characterize the phase fraction change, nanostructures and sub-nanometer scale compositions. The derived negative exponential intermixing mode was discussed in detail based on the proposed kinetic model. The main conclusions can be summarized as follows:

1. Phase evolution and the extended solubility of Cu-Cr system under HPT process were determined. The dissolution-induced phase change was driven by continuous deformation. The phase fraction change of as-deformed Cu-Cr alloy showed an obvious negative exponential trend. This work showed that about 32 wt.% (27.8 at.%) of Cu can be fully dissolved into Cr matrix to form bcc structure using HPT method. Only about 3 wt.% (3.6 at.%) Cr can be dissolved into Cu phase even the sample was deformed with 100 rotations.
2. The grain refinement of 57 wt.%Cu - 43 wt.%Cr sample was finished almost at the starting stage. When the sample was deformed with 25 rotations, the average grain size was decreased dramatically from micron-scale to less than 20 nm. Only a slight further refinement to average size of 13.7 nm occurred even the sample was deformed to 100 rotations.
3. Hardness value of 480 – 495 was obtained when the deformation rotations reached 100 rotations or even higher. At the starting stage, the fast increasing of hardness mainly comes from the grains refinement. For later stage, the slight increment is mainly due to increased amount of dissolution of Cu atoms into Cr matrix.
4. Kinetic dissolution model was proposed in this work based on the idea of that final solubility was determined by the competition of external forcing mixing and thermodynamic decomposition. The obtained negative exponential formula fits well with our experimental data. From this model and equation, it is easy to know the relationship between dissolved Cu solute amount and applied strain, which facilitates the understanding of dissolution process.

Acknowledgements

We gratefully acknowledge the financial support by the Austrian Science Fund (FWF): No. P27034 - N20. Peter Kutleša, Gabriele Moser, Herwig Felber and Silke Modritsch at Erich Schmid Institute of Materials Sciences, Austrian Academy of Sciences, are gratefully acknowledged for their help with the HPT, TEM and metallographical samples preparation.

Appendix: Supplementary data

1. X-ray diffraction results of compacted Cu-Cr powders with different compositions

To investigate the relationship between relative intensity ratio and dissolution amount of Cu, namely, how much percentage of Cu has been dissolved into Cr matrix after different numbers of rotations, the blended powders with different ratios of *x* wt.%Cu - (1-*x*) wt.%Cr (*x* = 5, 15, 35, 65, 85) were measured using XRD to calculate the relative intensity ratio changes of $(111)_{Cu}$ and $(110)_{Cr}$ peaks with different compositions. The XRD measurement curves and calculated ratios were plotted in Supplementary Fig. S1a and Fig. S1b respectively. The curve in Supplementary Fig. S1b was used as a reference in this work to calculate the quantity of each phase in the deformed alloys. Table 1 in text part shows the percentage of residual Cu phase in the first row and the already dissolved percentage of Cu phase in the second row. For the starting bulk material, the nominal percentage of Cu was about 57 wt.%. However the content of Cu calculated from the presented method here was about 53 wt.% for starting material. Anyhow, this small difference will not affect the accurate calculation of dissolution amount of Cu, because the results listed here all came from XRD calculation regarding the starting Cu phase 53 wt.% as the same baseline. Finally, after HPT deformation with 300 rotations or even higher, 32 wt.% (27.8 at.%) Cu can be fully dissolved into Cr phase forming single bcc structure.

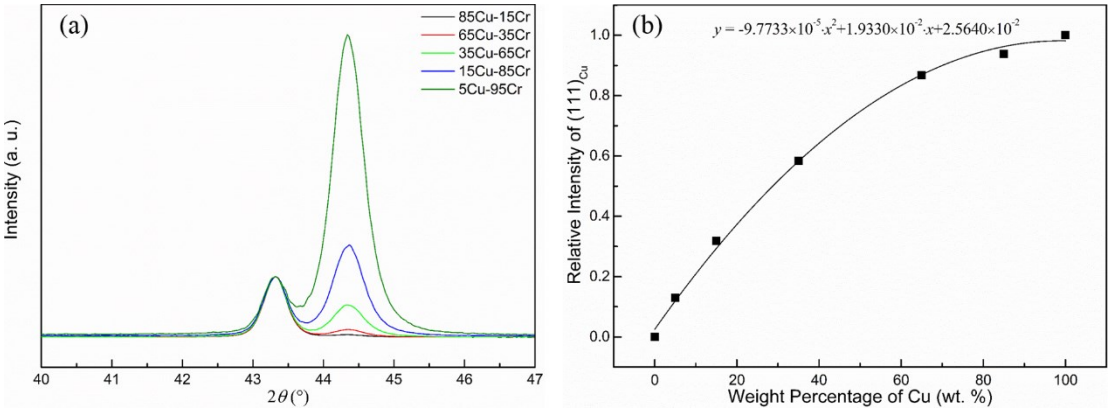

Fig. S1 X-ray diffraction results of compacted Cu-Cr powders. (a) Fine scanning XRD curves of compacted powders with different compositions. (b) Calculated relative intensity ratio of $(111)_{Cu}$ from XRD curves of compacted powders. (A fitted equation is inserted in the graph)

2. 10 additional EDXS point measurements for Cu and Cr grains respectively

10 point measurements at respective Cu and Cr grains were performed in the sample deformed with 100 rotations to confirm the EDXS line-scan results, as showed in Table S1. The average amount of Cu atoms in Cr grains is about 30.6 wt.% (26.5 at.%) and Cr amount dissolved into Cu grains is about 4.1 wt.% (4.9 at.%), which is fully consistent with the results showed in EDXS line-scan.

Table S1 EDXS measurements data of 10 Cu grains and 10 Cr grains in 57Cu-43Cr alloys deformed with 100 rotations.

Number of Cr Grains	1	2	3	4	5	6	7	8	9	10	Average
Cr Percentage (wt.%)	68.1	69.0	73.4	63.2	72.5	71.6	70.5	74.4	68.0	63.1	69.4
Cu Percentage (wt.%)	31.9	31.0	26.6	36.8	27.5	28.4	29.5	25.6	32.0	36.9	30.6
Number of Cu Grains	**1**	**2**	**3**	**4**	**5**	**6**	**7**	**8**	**9**	**10**	**Average**
Cr Percentage (wt.%)	2.3	6.4	3.8	4.8	2.7	3.2	4.1	4.4	3.9	5.6	4.1
Cu Percentage (wt.%)	97.7	93.6	96.2	95.2	97.3	96.8	95.9	95.6	96.1	94.4	95.9

3. Phenomenological model to discuss the largest solubility in non-equilibrium state proposed by Ma *et al.* and Martin.

As mentioned in introduction part, for the dissolution process of alloys generated by mechanical alloying, there were many discussions about the non-equilibrium state from different points of view.

The theory of "capillary pressure" was proposed to explain the dissolution process. The main viewpoint of this theory is that small fragments are generated with tip radii in the order of l nm during deformation so that capillary pressures force the atoms on these fragments to dissolve [1–4]. However, many research works also indicated that, atoms in the tip of fragment are easier to migrate to other regions of the filament with larger radius of curvature through interface diffusion rather than dissolved into the matrix through bulk lattice diffusion. That is, a filament with sharp tips would get spheroidized rather than dissolved. Kinetic models have also been proposed to describe the alloying process as a competition between sustained external forcing during plastic deformation and decomposition due to thermal diffusion [5,6].

In our Cu-Cr system, ultra-fine nanostructured grains with average size of 10 – 20 nm were obtained by applying large strains using HPT method. From the TEM investigations, the grain shape is almost spherical rather than filamentary as showed in high magnification image Fig. 3f. So the kinetic model discussed in "driven system" is more credible for this HPT deformed Cu-Cr alloy [1–5,7]. Ma *et al.* has shown it is energetically possible in ultra-thin sub-nanometer layered structures with thickness of less than 1 nm, excess energies caused due to interfaces and strains can provide a driving force for spontaneous intermixing, or called "inverse spinodal decomposition" [7]. But spontaneous alloying is not possible in solid state interdiffusion reaction even the microstructure is in the range of 1 – 100 nm. If no continuous kinetic forcing is applied, the system itself does not have enough excess energy to resist the positive heat of mixing and then disorder atoms to form a random solid solution in three-dimensional areas. So for the three-dimensional systems, the additional force from external driven processes, such as mechanical deformation, is necessary to form super saturated solid solution in non-equilibrium state [1–5,7].

Ma *et al.* [7,8] and Martin [9] have discussed the dissolution process quantitatively in non-equilibrium state to determine the largest solubility. Even though the phenomenological model in their work is relatively rough and based on the ball milling process, but it is also meaningful to deeply understand the dissolution of "immiscible" system under forcing of external deformation. Porter and Easterling have given the solubility of solute B (α phase) in matrix A (β phase) in equilibrium state as shown in equation (S1) [10]

$$x_B^{eq.} = \exp\{-\frac{\Omega(1-x_B^{eq.})^2+\Delta G_B}{RT}\} \quad \text{(S1)}$$

where ΔG_B is the difference in Gibbs free energy between pure solute B in α phase and β phase, Ω the enthalpy of solution, $x_B^{eq.}$ the equilibrium solubility of B, T the temperature and R the gas constant. According to this equation, the energy term in exponent causes that the positive heating system has extremely low solubility at room temperature of about 300 K, which is so-called "immiscible". But when external forcing was given to the system, the chemical potential of solute B will be raised by the Gibbs-Thomson effect via the term $2\lambda/r$, where λ and r mean interfacial energy and spherical radius of the fine particle of solute B respectively [1,10]. Moreover, the large stresses, applied by continuous deformation externally and also caused due to consequent defects, further changes chemical potential with an effect of the order of σV_m, where σ is the hydrostatic component of the stress tensor and V_m is the molar volume [11]. Simultaneously, "forcing parameters" γ_b was proposed by Martin and Pochet *et al.*, equaling to frequency ratio of ballistic jumps of atoms, to describe the kinetic effects between mixing under external forcing and thermodynamic movements [9,12]. Adding these excess terms into the numerator and denominator of exponent in Eq. (S1), it becomes equation (S2) which indicates the solubility in non-equilibrium state:

$$x_B^{sol.} = \exp\{-\frac{\Omega(1-x_B^{sol.})^2+\Delta G_B-\frac{2\lambda}{r}V_m-\sigma V_m}{RT(1+\gamma_b)}\} \quad \text{(S2)}$$

So just from the equation, it clearly shows that the effective chemical potential is reduced with the minus term of $-(\frac{2\lambda}{r}V_m + \sigma V_m)$, and the total exponent value is further increased due to the multiplication in denominator of the exponent by $(1+\gamma_b)$, which implies the increasing of solubility in non-equilibrium state.

Anyway, from the energetic point of view, equation (S2) can phenomenologically explain the increase of solubility due to the external forcing. But this description cannot intuitionally tell the dissolution process of the alloys under continuous deformation. In many binary systems prepared by severe plastic deformation method, atom probe tomography has been used to exhibit the solute gradients and a strong "solute-solvent" interdiffusion [2,3,13,14]. Actually some works in the literature reported the alloying process could be a competition between mixing under sustained external forcing and decomposition due to thermal diffusion [5,7–9,12]. Mazilkin and Straumal *et al.* observed the almost complete decomposition of Al-Zn supersatured solution during HPT process but less pronounced for Al-Mg alloy [15,16]. They rather thought backflow of solute atoms due to so called "deformation-accelerated diffusion" towards the equilibrium state instead of conventional thermal diffusion played a main role against forcing mixing because of deformation [15].

References of Appendix

[1] A.R. Yavari, P.J. Desré, T. Benameur, Mechanically driven alloying of immiscible elements, Phys. Rev. Lett. 68 (1992) 2235–2238.

[2] X. Sauvage, F. Wetscher, P. Pareige, Mechanical alloying of Cu and Fe induced by severe plastic deformation of a Cu-Fe composite, Acta Mater. 53 (2005) 2127–2135.

[3] X. Sauvage, P. Jessner, F. Vurpillot, R. Pippan, Nanostructure and properties of a Cu-Cr composite processed by severe plastic deformation, Scr. Mater. 58 (2008) 1125–1128.

[4] O. Drbohlav, A.R. Yavari, Mechanical alloying and thermal decomposition of ferromagnetic nanocrystalline f.c.c.-$Cu_{50}Fe_{50}$, Acta Metall. Mater. 43 (1995) 1799–1809.

[5] P. Bellon, R.S. Averback, Nonequilibrium roughening of interfaces in crystals under shear: Application to ball milling, Phys. Rev. Lett. 74 (1995) 1819–1822.

[6] C. Gente, M. Oehring, R. Bormann, Formation of thermodynamically unstable solid solutions in the Cu-Co system by mechanical alloying, Phys. Rev. B 48 (1993) 13244–13252.

[7] E. Ma, H.W. Sheng, J.H. He, P.J. Schilling, Solid-state alloying in nanostructured binary systems with positive heat of mixing, Mater. Sci. Eng. A 286 (2000) 48–57.

[8] E. Ma, J.H. He, P.J. Schilling, Mechanical alloying of immiscible elements: Ag-Fe contrasted with Cu-Fe, Phys. Rev. B 55 (1997) 5542–5545.

[9] G. Martin, Phase stability under irradiation: Ballistic effects. Phys. Rev. B 30 (1984) 1424–1436.

[10] D.A. Porter, K.E. Easterling, Phase transformations in metals and alloys. Chapman and Hall, London, 2nd ed. (1992) 41–47.

[11] J. Eckert, J.C. Holzer, C.E. Krill III, W.L. Johnson, Mechanically driven alloying and grain size changes in nanocrystalline Fe-Cu powders, J. Appl. Phys. 73 (1993) 2794–2802.

[12] P. Pochet, E. Tominez, L. Chaffron, G. Martin, Order-disorder transformation in Fe-Al under ball miling. Phys. Rev. B 52 (1995) 4006–4016.

[13] A. Bachmaier, M. Kerber, D. Setman, R. Pippan, The formation of supersaturated solid solutions in Fe-Cu alloys deformed by high-pressure torsion, Acta Mater. 60 (2012) 860–871.

[14] X. Sauvage, R. Pippan, Nanoscaled structure of a Cu-Fe composite processed by high-pressure torsion, Mater. Sci. Eng. A 410-411 (2005) 345–347.

[15] B.B. Straumal, B. Baretzky, A.A. Mazilkin, F. Phillipp, O.A. Kogtenkova, M.N. Volkov, R.Z. Valiev, Formation of nanograined structure and decomposition of supersaturated solid solution during high pressure torsion of Al-Zn and Al-Mg alloys, Acta Mater. 52 (2004) 4469–4478.

[16] A.A. Mazilkin, B.B. Straumal, E. Rabkin, B. Baretzky, S. Enders, S.G. Protasova, O.A. Kogtenkova, R.Z. Valiev, Softening of nanostructured Al-Zn and Al-Mg alloys after severe plastic deformation, Acta Mater. 54 (2006) 3933–3939.

References

[1] R.Z. Valiev, R.K. Islamgaliev, I.V. Alexandrov, Bulk nanostructured materials from severe plastic deformation, Prog. Mater. Sci. 45 (2000) 103–189.

[2] E. Ma, Alloys created between immiscible elements, Prog. Mater. Sci. 50 (2005) 413–509.

[3] T.D. Shen, C.C. Koch, Formation, solid solution hardening and softening of nanocrystalline solid solutions prepared by mechanical attrition, Acta Mater. 44 (1996) 753–761.

[4] A.R. Yavari, P.J. Desré, T. Benameur, Mechanically driven alloying of immiscible elements, Phys. Rev. Lett. 68 (1992) 2235–2238.

[5] A. Bachmaier, M. Kerber, D. Setman, R. Pippan, The formation of supersaturated solid solutions in Fe-Cu alloys deformed by high-pressure torsion, Acta Mater. 60 (2012) 860–871.

[6] J. Eckert, J.C. Holzer, C.E. Krill III, W.L. Johnson, Mechanically driven alloying and grain size changes in nanocrystalline Fe-Cu powders, J. Appl. Phys. 73 (1993) 2794–2802.

[7] E. Ma, M. Atzmon, F.E. Pinkerton, Thermodynamic and magnetic properties of metastable Fe_xCu_{1-x} solid solutions formed by mechanical alloying, J. Appl. Phys. 74 (1993) 955–962.

[8] X. Sauvage, F. Wetscher, P. Pareige, Mechanical alloying of Cu and Fe induced by severe plastic deformation of a Cu-Fe composite, Acta Mater. 53 (2005) 2127–2135.

[9] X. Sauvage, P. Jessner, F. Vurpillot, R. Pippan, Nanostructure and properties of a Cu-Cr composite processed by severe plastic deformation, Scr. Mater. 58 (2008) 1125–1128.

[10] A. Bachmaier, G.B. Rathmayr, M. Bartosik, D. Apel, Z. Zhang, R. Pippan, New insights on the formation of supersaturated solid solutions in the Cu-Cr system deformed by high-pressure torsion, Acta Mater. 69 (2014) 301–313.

[11] R.K. Islamgaliev, K.M. Nesterov, J. Bourgon, Y. Champion, R.Z. Valiev, Nanostructured Cu-Cr alloy with high strength and electrical conductivity, J. Appl. Phys. 115 (2014) 194301.

[12] S. Sheibani, S. Heshmati-Manesh, A. Ataie, Influence of Al_2O_3 nanoparticles on solubility extension of Cr in Cu by mechanical alloying, Acta Mater. 58 (2010) 6828–6834.

[13] M. Liang, Y. Lu, Z. Chen, C. Li, G. Yan, C. Li, P. Zhang, Characteristics of high strength and high conductivity Cu-Nb micro-composites, IEEE Trans. Appl. Supercond. 20 (2010) 1619–1621.

[14] L. Thilly, M. Véron, O. Ludwig, F. Lecouturier, J.P. Peyrade, S. Askénazy, High-strength materials: *in-situ* investigations of dislocation behaviour in Cu-Nb multifilamentary nanostructured composites, Philos. Mag. 82 (2002) 925–942.

[15] M.J. Demkowicz, L. Thilly, Structure, shear resistance and interaction with point defects of interfaces in Cu-Nb nanocomposites synthesized by severe plastic deformation, Acta Mater. 59 (2011) 7744–7756.

[16] N. Ibrahim, M. Peterlechner, F. Emeis, M. Wegner, S. V. Divinski, G. Wilde, Mechanical alloying via high-pressure torsion of the immiscible $Cu_{50}Ta_{50}$ system, Mater. Sci. Eng. A 685 (2017) 19–30.

[17] D.G. Morris, M.A. Muñoz-Morris, Microstructure of severely deformed Al-3Mg and its evolution during annealing, Acta Mater. 50 (2002) 4047–4060.

[18] B.B. Straumal, B. Baretzky, A.A. Mazilkin, F. Phillipp, O.A. Kogtenkova, M.N. Volkov, R.Z. Valiev, Formation of nanograined structure and decomposition of supersaturated solid solution during high pressure torsion of Al-Zn and Al-Mg alloys, Acta Mater. 52 (2004) 4469–4478.

[19] A.A. Mazilkin, B.B. Straumal, E. Rabkin, B. Baretzky, S. Enders, S.G. Protasova, O.A. Kogtenkova, R.Z. Valiev, Softening of nanostructured Al-Zn and Al-Mg alloys after severe plastic deformation, Acta Mater. 54 (2006) 3933–3939.

[20] S. Lee, A. Utsunomiya, H. Akamatsu, K. Neishi, M. Furukawa, Z. Horita, T.G. Langdon, Influence of scandium and zirconium on grain stability and superplastic ductilities in ultrafine-grained Al-Mg alloys, Acta Mater. 50 (2002) 553–564.

[21] X. Sauvage, N. Enikeev, R. Valiev, Y. Nasedkina, M. Murashkin, Atomic-scale analysis of the segregation and precipitation mechanisms in a severely deformed Al-Mg alloy, Acta Mater. 72 (2014) 125–136.

[22] R.Z. Valiev, T.G. Langdon, Principles of equal-channel angular pressing as a processing tool for grain refinement, Prog. Mater. Sci. 51 (2006) 881–981.

[23] Y. Saito, H. Utsunomiya, N. Tsuji, T. Sakai, Novel ultra-high straining process for bulk materials – development of the accumulative roll-bonding (ARB) process, Acta Mater. 47 (1999) 579–583.

[24] Y. Saito, N. Tsuji, H. Utsunomiya, T. Sakai, R.G. Hong, Ultra-fine grained bulk aluminum produced by accumulative roll-bonding (ARB) process, Scr. Mater. 39 (1998) 1221–1227.

[25] A. Kumar, K. Jayasankar, M. Debata, A. Mandal, Mechanical alloying and properties of immiscible Cu-20 wt.% Mo alloy, J. Alloy. Compd. 647 (2015) 1040–1047.

[26] C. Aguilar, V.deP. Martinez, J.M. Palacios, S. Ordoñez, O. Pavez, A thermodynamic approach to energy storage on mechanical alloying of the Cu-Cr system, Scr. Mater. 57 (2007) 213–216.

[27] A.P. Zhilyaev, T.G. Langdon, Using high-pressure torsion for metal processing: Fundamentals and applications, Prog. Mater. Sci. 53 (2008) 893–979.

[28] A.P. Zhilyaev, G.V. Nurislamova, B.K. Kim, M.D. Baró, J.A. Szpunar, T.G. Langdon, Experimental parameters influencing grain refinement and microstructural evolution during high-pressure torsion, Acta Mater. 51 (2003) 753–765.

[29] A. Vorhauer, R. Pippan, On the homogeneity of deformation by high pressure torsion, Scr. Mater. 51 (2004) 921–925.

[30] M. Kawasaki, R.B. Figueiredo, T.G. Langdon, An investigation of hardness homogeneity throughout disks processed by high-pressure torsion, Acta Mater. 59 (2011) 308–316.

[31] E. Ma, H.W. Sheng, J.H. He, P.J. Schilling, Solid-state alloying in nanostructured

binary systems with positive heat of mixing, Mater. Sci. Eng. A 286 (2000) 48–57.

[32] P. Bellon, R.S. Averback, Nonequilibrium roughening of interfaces in crystals under shear: Application to ball milling, Phys. Rev. Lett. 74 (1995) 1819–1822.

[33] C. Gente, M. Oehring, R. Bormann, Formation of thermodynamically unstable solid solutions in the Cu-Co system by mechanical alloying, Phys. Rev. B 48 (1993) 13244–13252.

[34] A.K. De, D.C. Murdock, M.C. Mataya, J.G. Speer, D.K. Matlock, Quantitative measurement of deformation-induced martensite in 304 stainless steel by X-ray diffraction, Scr. Mater. 50 (2004) 1445–1449.

[35] Y. Xu, S.H. Zhang, M. Cheng, H.W. Song, In situ X-ray diffraction study of martensitic transformation in austenitic stainless steel during cyclic tensile loading and unloading, Scr. Mater. 67 (2012) 771–774.

[36] L.M. Wang, Z.B. Wang, K. Lu, Grain size effects on the austenitization process in a nanostructured ferritic steel, Acta Mater. 59 (2011) 3710–3719.

[37] Y. Huang, M. Kawasaki, T.G. Langdon, An evaluation of the shearing patterns introduced by different anvil alignments in high-pressure torsion, J. Mater. Sci. 49 (2014) 3146–3157.

[38] J. Tao, G. Chen, W. Jian, J. Wang, Y. Zhu, X. Zhu, T.G. Langdon, Anneal hardening of a nanostructured Cu-Al alloy processed by high-pressure torsion and rolling, Mater. Sci. Eng. A 628 (2015) 207–215.

[39] Y. Ogino, T. Yamasaki, S. Murayama, R. Sakai, Non-equilibrium phases formed by mechanical alloying of Cr-Cu alloys, J. Non-Cryst. Solids 117/118 (1990) 737–740.

[40] N.A. Mara, D. Bhattacharyya, R.G. Hoagland, A. Misra, Tensile behavior of 40 nm Cu/Nb nanoscale multilayers, Scr. Mater. 58 (2008) 874–877.

[41] D. Tian, F. Jona, P.M. Marcus, Structure of ultrathin films of Fe on Cu {111} and Cu {110}, Phys. Rev. B 45 (1992) 11216–11221.

[42] W.Y. Ching, Y.N. Xu, K.W. Wong, Ground-state and optical-properties of Cu_2O and CuO crystals, Phys. Rev. B 40 (1989) 7684–7695.

[43] P. Gibot, L. Vidal, Original synthesis of chromium (III) oxide nanoparticles, J. Eur. Ceram. Soc. 30 (2010) 911–915.

[44] S.J. Wang, H. Wang, K. Du, W. Zhang, M.L. Sui, S.X. Mao, Deformation-induced structural transition in body-centred cubic molybdenum., Nat. Commun. 5 (2014) 3433.

[45] T.P. Harzer, S. Djaziri, R. Raghavan, G. Dehm, Nanostructure and mechanical behavior of metastable Cu-Cr thin films grown by molecular beam epitaxy, Acta Mater. 83 (2015) 318–332.

[46] E. Ma, J.H. He, P.J. Schilling, Mechanical alloying of immiscible elements: Ag-Fe contrasted with Cu-Fe, Phys. Rev. B 55 (1997) 5542–5545.

[47] G. Martin, Phase stability under irradiation: Ballistic effects, Phys. Rev. B 30 (1984) 1424–1436.

[48] P. Pochet, E. Tominez, L. Chaffron, G. Martin, Order-disorder transformation in Fe-Al under ball milling, Phys. Rev. B 52 (1995) 4006–4016.

[49] J. Guo, J. Rosalie, R. Pippan, Z. Zhang, On the phase evolution and dissolution process in Cu-Cr alloys deformed by high pressure torsion, Scr. Mater. 133 (2017) 41–44.

[50] K. Sato, T. Yoshiie, Y. Satoh, Q. Xu, M. Kiritani, Simulation of vacancy migration energy in Cu under high strain, Mater. Sci. Eng. A 350 (2003) 220–222.

[51] Z. Zhang, J. Guo, G. Dehm, R. Pippan, *In-situ* tracking the structural and chemical evolution of nanostructured CuCr alloys, Acta Mater. 138 (2017) 42–51.

III

Insights into shear deformation induced grain refinement and intermixing in ductile-brittle Cu-Cr composite via high pressure torsion

Jinming Guo, Reinhard Pippan, Zaoli Zhang

Erich Schmid Institute of Materials Science, Austrian Academy of Sciences, 8700 Leoben, Austria

Shear deformation processes were captured at the atomic scale in ductile-brittle Cu-Cr composite at the initial stage of straining. The refinement of hard phase Cr experienced elongation until reaching extremely fine lamellar structures, embedded with 1 – 2 nm thick Cu layers at the phase boundaries. Grain refinement and intermixing drastically proceeded in the beginning, and the subsequent deformation mainly facilitated the homogenization of Cu- and Cr-rich regions, finally forming equiaxed grains with sizes of less than 20 nm. In addition, the dissolved Cu was surprisingly observed as 2 nm-sized nanoclusters embedded inside the Cr grains maintaining body-centered cubic structure.

Keywords: Nanocrystalline alloys; High pressure torsion; Deformation process; Grain refinement; Intermixing

The application of severe plastic deformation usually results in significant grain refinement in metals and alloys, and generates supersaturated solid solutions even out of "immiscible" systems [1,2]. Among non-equilibrium systems, Cu-Cr was widely investigated and thought as a promising alloy in potential applications requiring high strength and good thermal stability while without compromising electrical conductivity [3–7]. In our recent work, we have systematically investigated the microstructural evolution, phase volume change and the dissolution mechanism of the Cu-Cr nanocrystalline alloys prepared by high pressure torsion (HPT) with extremely large strains, revealing that a maximum amount of 32 at.% Cu can be fully dissolved into the Cr matrix forming nanostructures with saturated grain sizes of about 13 – 15 nm [8,9]. Meanwhile, the as-deformed Cu-Cr nanocrystalline alloy showed a relatively good microstructural stability under annealing at 420 °C [10].

However, all the previous studies focused on the Cu-Cr composites close to strain-saturated states deformed by HPT. Including other Cu-based ductile-brittle systems, such as Cu-Co [11], Cu-Mo [12], Cu-W [13], the investigations on the deformation processes at the early deformation stage are missing, especially the information at or close to the atomic scale is not available. Here, via the advanced transmission electron microscopy (TEM) we intend to capture the deformation processes in the ductile-brittle Cu-Cr system, including initial elongation, fracture until reaching final structure-saturated stage. Simultaneously, the composition changes can be detected as the increase of applied strains due to the concurrent intermixing of both Cu and Cr phases. The systematical investigations on the grain refinement and the accompanied intermixing can demonstrate the sequence of these two processes at the initial stage during HPT.

The initial bulk materials with nominal composition of 57 wt.%Cu - 43 wt.%Cr (volume and atomic fraction of about 50%) were HPT-deformed with different numbers of rotations N (N = 0.25, 1, 5, 25, 100) under a constant pressure of 7.4 GPa and a rotation speed of 0.4 rotation/min. The equivalent strain ε is calculated using equation given in the Ref. [9]. The morphologies of raw material and as-deformed samples were examined by Scanning Electron Microscope (SEM) LEO Gemini 1525 (Carl Zeiss, Oberkochen, Germany) using backscattered electrons. X-ray diffraction (XRD) was conducted on all samples using Smartlab X-Ray Diffractometer (Rigaku, Japan). Here, it should be emphasized that the X-ray beam irradiated on small pieces of samples with width of 1 mm cut out of the HPT disks from radius of 2.5 to 3.5 mm. TEM and scanning transmission electron microscopy (STEM) characterizations were carried out using a field emission gun transmission electron microscope (JEOL JEM-2100F, Japan) equipped with an image-side spherical aberration corrector and an Oxford INCA Energy TEM 200 energy-dispersive X-ray spectroscopy (EDXS) system. All microstructural investigations were undertaken at radius of 3.0 mm from the torsional axes of the HPT deformed disks. Vickers microhardness measurements were conducted on a Buehler Mircomet 5100 using a load of 500 g (HV0.5).

The overall microstructural characterizations on initial material and as-deformed composites were conducted via SEM and XRD as shown in Fig. 1. Figs. 1(a - e) show backscattered electron micrographs of (a) raw material and samples deformed with different numbers of rotations: (b) N = 0.25, (c) N = 1, (d) N = 5, (e) N = 25. The shear plane is vertical in each of the micrographs. It can be seen that Cu (bright) and Cr (dark) particles with average sizes of about 50 μm distribute homogeneously in the raw material. While the Cu-Cr sample was HPT deformed with 0.25 rotation, the Cr particles were elongated along the radial direction. As the sample was deformed further with 1 rotation, the lamellae of Cr particles become thinner and the aspect ratio was larger compared to the sample with N = 0.25 (Fig. 1b). It can be speculated

that the Cu phase is drastically refined because of its high ductile and relative soft nature, which will be verified by the following TEM image in Fig. 3a. However, the Cr particles are barely seen in Fig. 1d of sample deformed with 5 rotations. The level of microstructural refinement is clearly greater at the vicinity of rim than at the center of the sample due to the radial dependence of the equivalent strain. Only some very fine lamellae appeared at the relatively low strain regions. The comparison of the distinct morphologies in Fig. 1c and Fig. 1d reveals that the fragmentation of Cr particles mainly occurred at the strain condition between 1 rotation (ε = 13.6) and 5 rotations (ε = 68). Further deformation with 25 rotations (ε = 340), e.g. Fig. 1e, no Cr particles can be observed any more.

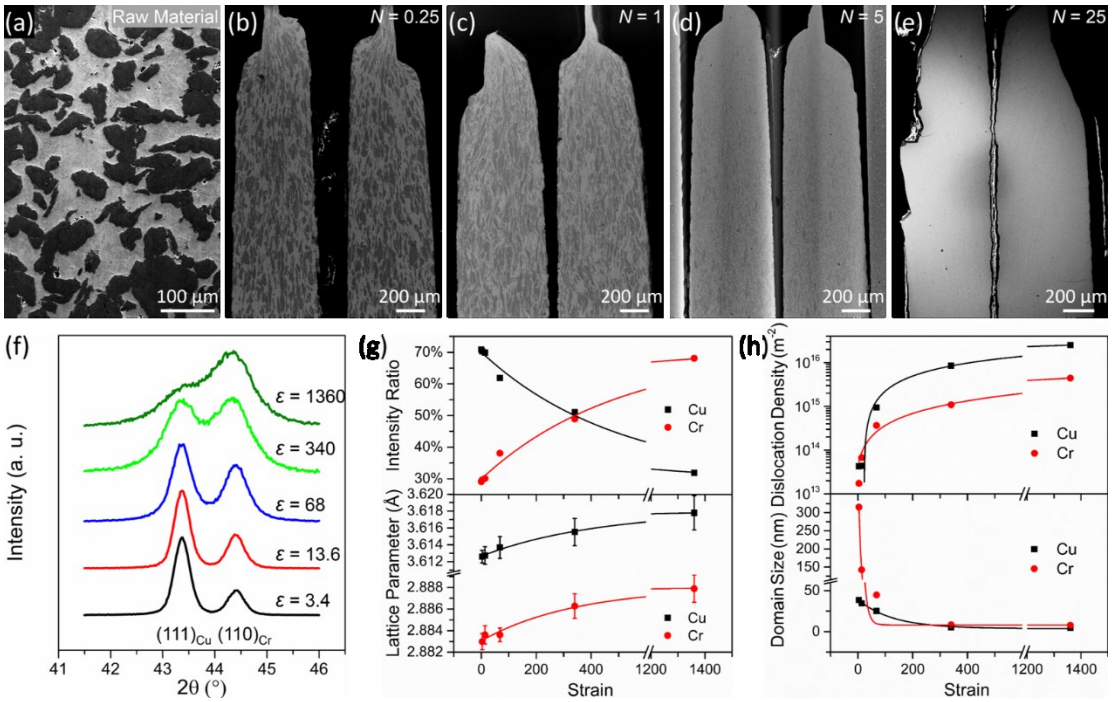

Fig. 1. SEM and XRD characterizations of raw material and as-deformed composites. Backscattered electron micrographs of (a) raw material and samples deformed with different numbers of rotations: (b) N = 0.25, (c) N = 1, (d) N = 5, (e) N = 25. (f) XRD patterns focusing on $(111)_{Cu}$ and $(110)_{Cr}$ peaks of as-deformed samples. (g) Relative intensity ratio and lattice parameter, (h) dislocation density and domain size calculated from XRD patterns as a function of applied strain (ε = 3.4, 13.6, 68, 340, 1360).

Figs. 1 (f - h) show XRD patterns focusing on $(111)_{Cu}$ and $(110)_{Cr}$ peaks of as-deformed samples, and resultant calculations of relative intensity ratio, lattice parameter, dislocation density and domain size respectively as a function of applied strain (ε = 3.4, 13.6, 68, 340, 1360). The XRD patterns in Fig. 1f clearly indicate the relative intensity ratio change between face-entered cubic (*fcc*) and body-centered cubic (*bcc*) structures. The calculated relative intensity ratio and lattice parameter of respective Cu and Cr phase are plotted in Fig. 1g. The relative intensity ratio of Cr phase continuously increases as the strain increases, from 29% of sample deformed with 0.25 rotation to 68% of sample deformed with 100 rotations. Because the texture in the as-deformed Cu-Cr alloy is negligible, so the change of relative intensity ratio can be correlated with the change of phase volume during HPT deformation [8,9,14,15], which

is confirmed by the EDXS line-scan measurements in the following. The lattice parameters of both Cu phase and Cr phase increase slightly as the accumulation of strain, which is in agreement with the lattice expansion reported for Cu-Cr alloys in literature [9,16]. Due to the very close atomic radius of Cu and Cr, i.e. 127.8 pm and 128.0 pm respectively, the lattice parameters of both phases should retain almost invariant according to Vegard's law. However, the actual subtle expansions could be attributed to elastic strains present in the positive heat of mixing systems [2,17].

Fig. 1h displays the dislocation densities and domain sizes calculated based on XRD full range patterns according to Williamson-Hall plot [18–21]. It can be seen that the dislocation densities increase continuously, accompanied with a fast decrease of domain size which denotes the spacing between incoherent structures under the deformation of first 5 rotations (equivalent strain ε less than 68). Unlike the continuous increase of dislocation densities, domain sizes reach saturated values of several nanometers after deformation of 25 rotations (ε = 340). The decrease of domain size depicts an obvious tendency of that grain refinement (or resultant generation of subgrains) almost completed before the strain of about 120 (8 - 9 rotations). It has been well documented that grain refinement is a dynamic process between the hardening rate introduced by dislocation generation and the recovery rate arising from dislocation annihilation and recombination [22]. Hence, the dramatic refinement at the initial deformation stage is clearly correlated with the dislocation multiplication in both phases. Moreover, one can note that the large difference of domain size between Cu and Cr phases even at the extremely low strain condition of 3.4 (0.25 rotation), which is attributed to the soft-hard and ductile-brittle features of Cu and Cr phases respectively. The deformation of Cu phase happens immediately when the strain is applied, inducing instantaneous refinement which is distinct from Cr phase.

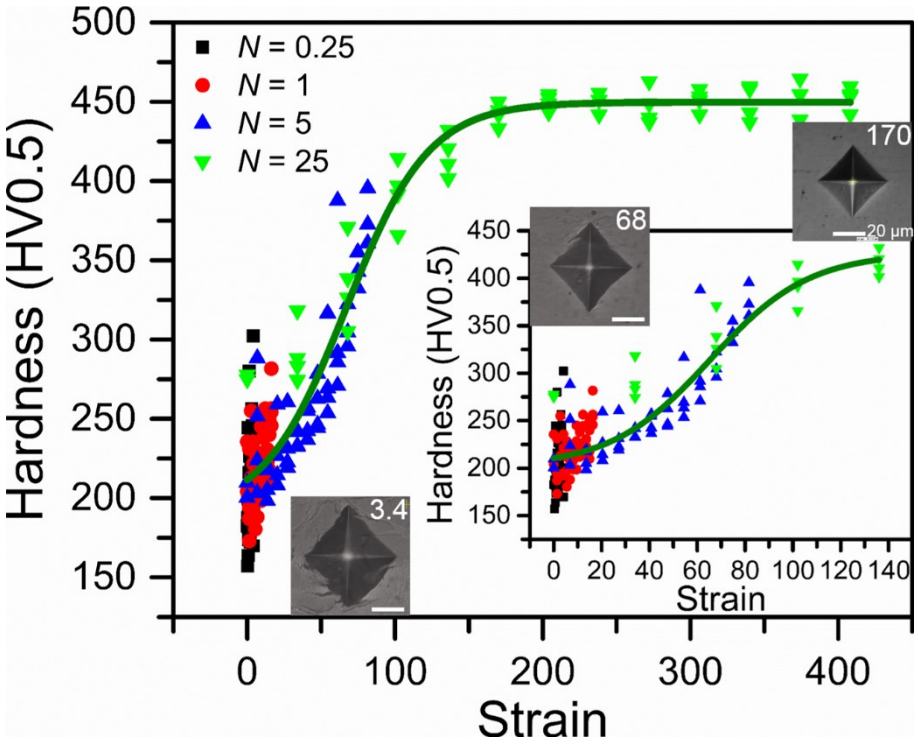

Fig. 2. Microhardness of as-deformed samples plotted against applied strain. The enlarged plot at the bottom right focuses on the hardness at the low strain range, and three indent micrographs recorded at different strain conditions (ε = 3.4, 68, 170) are inserted.

To examine the mechanical properties, hardness of Cu-Cr alloys deformed with different numbers of rotations was measured systematically as shown in Fig. 2. The inset shows the enlarged hardness results in a relatively low strain range of 0 – 140, and three indent micrographs recorded at different strain conditions (ε = 3.4, 68, 170) are also inserted. Generally, the increment of hardness as a function of strain can be divided into three stages. The hardness value slowly increases at the initial stage of deformation with a lower strain less than 20 (1.5 rotations). At this stage, the Cr particles are elongated and thinned but still in the range of several tens of microns as shown in Figs. 1(b, c), resulting in irregular indent crossing different phases. The indent micrograph recorded at strain of 3.4 has large cracks which may initiate from the brittle Cr particles. When the sample is deformed at the second stage with strain from 20 to120, hardness increases quickly from about 220 HV to 415 HV due to the dramatic domain refinement of both phases, especially for Cr (as shown in Fig. 1h), from initial ~325 nm drop to less 25 nm. The third stage begins at the strain point of 120 where grain refinement has almost completed. The hardness rises from 415 HV to a saturated value of ~ 450 HV due to a further slight grain refinement. It can be seen that the indent shows a standard square shape without forming any crack.

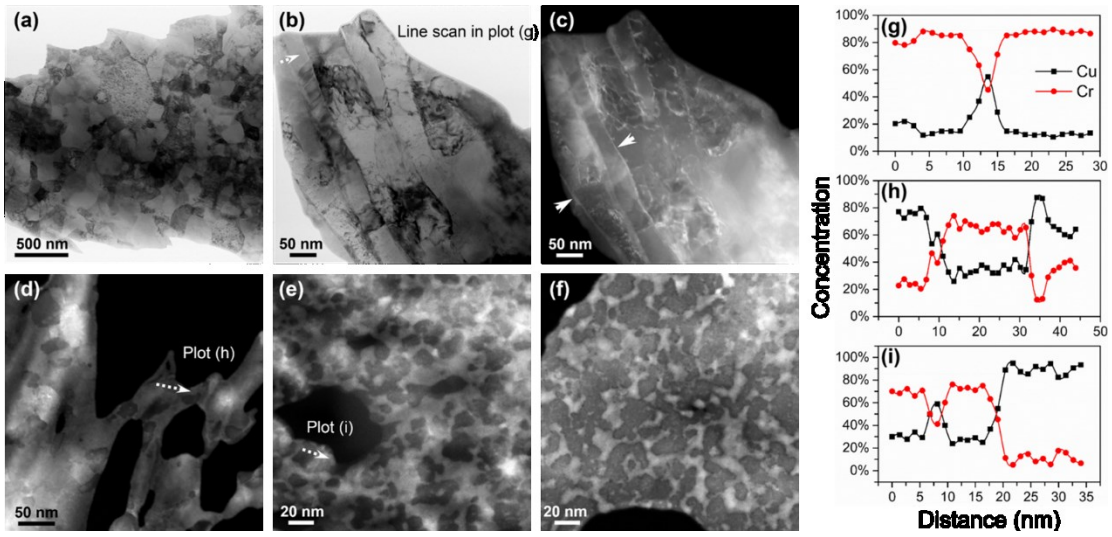

Fig. 3. (a) BF-STEM image of one Cu particle deformed with 1 rotation. (b, c) Corresponding BF-STEM and HAADF-STEM images of a Cr-rich region deformed with 5 rotations. (d) HAADF-STEM image of a Cu-rich region deformed with 5 rotations. (e, f) HAADF-STEM images of respective Cu-rich and Cr-rich regions deformed with 25 rotations. (g - i) EDXS line-scan profiles corresponding to positions marked by white dashed arrows in (b), (d) and (e).

In order to closely investigate the deformation behavior and intermixing of Cu-Cr alloys at the atomic scale, STEM and HRTEM techniques are employed. Figs. 3(a - f) show the corresponding bright-field (BF) and high angle annular dark field (HAADF) STEM images of Cu- and Cr-rich regions deformed with different numbers of rotations. As mentioned above, Cu phase is relatively easy to deform and the grains are drastically refined even the sample is only deformed by 0.25 rotation (ε = 3.4). Fig. 3a displays the BF-STEM image of one Cu particle deformed with 1 rotation, where it can be seen the Cu grains are refined to an average value of about 200 – 300 nm. Under this deformation condition, however, the Cr grains remain in micrometer sizes. The SEM image Fig. 1d shows that Cr particles start fragmentation under the deformation of 5 rotations. One Cr-rich region was closely checked and corresponding BF and HAADF-STEM images are shown in Figs. 3(b, c). EDXS measurement indicates that the whole tip is composed of about 90 at.% Cr and 10 at.% Cu. The Cr grains show lamellar structure orientated to the radial direction of HPT disk, with a thickness of about 30 – 100 nm. Furthermore, a large amount of dislocations are clearly visible in the Cr lamellae. Unexpectedly, in HAADF-STEM images there are a few of very thin layers with thickness of 1 – 2 nm and a brighter contrast present between two Cr lamellae, which are identified as Cu phases (labeled by arrows in Fig. 3c). It has been well documented that during severe plastic deformation the mechanism of forced intermixing is mainly built on the interface roughening and plasticity-driven mechanical mixing via shear transfer (dislocations, shear bands) across the heterophase interfaces, which is described as dislocation-shuffling [23,24]. Such shearing and interface roughening can create small embedded particles consisting of atoms from one phase into another. Our observation provides a direct evidence supporting this theory in HPT-deformed heterophase materials. The ample dislocations in both phases can facilitate the interface roughening which will cut off and eventually merge such thin Cu layers. Different from the Cr-rich areas, the Cu-rich regions show much finer grains for both Cu and Cr phases with equiaxed structures as shown in Fig. 3d. Some scattered Cr grains are embedded in the Cu matrix, and the grain sizes of Cu and Cr are mainly in the range of about 20 – 40 nm and 40 – 60 nm respectively.

When the Cu-Cr composite is deformed with 25 rotations (ε = 340), the microstructures become equiaxed and more homogeneous for both Cu and Cr phases, although Cu-rich and Cr-rich regions still exist with differences in phase volume as shown in Fig. 3e and Fig. 3f respectively. The average grain size at this strain condition is about 20 nm [9]. However, what's more interesting is the occurrence of less than 2 nm sized Cu clusters with bright contrast inside the Cr grains, in both Cu-rich and Cr-rich regions. These embedded Cu nanoclusters possess the same *bcc* structure as Cr phase based on HRTEM images of Cr grains.

Figs. 3(g - i) display the EDXS line-scan measurements on the corresponding positions marked with white dashed arrows in Figs. 3(b, d, e) respectively. The plots of Cu and Cr concentrations shown in Fig. 3g are recorded across two Cr lamellae with one 2 nm thick Cu thin layer embedded between Cr boundaries. With EDXS line-scan measurement, it is found that about 12 at.% Cu has been dissolved into the Cr matrix after deformation of 5 rotations. However, the measurement performed in the Cu-rich regions give a different result (Fig. 3h), where the line-scan crossing a Cr grain from Cu matrix as indicated in Fig. 3d. The left-hand side of EDXS plot corresponds to Cu-rich region, and about 23 at.% Cr is dissolved in the matrix. While inside the Cr grains, the average dissolved Cu is about 34 at.%, and one Cu cluster with size of 2 nm is found at the right-hand side within a Cr grain. The line-scan shown in Fig. 3i from the sample deformed with 25 rotations also reveals a 2 nm sized Cu cluster embedded in the Cr grain. The nanometer-scale EDXS measurements confirm the existence of Cu nano-clusters inside Cr grains, and show different dissolution process on the Cu-rich or Cr-

rich regions during deformation, which is different from the macro-scale observation using XRD or other techniques.

To further check the deformation behavior at the atomic scale, the sample deformed by 25 rotations was investigated by HRTEM. Fig. 4a displays a BF image of a Cr-rich region embedded in the matrix, with a composition of about 88 at.% Cr and 12 at.% Cu at the Cr-rich area. It can be seen that the grains in the matrix have been refined to about 20 nm, while the Cr phase still shows lamellar structure with thickness of 20 – 40 nm inside the large Cr particle. The HRTEM image shown in Fig. 4b is acquired on the two neighboring Cr subgrains marked by a white circle in Fig. 4a. The both two grains are close to $[001]_{bcc}$ zone axis. However, the lattices of these two grains are clearly subjected to a shear distortion along the interface. The Fast Fourier Transform (FFT) of the top grain shows that the angle between $(1\bar{1}0)$ and (110) planes is only 77.5˚ rather than 90˚ for standard cubic structures. Actually, we have observed previously the coexistence of two subareas with zone axes of $[001]_{bcc}$ and $[111]_{bcc}$ inside one Cr grain [9], which is due to the deformation-induced local transition from <001>-oriented *bcc* structure to <111>-oriented lattice. It is similar to the phase transition in *bcc* Mo caused by shear straining [25]. In addition, many dislocations locate at the interface of two subgrains. Fig. 4c shows an enlarged atomic structure of interface extracted from Fig. 4b, where one edge dislocation is visible. To clearly see this defect, a Fourier-filtered image using $(1\bar{1}0)$ reflection spot is exhibited as Fig. 4d. Due to the edge dislocation, $(1\bar{1}0)$ planes of two neighboring grains have a misfit angle of 3.5˚. The increasing accumulation of lattice dislocations at the interface of two subgrains forms the small angle grain boundary, giving rise to grain refinement [26].

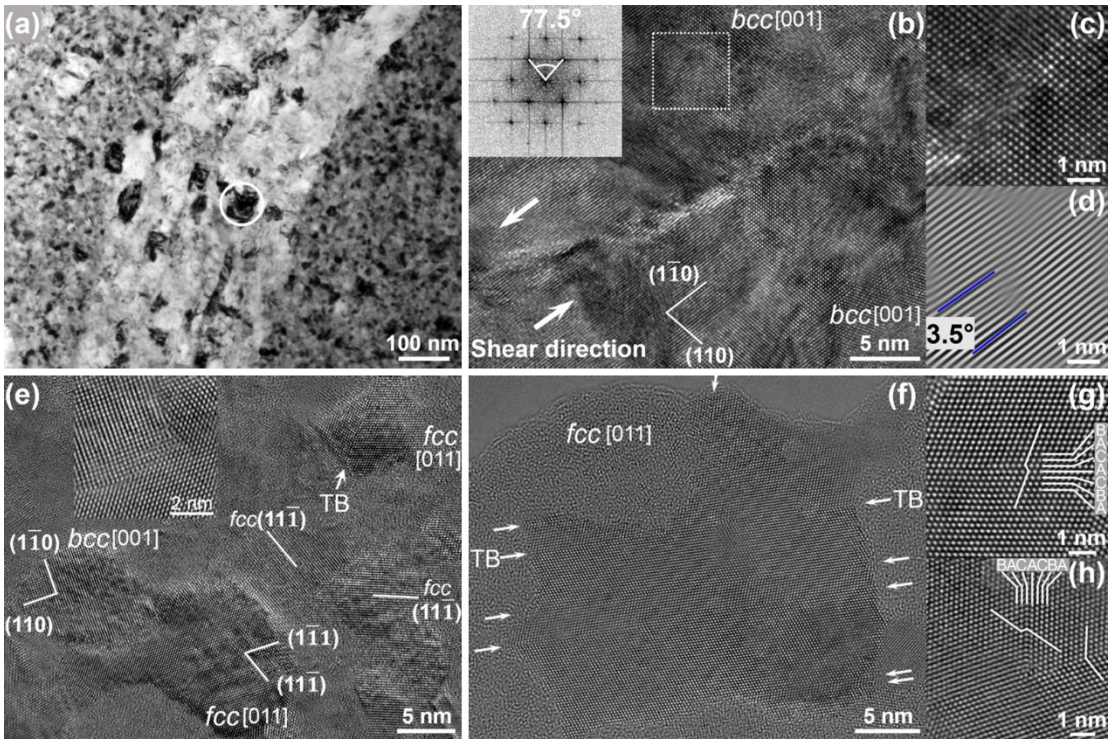

Fig. 4. Atomic structure characterizations of as-deformed sample with 25 rotations. (a) BF image of a Cr-rich region embedded in the matrix. (b) HRTEM image of two Cr grains from the position marked with a white circle in (a), and the FFT inset at the top-left corner is derived

from the area marked with a dashed box. (c, d) The HRTEM image extracted from the boundary and the corresponding Fourier-filtered image using $(1\bar{1}0)$ reflection spot. (e) Overall HRTEM image showing Cu and Cr grains, with highlighting an interface between Cu and Cr grains in the inset. (f) HRTEM displaying a Cu grain with many nanotwins, dislocations and stacking faults. Twin boundary is abbreviated as TB and indicated by white arrow in (e) and (f). (g, h) Two enlarged images showing the defects extracted from (f).

Fig. 4e shows an overall HRTEM image of Cu and Cr grains, highlighting an interface between Cu and Cr grains in inset. The two grains at the bottom left are one Cu grain with zone axis of $[011]_{fcc}$ and a Cr grain with zone axis of $[001]_{bcc}$, with an orientation relationship of $(1\bar{1}1)_{fcc}$ // $(110)_{bcc}$. Except for the twinned Cu grain with a zone axis of $[011]_{fcc}$ at the top right, there are a few other Cu grains which are not exactly on zone axes. Fig. 4f displays a clear HRTEM image of one Cu grain with many defects, i.e., nanotwins, dislocations and stacking faults. It can be seen that there are many nanotwins with thickness of several atomic layers. To observe these defects clearly, two enlarged images extracted from Fig. 4f are exhibited in Figs. 4(g, h). Fig. 4h displays a typical atomic structure of intrinsic stacking fault while Fig. 4h shows an intersection area of a stacking fault, an edge dislocation and a nanotwin. These atomic resolution observations exhibit an evidence of numerous defects present inside 20 nm-sized grains of HPT deformed alloys.

In summary, we systematically investigated the low-strain deformed ductile-brittle Cu-Cr alloys by high pressure torsion. The microstructural evolution, deformation behavior and dissolution process were recorded at the atomic scale. Our observation provides a direct evidence supporting the dislocation-shuffling mechanism in forced mixing of non-equilibrium system under severe plastic deformation. In addition, the solubility of both elements is strongly dependent on the Cu- or Cr-rich regions. In this Cu-Cr binary system, dimensions of less than 2 nm-sized Cu clusters were found inside the Cr grains, maintaining *bcc* structures. Furthermore, the atomic-scale distortion of Cr lattice induced by shear deformation has been detected directly, giving rise to formation of small angle grain boundary due to dislocation accumulation at the interface.

Acknowledgements

This work was financially supported by the Austrian Science Fund (FWF): No. P27034 - N20. The authors are highly grateful to Dr. Julian Rosalie at Erich Schmid Institute of Materials Science, Austrian Academy of Sciences for acquiring SEM images.

References

[1] R.Z. Valiev, R.K. Islamgaliev, I.V. Alexandrov, Prog. Mater. Sci. 45 (2000) 103–189.

[2] E. Ma, Alloys created between immiscible elements, Prog. Mater. Sci. 50 (2005) 413–509.

[3] X. Sauvage, P. Jessner, F. Vurpillot, R. Pippan, Scr. Mater. 58 (2008) 1125–1128.

[4] A. Bachmaier, G.B. Rathmayr, M. Bartosik, D. Apel, Z. Zhang, R. Pippan, Acta Mater. 69 (2014) 301–313.

[5] T.P. Harzer, S. Djaziri, R. Raghavan, G. Dehm, Acta Mater. 83 (2015) 318–332.

[6] T.P. Harzer, G. Dehm, Thin Solid Films 623 (2017) 48–58.

[7] C. Aguilar, V.P. Martinez, J.M. Palacios, S. Ordoñez, O. Pavez, Scr. Mater. 57 (2007) 213–216.

[8] J. Guo, J. Rosalie, R. Pippan, Z. Zhang, Scr. Mater. 133 (2017) 41–44.

[9] J. Guo, J.M. Rosalie, R. Pippan, Z. Zhang, Mater. Sci. Eng. A 695 (2017) 350–359.

[10] Z. Zhang, J. Guo, G. Dehm, R. Pippan, Acta Mater. 138 (2017) 42–51.

[11] A. Bachmaier, J. Schmauch, H. Aboulfadl, A. Verch, C. Motz, Acta Mater. 115 (2016) 333–346.

[12] J.M. Rosalie, J. Guo, R. Pippan, Z. Zhang, J. Mater. Sci. 52 (2017) 9872–9883.

[13] I. Sabirov, R. Pippan, Scr. Mater. 52 (2005) 1293–1298.

[14] A.K. De, D.C. Murdock, M.C. Mataya, J.G. Speer, D.K. Matlock, Scr. Mater. 50 (2004) 1445–1449.

[15] Y. Xu, S.H. Zhang, M. Cheng, H.W. Song, Scr. Mater. 67 (2012) 771–774.

[16] T.D. Shen, C.C. Koch, Acta Mater. 44 (1996) 753–761.

[17] E. Ma, M. Atzmon, F.E. Pinkerton, J. Appl. Phys. 74 (1993) 955–962.

[18] G.K. Williamson, W.H. Hall, Acta Metall. 1 (1953) 22–31.

[19] G.K. Williamson, R.E. Smallman, Philos. Mag. 1 (1956) 34–46.

[20] Y.H. Zhao, K. Lu, K. Zhang, Phys. Rev. B 66 (2002) 085404.

[21] Y.H. Zhao, X.Z. Liao, Z. Jin, R.Z. Valiev, Y.T. Zhu, Acta Mater. 52 (2004) 4589–4599.

[22] F.A. Mohamed, Acta Mater. 51 (2003) 4107–4119.

[23] D. Raabe, S. Ohsaki, K. Hono, Acta Mater. 57 (2009) 5254–5263.

[24] D. Raabe, P.P. Choi, Y. Li, A. Kostka, X. Sauvage, F. Lecouturier, K. Hono, R. Kirchheim, R. Pippan, D. Embury, MRS Bull. 35 (2010) 982–991.

[25] S.J. Wang, H. Wang, K. Du, W. Zhang, M.L. Sui, S.X. Mao, Nat. Commun. 5 (2014) 3433.

[26] D.A. Hughes, Q. Liu, D.C. Chrzan, N. Hansen, Acta Mater. 45 (1997) 105–112.

IV

In-situ atomic-scale observation of oxidation and decomposition processes in nanocrystalline alloys

Jinming Guo[1], Georg Haberfehlner[2], Julian Rosalie[1], Lei Li[3], María Jazmin Duarte[4], Gerhard Dehm[4], Gerald Kothleitner[2], Yunbin He[3], Reinhard Pippan[1], Zaoli Zhang[1]

[1] *Erich Schmid Institute of Materials Science, Austrian Academy of Sciences, Leoben 8700, Austria.*

[2] *Institute for Electron Microscopy and Nanoanalysis, Graz University of Technology, Steyrergasse 17, Graz 8010, Austria.*

[3] *Hubei Collaborative Innovation Center for Advanced Organic Chemical Materials, Ministry-of-Education Key Laboratory of Green Preparation and Application for Functional Materials, Hubei Key Lab of Ferro & Piezoelectric Materials and Devices, School of Materials Science and Engineering, Hubei University, Wuhan 430062, China.*

[4] *Max-Planck Institut für Eisenforschung GmbH, Max-Planck- Straße 1, Düsseldorf 40237, Germany.*

Oxygen contamination is a problem which inevitably occurs during severe plastic deformation of metallic powders by exposure to air. Although this contamination can change the morphology and properties of the consolidated materials, there is a lack of detailed information about the behavior of oxygen in nanocrystalline alloys. In this study, aberration-corrected high-resolution transmission electron microscopy and associated techniques are used to investigate the behavior of oxygen during *in-situ* heating of highly-strained Cu-Fe alloys. Contrary to expectations, oxide formation occurs prior to the decomposition of the metastable Cu-Fe solid solution. This oxide formation commences at relatively low temperatures, generating nano-sized clusters of firstly CuO and later Fe_2O_3. The orientation relationship between these clusters and the matrix differs from that observed in conventional steels. These findings provide a direct observation of oxide formation in single-phase Cu-Fe composites and offer a pathway for the design of nanocrystalline materials strengthened by oxide dispersions.

Introduction

Nanostructuring and alloying are strategies to obtain enhanced properties for bulk metals[1–5]. Severe plastic deformation (SPD) can effectively generate novel metallic nanocrystalline materials by drastically refining and mechanically alloying normally immiscible composites[6–10]. Now combined with powders processing technique, SPD is extended to produce nanocrystalline alloys with desirable compositions directly from blended powders without any precasting[11], which is a convenient low-cost route in manufacturing applicable bulk materials.

However, gaseous impurities in the raw materials and introduced during SPD generation in the nanostructures pose a challenge which needs to be addressed prior to industrial application as they will influence material properties[12,13]. Oxygen contamination seems to be inevitable during premixing and consolidation for powders processing, as well as in the sequential straining of deformation[14,15]. Moreover, it indeed has been realized that oxygen could be incorporated into the nanocrystalline samples during processing, generating discrepant morphologies[13], mechanical properties[12,15] and thermal stabilities[13]. However, to our knowledge, the exact status of such contaminant inside the materials remains unclear, and how it behaves during annealing has never been studied.

For decades, it was believed that pure metal precipitates of already dissolved elements will form inside grains or at grain boundaries after annealing, and some reports indeed supported this by observing nano-sized precipitates of alleged pure metal elements[16]. However, some different types of carbides were detected inside annealed bulk samples, pointing out that contaminants could affect constituents of precipitates and then induce discrepant properties of nanostructured alloys[17]. Nevertheless, the formation processes of heterogeneous precipitates in nanocrystalline alloys were never investigated directly due to the tiny signal intensities of trace amount of such light elements, which are barely detectable by conventional techniques. The current empirical explanations on the effects of light elements are based on phenomenological assumptions[15,18].

It is known that oxides are efficient additives to produce so-called oxides-dispersion-strengthened steels/refractory metals which have been strenuously developed for decades due to their high temperature strength, stability and enhanced ductility[19–29]. Therefore, it is reasonable to assume that the potential existence of oxide clusters may affect the properties and microstructures in nanocrystalline materials. Fortunately, the advent of modern *in-situ* high-resolution transmission electron microscopy (HRTEM), combined with image processing technique, enables probing the mechanism behind complicated physicochemical processes at the atomic scale. For example, nowadays novel phase formation[30,31] and transition[32,33], metal-catalyzed process[34], deformation twinning generation[35], irradiation-induced void formation[36] as well as nanocrystal facet development[37] have been captured in *real-time* observations.

Stimulated by direct atomic-resolution observation, we systematically studied the thermal behaviors of oxygen in high pressure torsion (HPT) deformed Cu-Fe alloys by means of *in-situ* spherical-aberration corrected HRTEM using a heating holder, via recording atomic-resolved images, diffraction patterns as well as capturing compositional information by electron energy-loss spectroscopy (EELS) and energy dispersive X-ray spectroscopy (EDXS), supplemented by X-ray photoelectron spectroscopy (XPS), synchrotron X-ray diffraction (XRD), atom probe tomography (APT) and density-functional theory (DFT) calculations. The results show that the 75 at.%Cu - 25 at.%Fe (75Cu-25Fe) alloy has a single face-centered-cubic (*fcc*) structure at room temperature after severe deformation. When heated, unexpected oxidation processes forming CuO and Fe_2O_3 inside grains are detected at relatively low temperature before the *fcc*

supersaturated solid solution decomposes into Fe- and Cu-rich grains. Lattice coherency between oxides and matrix is determined based on different HRTEM images. This work provides, to our knowledge, the first observation of oxygen behavior in nanocrystalline alloys and demonstrates that stable nano-sized oxides can easily form inside grains, which may pose a promising route to manipulate mechanical properties by intentionally incorporating light elements before deformation and also assist in quantitatively investigating on the role of oxygen in the grain refinement and intermixing of nanocrystalline alloys.

Results

Detection of oxidation and decomposition processes. The blended powders of 75Cu-25Fe are severely deformed forming a single *fcc* structure after 100 rotations of high pressure torsion (equivalent strain of 1360 at the investigated areas). The grains are drastically refined from roughly 50 μm down to an average size of 58 nm according to large population statistics (Supplementary Figure 1 and Note 1). The presence of oxygen in as-deformed bulk samples is verified by XPS measurements and the oxygen concentration is about 3.5 at.% (Supplementary Figure 2, Note 2 and Table 1). The sources of oxygen contamination can be from native oxide layers of the micron-sized particles of raw powders which are usually introduced during powders premixing in air, and residual air voids after the compaction of mixed powders which are trapped inside samples. To reveal the latent oxygen behavior inside HPT nanocrystalline alloys, *in-situ* TEM is employed to observe the subsequent phenomena under annealing. To minimize the possible interference of the surface adsorbed oxygen on the TEM samples, TEM samples are transferred to the microscope immediately after ion-milling. Fig. 1 shows low magnification TEM images and diffraction information as well as bright-field (BF) and dark-field (DF) images of the *in-situ* heated sample. Fig. 1a displays a series of images from the same area recorded at different temperatures. Almost no grain coarsening is observed even when heated up to 420 °C, and careful investigation with scanning transmission electron microscopy (STEM) confirms the thermal stability of microstructures (Supplementary Figure 3 and Note 3), which has been reported in the literature and attributed to alloying of elements and the pinning effect of contaminants in nanocrystalline metals[38]. The distribution of dark areas in the BF images (Fig. 1a) indicates, that the grain orientations remain unchanged during *in-situ* heating, which makes it feasible to record and compare HRTEM images focusing on a small area (marked as white circle in the first panel of Fig. 1a). The integrated profiles of diffraction patterns of the same area using PASAD[39] are shown in Fig. 1b. All peaks in the profiles are indexed as planes of *fcc* matrix, Fe precipitates or oxides based on the interplanar spacing. It is worth noting that on the left side of $(111)_{fcc}$ peak, i.e., the larger interplanar spacing values than $(111)_{fcc}$, some tiny peaks corresponding to oxides which are marked as $(101)_{CuO}$, $(112)_{Fe2O3}$ and $(110)_{CuO}$ appear when the temperature reaches 260 °C. At an even higher temperature of 340 °C additionally $(200)_{Fe}$ and $(211)_{Fe}$ peaks from Fe can also be clearly observed. Selected area electron diffraction gives structural information of a micron-sized area of the TEM sample, and has higher scattering efficiency than XRD. It is therefore more sensitive to an intensity difference compared to XRD. But it is still relatively insensitive to reflect the onset of oxidation and precipitation at the atomic scale, so the way is to take the advantage of HRTEM (as shown in the following section).

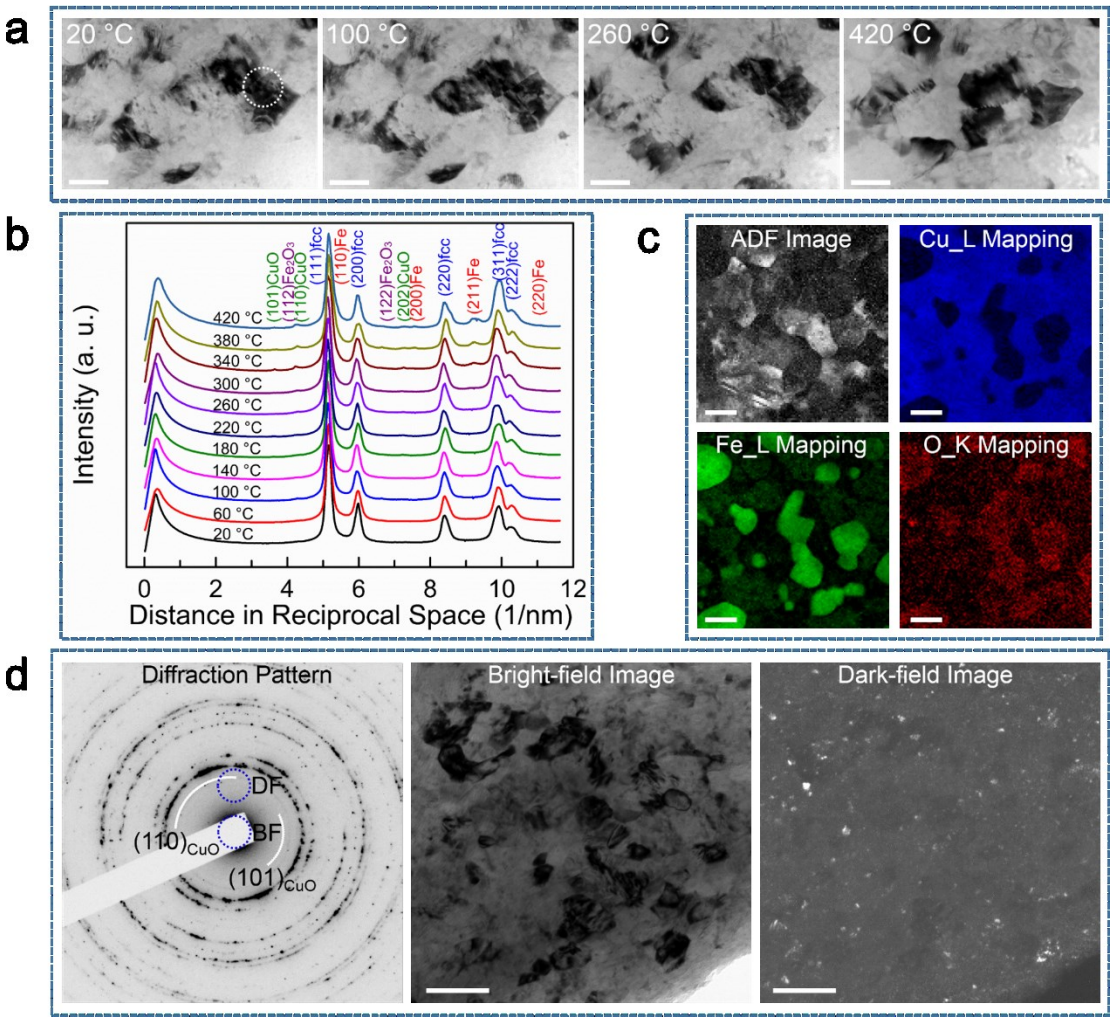

Fig. 1 TEM images and diffraction patterns for *in-situ* heated samples. (**a**) Low magnification images focusing on the same area recorded at different temperatures. (**b**) Integrated profiles of diffraction patterns of the same area. (**c**) ADF image and corresponding elemental distributions using EELS mapping of Cu_$L_{2,3}$, Fe_$L_{2,3}$ and O_K edges for the sample after *in-situ* annealing at 420 °C. (**d**) Diffraction pattern of the sample *in-situ* annealed at 420 °C, the corresponding BF and DF images forming from partial diffractions as schematically illustrated in the left diffraction pattern with blue circles. The scale bars in (**a**,**c**) are 50 nm and in (**d**) is 100 nm.

Fig. 1c shows the annular dark field (ADF) image and corresponding elemental distributions from electron energy loss spectroscopy (EELS) mapping of the Cu_$L_{2,3}$, Fe_$L_{2,3}$ and O_K edges for the sample after *in-situ* annealing at 420 °C. The colorful area in each image represents the respective elemental distribution. It can be seen that Fe precipitates are embedded inside the Cu matrix with a size ranging from about 5 nm to 60 nm. O is distributed over the whole area but enriches at Fe-rich particles. Fig. 1d displays a diffraction pattern of the sample *in-situ* annealed at 420 °C and corresponding BF and DF images. The smallest objective aperture is positioned at the locations indicated in the diffraction pattern with blue

circles to form BF and DF images. For the DF image only oxide diffraction spots are captured by objective aperture, so in this way the dispersively distributed bright features in DF image correspond exactly to oxides. Although it is impossible to distinguish between CuO and Fe_2O_3 due to the unavailability of sufficiently small objective aperture, this oxides mapping verifies that the oxygen exists everywhere inside HPT samples which is consistent with the EELS O_K edge mapping, and simultaneously it shows that oxides form with extremely fine dimensions of roughly less than 15 nm[19,20].

Atomic-scale distribution of oxides and Fe precipitates. To observe the formation processes of oxides at the atomic scale, *in-situ* HRTEM is employed. Fig. 2 displays a series of HRTEM images recorded during *in-situ* heating and the corresponding distribution mappings of oxides and Fe precipitates. The first column shows the sequential *in-situ* HRTEM images recorded during heating. It can be seen intuitively that as the temperature increases, some areas appear blurred and their lattice orientations change compared to the *fcc* matrix. The HRTEM image recorded at 380 °C is enlarged and inserted at the top-right corner to better distinguish the different structures. The second column shows FFT calculations of the corresponding HRTEM images recorded at different temperatures. The FFT results show that the *fcc* matrix is on $[011]_{fcc}$ zone axis. For the as-deformed sample prior to heating, the FFT is quite "clean" with only diffraction spots of the *fcc* matrix along the [011] zone axis. When the sample is heated at 60 °C, several tiny spots (red color) appear which are indexed as reflections of CuO according to the calculations of interplanar spacing. Then after annealing at 100 °C, more diffraction spots appear close to the central spot equivalent to larger spacing, which are indexed as planes of Fe_2O_3 phase. CuO shows a monoclinic structure with lattice parameters of a = 4.684 Å, b = 3.423 Å, c = 5.129 Å and β = 99.54°[40], while Fe_2O_3 can be recognized having a hexagonal structure with lattice parameters of a = 5.035 Å, b = 5.035 Å, c = 13.752 Å and γ = 120°[41,42]. So the phases of CuO and Fe_2O_3 can be easily distinguished by the interplanar spacing of low-index planes, such as (002), (101) and so on. When the temperature reaches 260 °C, the FFT becomes more complicated with more subtle spots appearing. By carefully comparing the FFT with previous ones, pure Fe precipitates can be identified by their (110) diffraction spots. One should note that, although $(022)_{Fe2O3}$ (2.078 Å), $(012)_{CuO}$ (2.034 Å) and $(110)_{Fe}$ (2.037 Å) have similar interplanar spacings, for FFT images obtained at 180 °C and 220 °C, at the circle with a radius of 9.8208 ± 0.4910 1/nm (5% variation) corresponding to interplanar spacing of 2.037 ± 0.102 Å, no clear spots can be detected while other spots from CuO and Fe_2O_3 phases can be easily recognized. But for the FFT image of the 260 °C-annealed sample, at this circle region, some discernable spots with detectable intensities show up. So these spots can be justified as the evidence of Fe precipitates. The partial reflections of CuO, Fe_2O_3 and Fe (marked as colorized disks) in the FFT images are selected to generate their distribution mappings by Inverse Fast Fourier Transform (IFFT) with specific conditions of the same circle size, circle numbers and positions for each phase[32]. The resultant distributions of CuO, Fe_2O_3 and Fe precipitates are displayed in the third to fifth columns respectively, with the same contrast limits for all images in one column. Generally, the areas of the CuO, Fe_2O_3 and Fe precipitates increase with the annealing temperature, and finally the dimensions of the oxides are in the range of 10 nm, well consistent with the result of oxide distributions in DF images shown in Fig. 1d. We note that the spatial distribution of CuO is almost identical to that of Fe_2O_3, which means that oxygen diffuses to one specific area during heating, simultaneously triggering the nucleation processes of oxides. From the mapping of Fe precipitates, only tiny areas are marked as Fe agglomerates because of the limited image size.

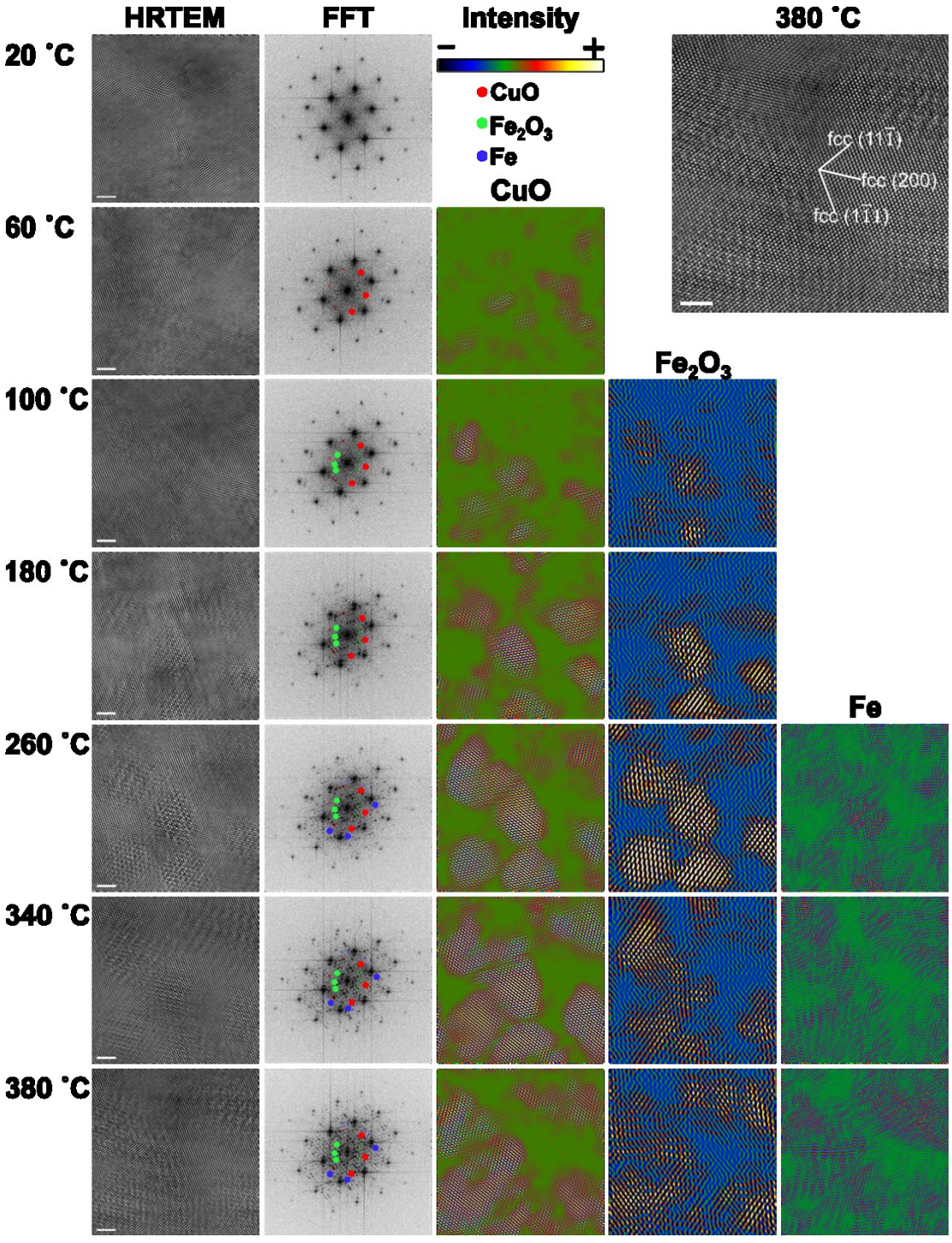

Fig. 2 HRTEM images and corresponding distributions of oxides and Fe precipitates for *in-situ* heated samples. The first column shows the HRTEM images recorded during *in-situ* sample heating. The second column shows the FFT calculations of the corresponding HRTEM images recorded at different temperatures. The third to fifth columns display the distributions of oxides and Fe precipitates by IFFT. The HRTEM image recorded at 380 °C is enlarged and inserted at the top-right corner. The scale bars in HRTEM images are 2 nm.

Additionally, one may query whether the electron beam affects the formation of oxides and precipitates. Actually electron beam effects are unavoidable in TEM studies and should be taken into consideration, especially in *in-situ* experiments[43]. During our experiments, two measures have been taken to minimize the potential influences of the electron beam. First, during image recording, the electron beam was spread to fit the size of the fluorescent screen every time. The beam was switched off during the heating process and the imaging was done immediately after the heating was finished. Second, to confirm that oxidation and precipitation are not caused by e-beam irradiation, a series of comparison experiments were carried out, where a region of the sample was exposed to the electron beam continuously with the same dose as in the *in-situ* experiments (Supplementary Figure 4 and Note 4). The result shows that even after exposure for several minutes, no obvious changes were observed. In addition, the electron dose rate of the HRTEM images in the *in-situ* heating experiments are quantified as shown in Supplementary Figure 5 and Note 5. Even though electron beam effects are complex, our systematic experiments have confirmed that in the present study electron beam effects on the oxidation and precipitation processes are negligible.

Oxides and Fe precipitates in *ex-situ* annealed bulk samples. To investigate whether the TEM sample geometry has an effect on the reactions or processes due to its reduced size, as-deformed bulk materials were *ex-situ* annealed with the same time as *in-situ* heating in above HRTEM investigations. XRD, EDXS, APT and TEM characterizations of *ex-situ* annealed samples are shown in Fig. 3. Fig. 3a shows the full range XRD scan of 40˚ – 100˚ of as-deformed and annealed samples. It shows clearly that the body-centered-cubic (*bcc*) Fe phase starts to appear when the sample is annealed at 260 °C. Fig. 3b displays the finely scanned XRD profiles with a range of 40˚ – 47˚ to closely show the appearing process of $(110)_{Fe}$. It can be observed clearly that, at the position corresponding to $(110)_{Fe}$, a weak peak shows up, which becomes stronger with increasing temperature. Simultaneously, the $(111)_{Cu}$ peak obviously shifts to higher angles as a result of temperature increase above 100 °C. The calculated lattice parameters of the *fcc* phase, and the averaged residual Fe concentrations in the *fcc* matrix of samples annealed at different temperatures are presented in Fig. 3c. The lattice parameter of sample annealed at 100 °C keeps identical to that of as-deformed sample, but it then decreases when annealed at 260 °C, and finally it is reduced by 0.017 Å compared to the original value due to the decomposition of super saturated solid solutions after annealing at 420 ˚C. Based on the two aspects of $(110)_{Fe}$ appearance and $(111)_{Cu}$ peak shift, it can be concluded that the dissolved Fe starts to segregate at the temperature of 260 °C, which is in accordance to *in-situ* heating results. The residual Fe concentration in the *fcc* matrix is systematically measured at different annealing temperatures using the high spatially-resolved EDXS, and the result directly confirms the segregation of Fe from the matrix.

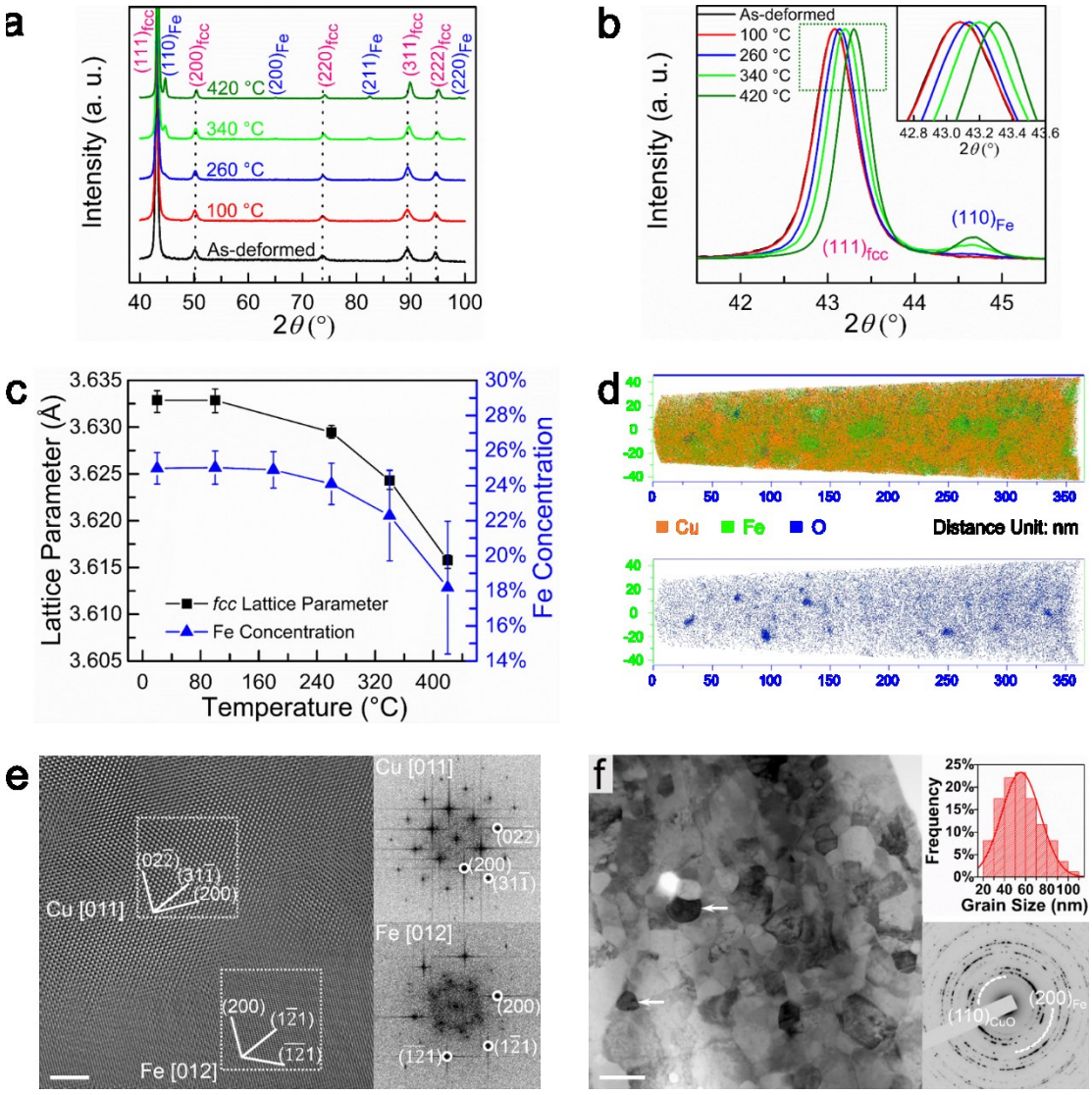

Fig. 3 XRD, EDXS, APT and TEM characterizations of *ex-situ* annealed samples. (**a**) Full range XRD profiles of 75Cu-25Fe samples *ex-situ* annealed at different temperatures. (**b**) Fine scanning XRD profiles focusing on $(111)_{fcc}$ and $(110)_{Fe}$ peaks. (**c**) Lattice parameter and residual Fe concentration in *fcc* matrix of samples annealed at different temperatures. (**d**) APT overview image of the 75Cu-25Fe sample *ex-situ* annealed at 300 °C and the corresponding oxygen map highlighting O-rich clusters. (**e**) HRTEM image of the sample *ex-situ* annealed at 420 °C showing the neighboring Cu and Fe grains on zone axes of $[011]_{Cu}$ and $[012]_{Fe}$ respectively. The two FFT images are calculated based on the Cu and Fe areas marked with white frames. (**f**) Low magnification BF image of the sample *ex-situ* annealed at 420 °C; the white arrows indicate Fe grains. The inset at top-right corner is a grain size statistics histogram, and the bottom-right diffraction pattern is from the same annealed sample. The scale bar in (**e**) is 2 nm and in (**f**) is 100 nm.

Furthermore, APT was employed to detect the oxide clusters for the *ex-situ* annealed sample at 300 °C as shown in Fig. 3d. From the upper overview image, some Fe-rich areas (green color), containing 8.3 at. % of Cu and 0.35 at.% oxygen atoms are observed with dimensions of 20 – 50 nm which accords with the results obtained from EELS mapping displayed in Fig. 1c. The Fe content in the matrix is about 23.3 at.% in agreement also with the EDXS result shown in Fig. 3c. The bottom image shows the oxygen distribution, from which it can be seen that O atoms distribute almost homogeneously while some clusters with sizes of 3 – 8 nm form after *ex-situ* annealing, mainly at the boundaries between Fe-rich grains and the matrix. Fig. 3e displays a HRTEM image of the sample *ex-situ* annealed at 420 °C showing neighboring Cu and Fe grains with zone axes of $[011]_{Cu}$ and $[012]_{Fe}$ respectively. The two FFT images are calculated based on the Cu and Fe areas marked by white frames. Evidently, the neighboring Cu and Fe grains have an orientation relationship of $(02\overline{2})_{Cu}$ // $(200)_{Fe}$, which is different from the typical K-S relationship relevant to *fcc* and *bcc* structure interface, i.e., $(111)_{fcc}$ // $(110)_{bcc}$[44]. A low magnification BF image of the same sample *ex-situ* annealed at 420 °C is shown in Fig. 3f. The inset at the top-right corner shows the grain size statistics, and the diffraction pattern at the bottom right is recorded on the same annealed sample where $(110)_{CuO}$ and $(200)_{Fe}$ rings are marked. The average grain size is about 56 nm, and the emergence of $(110)_{CuO}$ diffraction ring confirms the occurrence of oxides inside HPT-deformed samples during annealing. The white arrows in Fig. 3f indicate Fe grains formed after annealing at 420 °C, consistent with the appearance of the $(200)_{Fe}$ diffraction ring.

To confirm the conclusions drawn from the *in-situ* heating experiments, EELS mappings are implemented on the *ex-situ* annealed sample at 420 °C. The morphology and distribution of Fe grains are almost identical to those from *in-situ* annealing, with dimensions of about 20 – 50 nm (Supplementary Figure 6 and Note 6). Meanwhile, synchrotron XRD measurements presented in Supplementary Figure 7 and Note 7 confirm the presence of oxides inside the materials after annealing.

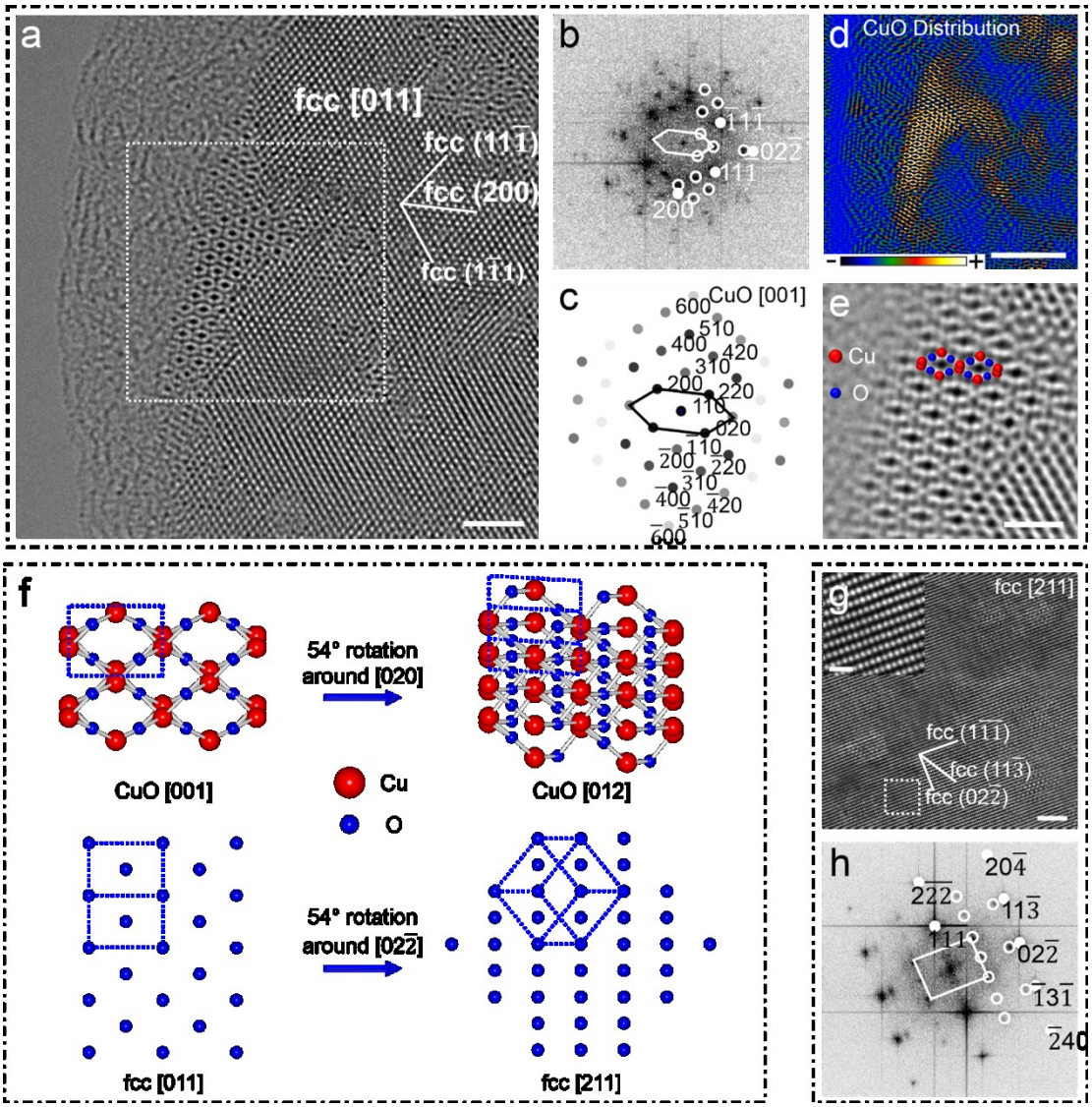

Fig. 4 Lattice matching relationship between CuO and *fcc* matrix. (**a**) HRTEM image of CuO developed from *fcc* matrix with $[011]_{fcc}$ zone axis. (**b**) FFT image calculated from the white frame area in (**a**). (**c**) Simulated diffraction pattern of CuO on zone axis of $[001]_{CuO}$. (**d**) CuO distribution generated from the CuO reflections marked with white circles in (**b**). (**e**) Enlarged filtered CuO HRTEM image. (**f**) Schematic illustration of lattice matching relationship between CuO and *fcc* matrix. (**g**) HRTEM of *fcc* matrix on zone axis of $[211]_{fcc}$. The inset is an enlarged area of *fcc* matrix. (**h**) FFT reflections of image (**g**). Scale bar: (**a**) 2 nm, (**e**) 1 nm, (**g**) 2 nm and the inset in (**g**) 0.5 nm.

Lattice matching relationship between CuO and *fcc* matrix. Fig. 4a shows a HRTEM image of CuO developing within the *fcc* matrix after annealing at 420 °C. The *fcc* matrix shows a lattice structure with a $[011]_{fcc}$ zone axis, while CuO is exactly on the $[001]_{CuO}$ zone axis. The FFT calculated from the area within the white frame in Fig. 4a and simulated diffraction pattern of CuO on $[001]_{CuO}$ zone axis are displayed in Fig. 4b and Fig. 4c respectively. The main reflection spots of *fcc* matrix on zone axis $[011]_{fcc}$ are marked with solid discs, while the diffraction spots of CuO are marked by white circles, which match well with the simulated diffraction pattern. In the FFT image, it can be clearly seen that the matching relationship between CuO and the *fcc* matrix is $(\bar{4}00)_{CuO}$ // $(200)_{fcc}$ and $(020)_{CuO}$ // $(02\bar{2})_{fcc}$, with a corresponding lattice mismatch of 6.2% and 10.4% in each direction. Fig. 4d shows the IFFT image using only CuO reflections marked in Fig. 4b with white circles highlighting the CuO clusters from *fcc* matrix as visible in Fig. 4a. To clearly show the CuO lattice structure, an enlarged Wiener-filtered image of CuO is displayed in Fig. 4e, where the Cu and O atoms are identified.

From $[011]_{fcc}$ zone axis of *fcc* matrix, the matching relationship between CuO and *fcc* matrix is defined as above-mentioned. Based on crystallography, a 54˚ rotation of the *fcc* matrix around the $[02\bar{2}]$ crystallographic orientation to the $[211]_{fcc}$ zone axis, is accompanied by a 54˚ rotation of CuO around the [020] direction to the $[012]_{CuO}$ zone axis, as shown in Fig. 4f. Fig. 4g shows a HRTEM image on a zone axis of $[211]_{fcc}$ with an inset of enlarged lattice structure at the top-left corner. Fig. 4h presents the FFT of the whole image shown in Fig. 4g, with the main reflection spots of the *fcc* matrix on the $[211]_{fcc}$ zone axis marked with white solid discs, and weak spots of CuO on $[012]_{CuO}$ zone axis sorted out by white circles. The matching relationship between CuO and the *fcc* matrix is accurately defined from two crystallography directions. The full lattice coherency between the oxide nanoclusters and the matrix gives rise to a low interface energy between the two disparate phases, oxide and metal. The low interface energy can effectively prevent the coarsening of the oxide precipitates[19].

Discussion

Fig. 5 shows a schematic diagram of oxidation process at the atomic scale. After severe deformation of the 75Cu-25Fe alloy, the oxygen atoms distribute randomly at the centers of octahedra as interstitials in the *fcc* lattice as shown in Fig. 5a[45–48]. The oxygen atoms are activated by heating and diffuse in the *fcc* lattice. The schematic diagram of the activation and diffusion processes of O atoms is shown in Fig. 5b, where the configurations of the initial state, transition state and final state are displayed in the left, middle and right panels respectively. A number of calculations have reported the energy state of light elements diffusion from one octahedral center to another, giving different activation energy values[45–48]. The activated oxygen atoms then diffuse through the *fcc* lattice, forming O-rich nanoclusters[47,48] as shown in Fig. 5c. Because of the existence of ample point defects, such as vacancies, solute atoms and O interstitials in severely deformed alloys, the formation energy of O-rich nanoclusters is largely decreased due to the bound state of O-Vacancy pairs with high stability[47]. The binding energy of O with one nearest-neighbor Fe vacancy is about -1.45 eV[47,48]. At the next stage, oxides nucleate when the external heating energy is imposed on the O-rich area. According to the experimental results, the nucleation of oxides starts at 60 °C when the sample is heated for 10 min. Based on the DFT and DFT + U model[49,50], the formation enthalpies of copper and iron oxides are carefully calculated. The calculation procedures and results are displayed in Supplementary Information (Supplementary Note 8 and Table 2). The calculated formation

enthalpies are comparable to the values given in many previous reports[51]. It shows that the formation enthalpies of CuO and Fe_2O_3 are lower than those of their counterparts, Cu_2O and FeO, respectively. Thus, from the viewpoint of the formation enthalpy, the formation of CuO and Fe_2O_3 rather than other oxides with different valences may be explained. The reason why CuO was observed prior to Fe_2O_3 is most likely ascribed to the large volume of Cu in the alloy. The finally formed CuO lattice along $[001]_{CuO}$ embedded in the *fcc* matrix with zone axis of $[011]_{fcc}$ is illustrated in the schematic diagram in Fig. 5d. Nevertheless, it should be emphasized that although nano-sized oxide clusters are detected inside grains during heating, the possibility that oxides precipitate at grain boundaries and TEM foil surfaces cannot be excluded.

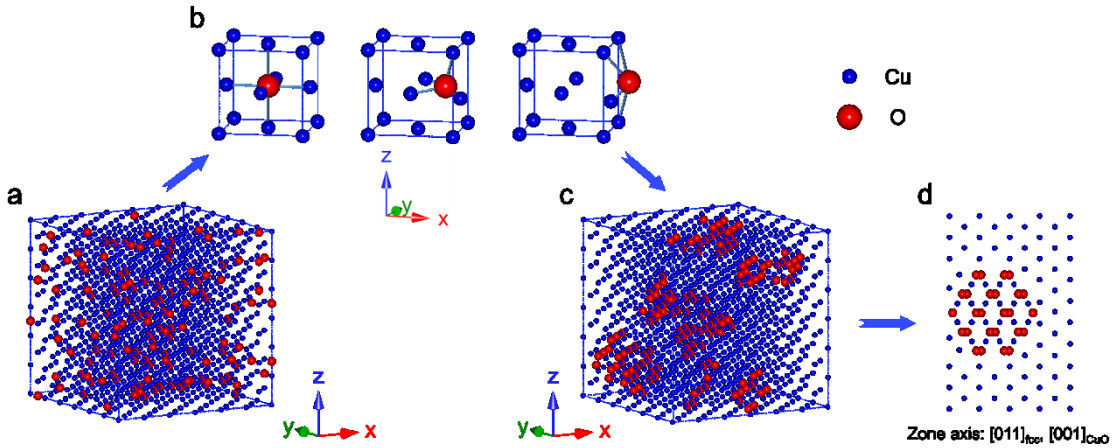

Fig. 5 Schematic diagram of the oxidation process. (**a**) As-deformed state with oxygen randomly distributed in *fcc* matrix. (**b**) Oxygen movement from one octahedral center to another. (**c**) O-rich nanoclusters formation inside the *fcc* matrix. (**d**) Formed CuO with zone axis of $[001]_{CuO}$ embedded inside *fcc* matrix with zone axis of $[011]_{fcc}$.

In summary, our work demonstrates atomic-scale observations of oxidation and decomposition processes in severely deformed *fcc* Cu-based nanocrystalline alloys using *in-situ* HRTEM. Randomly distributed, stable oxide clusters with dimensions of several nanometers are captured in nanocrystalline samples. Our findings show the critical consequences of oxygen presence in nanocrystalline alloys, and may offer a pathway to strengthen the mechanical properties via intentionally forming oxides-dispersed nanocrystalline materials.

Methods

Sample deformation by high pressure torsion. The commercial coarse-grained powders from Alfa Aesar (Karlsruhe, Germany) of Cu (Purity 99.9%) and Fe (Purity 99.9%) were fully mixed with composition of 75 at.%Cu - 25 at.%Fe and then HPT deformed using a two-stage method[11] with 100 rotations at room temperature and air cooling for the whole process. The pressure during HPT was fixed at 7.3 GPa and the rotation speed was 0.4 r/min.

***In-situ* heating in transmission electron microscope.** *In-situ* heating experiments were conducted in TEM and STEM to characterize in detail the microstructures and compositions of the HPT deformed Cu-Fe alloy. The TEM sample was *in-situ* annealed for 10 min at different temperatures using Gatan heating holder, in steps of 40 °C from room temperature to a maximum temperature of 420 °C. All microstructural investigations in this work were undertaken at radius of 3.0 mm from the torsional axis of the HPT deformed disks. (S)TEM studies were carried out using a field emission gun transmission electron microscope (JEOL JEM-2100F, Japan) equipped with an imaging spherical aberration corrector. In STEM mode, a spot size of 0.7 nm of electron beam was used to record high angle annular dark field (HAADF) images. Simultaneous EDXS for nanoscale compositional analysis was also carried out in STEM mode. STEM EELS investigations were done on a probe-corrected FEI Titan³ 60-300 microscope operated at 300 kV equipped with a Gatan GIF Quantum energy filter. The electron beam was perpendicular to the shear plane of the disks for all microstructural investigations in this work.

X-ray diffraction characterization. X-ray diffraction was conducted on all samples using a Smartlab X-Ray Diffractometer (Rigaku, Japan) with Cu $K_{\alpha 1}$ radiation ($\lambda = 1.540593$ Å). Here it should be emphasized that the X-ray beam width for all the measurements in this work was limited to 2 mm using the relevant incident slit, covering a large area of HPT deformed disk from the radius of 2 mm to 4 mm. For the whole range scanning of 40˚ – 100˚, the scanning speed is 0.4 ˚/min with a step of 0.02˚, and then an extremely fine scanning speed of 0.1 ˚/min with the step of 0.02˚ was imposed for the focused range of 40˚ – 47˚ to get better signal to noise ratio and more accurate diffraction angles.

Atom probe tomography characterization. APT measurements were conducted in a local electrode atom probe, LEAP 3000X HR™ from Cameca Instruments. The measurements were set up in laser mode with energy of 0.8 nJ and a pulse repetition rate of 250 kHz, base temperature of 60 K and a detection rate of 0.005 atoms per pulse. The specimens were prepared by standard sample lift out and annular milling, using a focused ion beam (FIB) FEI Helios 600i Dual Beam workstation. A final cleaning of the tip with low ion energy of 3 kV ensured a Ga content in the analyzed volumes below 0.05 at.%.

X-ray photoelectron spectroscopy, synchrotron X-ray diffraction methods and density-functional theory calculation procedures are presented in detail in Supplementary Information (Supplementary Note 2, Note 7 and Note 8).

Acknowledgements

We gratefully acknowledge the financial support by the Austrian Science Fund (FWF): No. P27034 - N20. Peter Kutleša, Gabriele Felber, Herwig Felber and Silke Modritsch at the Erich Schmid Institute of Materials Sciences, Austrian Academy of Sciences, are gratefully acknowledged for their help with the HPT, TEM and metallographic samples preparation. G. H. and G. K. acknowledge funding from the European Union within the 7th Framework Program [FP7/2007-2013] under Grant Agreement No. 312483 (ESTEEM2). Y. H. acknowledges the National Natural Science Foundation of China (Grant Nos. 61274010, 51572073, 11774082). The authors are highly grateful to Yong Zhang at Hunan University, China and Erich Schmid Institute of Materials Sciences, Austrian Academy of Sciences for his kind help in the DFT calculations.

Author contributions

Z. Z. conceived the idea and oversaw the whole project. J. G. conducted the experiments and wrote the manuscript with input from all authors. G. H. and G. K. conducted STEM EELS mapping experiments. J. R. assisted the XRD experiments, and L. L., Y. H. performed XPS measurements. M.J. D. and G. D. carried out the APT characterization. J. G. and Z. Z. analyzed the experimental results. R. P. made helpful comments on the manuscript. All authors read through the manuscript and contributed to the discussion of the results.

Supplementary Information

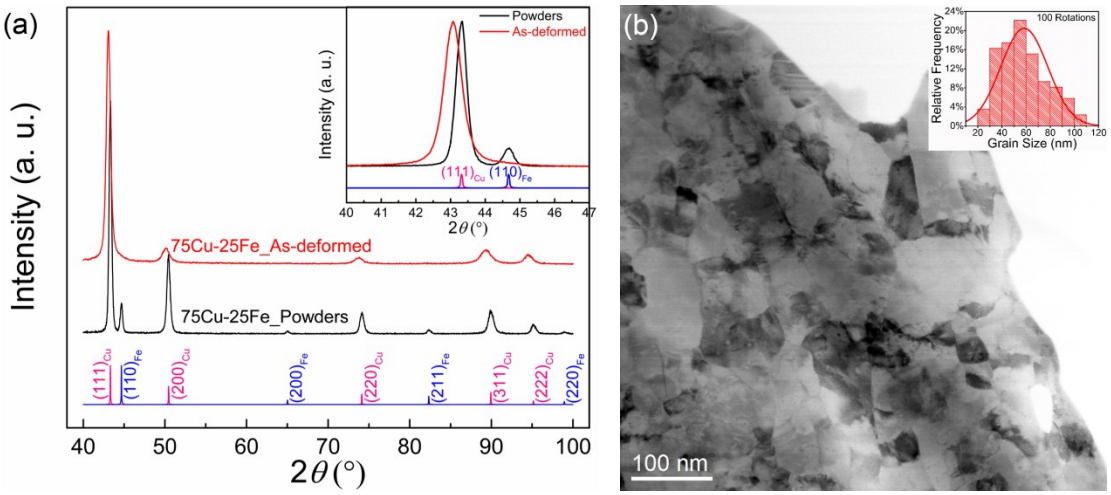

Supplementary Figure 1: (**a**) XRD comparison between compacted powders and HPT-deformed sample of 75Cu-25Fe with 100 rotations. The enlarged profiles focusing on $(111)_{Cu}$ and $(110)_{Fe}$ peaks are displayed as inset at top-right corner. (**b**) Bright-field image and grain size statistics of as-deformed 75Cu-25Fe sample with 100 rotations.

Supplementary Note 1: Microstructure characterization of as-deformed 75Cu-25Fe alloys.

Supplementary Fig. 1a shows the XRD profiles of compacted powders and as-deformed sample of 75Cu-25Fe. It is clearly shown that the blended powders were severely deformed and formed a single *fcc* phase after 100 rotations deformation. The calculated *fcc* lattice parameter increases from 3.613 ± 0.001 Å for pure Cu powders to 3.634 ± 0.001 Å due to the 25 at.%Fe incorporation. Supplementary Fig. 1b shows the bright-field image of as-deformed 75Cu-25Fe sample with 100 rotations, and the statistics of grain size, which indicates a mean grain size of about 58 nm.

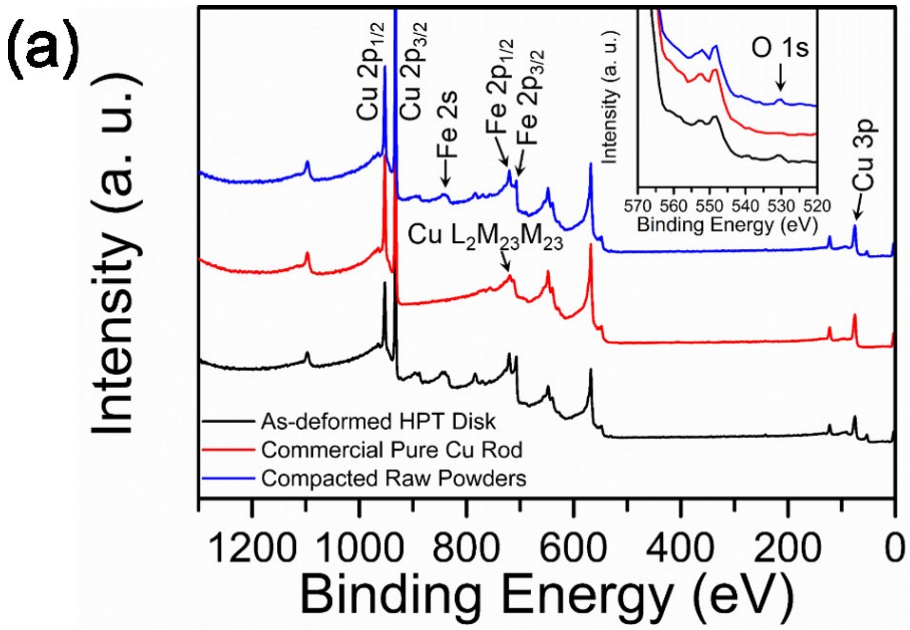
(a)
Intensity (a. u.)
Cu 2p1/2
Cu 2p3/2
Fe 2s
Fe 2p1/2
Fe 2p3/2
Cu L2M23M23
Cu 3p
O 1s
Intensity (a. u.)
570 560 550 540 530 520
Binding Energy (eV)
As-deformed HPT Disk
Commercial Pure Cu Rod
Compacted Raw Powders
1200 1000 800 600 400 200 0
Binding Energy (eV)

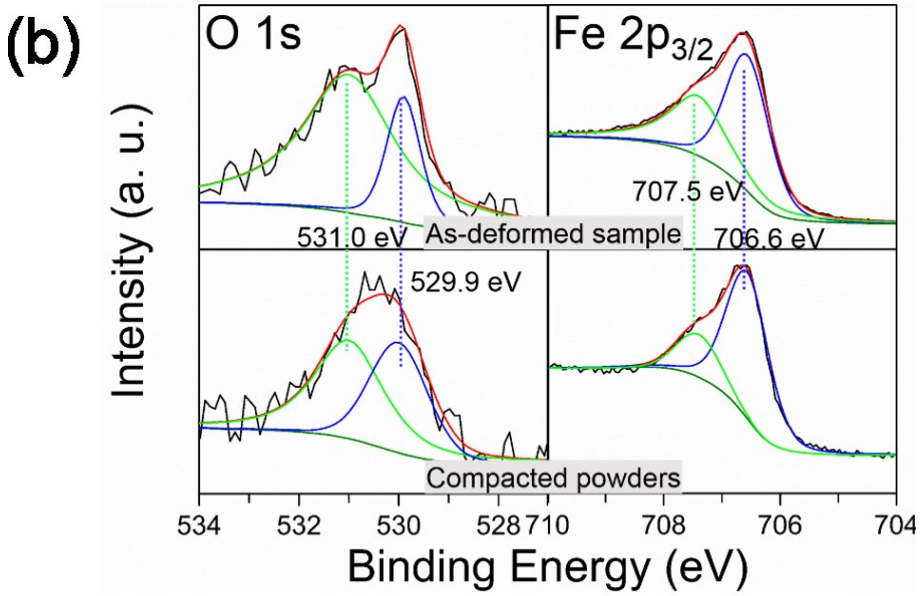
(b)
Intensity (a. u.)
O 1s
Fe 2p3/2
531.0 eV
As-deformed sample
707.5 eV
706.6 eV
529.9 eV
Compacted powders
534 532 530 528 710 708 706 704
Binding Energy (eV)

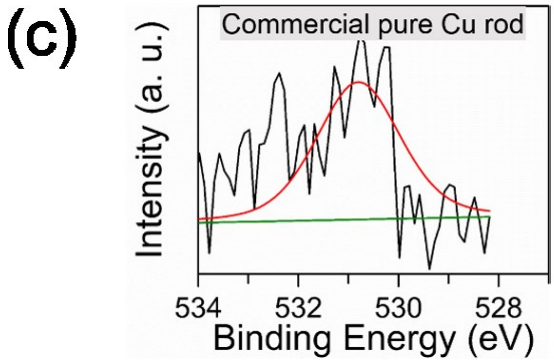
(c)
Commercial pure Cu rod
Intensity (a. u.)
534 532 530 528
Binding Energy (eV)

Supplementary Figure 2: (**a**) XPS spectra of 75Cu-25Fe as-deformed HPT sample (black spectrum), commercial pure Cu rod (red spectrum) and 75Cu-25Fe compacted raw powders (blue spectrum). (**b**) Fine measurements of O 1s and Fe $2p_{3/2}$ peaks of 75Cu-25Fe as-deformed HPT sample and compacted raw powders. (**c**) Fine measurement of O 1s peak of commercial pure Cu rod.

Supplementary Table 1: Constituents of 75Cu-25Fe as-deformed sample, commercial pure Cu rod and 75Cu-25Fe compacted raw powders calculated from respective XPS spectra.

Samples	O (at.%)	Cu (at.%)	Fe (at.%)
As-deformed HPT disk	3.6	74.9	21.5
Commercial pure Cu rod	< 1.0	> 99.0	-
Compacted raw powders	3.0	73.3	23.7

Supplementary Note 2: XPS measurements of constituents of as-deformed samples and comparison samples.

Oxygen contents in the initial raw powders, as-deformed HPT sample and a piece of commercial pure Cu material (nominal purity of 99.99%, used as a reference) were systematically measured by X-ray photoelectron spectroscopy (XPS, ESCALAB 250Xi, Thermo Fisher Scientific, Waltham, USA). We have taken a series of special measures to remove the surface oxide layers before transfer the samples to the XPS chamber. All sample surfaces were fully polished in a media of ethyl alcohol and then transferred to XPS chamber immediately, which was followed by Ar ion sputtering with ion energy of 3 keV for 5 minutes to completely remove the possible surface oxide layers. We would emphasize that all samples were kept in ethyl alcohol after polishing, and the operation time of transfer from ethyl alcohol to XPS chamber was controlled to a minimum of about a few seconds. All three samples mentioned above were transferred into the chamber at the same time.

Supplementary Fig. 2a shows the spectra in a full range of 0 – 1300 eV. Some typical peaks of Cu and Fe are indexed on the profiles. To clearly check the O 1s peaks, the spectra within the region of 520 – 570 eV are enlarged and shown as an inset in Supplementary Fig. 2a. While O 1s peaks can be seen clearly for the 75Cu-25Fe as-deformed sample and the compacted powders, almost no signal can be observed for the commercial pure Cu rod sample at binding energy of 530 – 532 eV. The comparative study by XPS provides the direct evidence of oxygen presence in powder samples.

Supplementary Fig. 2b shows the fine measurements of O 1s and Fe $2p_{3/2}$ peaks of 75Cu-25Fe as-deformed HPT sample and compacted raw powders respectively, and Supplementary Fig. 2c shows the fine measurement of O 1s peak of commercial pure Cu rod. For the Fe $2p_{3/2}$ peak, it can be seen that each well resolved Fe $2p_{3/2}$ spectrum shows multiplet splitting with

second component shifting to a higher energy by 0.9 eV from the main peak. The position of main peak at 706.6 eV and the typical asymmetric peak shape containing a 0.9 eV higher component at 707.5 eV, both attest the Fe atoms are substantially in zero-valent states. If we compare the O 1s peak shown in Supplementary Fig. 2c with the O 1s peaks of 75Cu-25Fe as-deformed HPT sample and compacted raw powders, we can see the signal-to-noise ratio of the O 1s peak of commercial Cu rod is very low and the peak is nearly negligible, which means probably only very tiny amount of oxygen exists in the pure Cu rod. Meanwhile, it proves that our measurements are effective without introducing adsorbed oxygen.

To evaluate the content of oxygen in each sample, peaks of O 1s, Cu $2p_{3/2}$ and Fe $2p_{3/2}$ were selected to quantify the integral areas. Supplementary Table 1 displays the quantification result of the contents of O, Cu and Fe in 75Cu-25Fe as-deformed sample, commercial pure Cu and 75Cu-25Fe compacted powders, taking into account relative sensitivity factors of 2.881 (O), 16.73 (Cu) and 10.7 (Fe). It can be seen that the powder samples contain a level of about 3 at.% oxygen inside material while for commercial pure Cu the oxygen content is less than 1 at.%. It should be emphasized that for the fine scan spectrum of commercial pure Cu, the signal-to-noise ratio of O 1s peak is quite low and it is hard to calculate the integral area of this peak accurately, so the given value here of 1 at.% is very likely overestimated.

The measured oxygen content in 75Cu-25Fe as-deformed disk here is 3.6 at.%. Actually we have also carried out independent measurements for another two as-deformed samples, the oxygen contents in these two samples are 3.4 at.% and 3.3 at.% respectively. So it can be assured that the oxygen content in the HPT as-deformed samples is about 3.5 at.%. As for the reason why the measured oxygen content in the compacted powders is 3.0 at.%, a little bit lower than the value in the HPT-deformed sample, it might be that the pores formed during compaction are segmented and the embedded oxygen react with metal elements during continuous deformation.

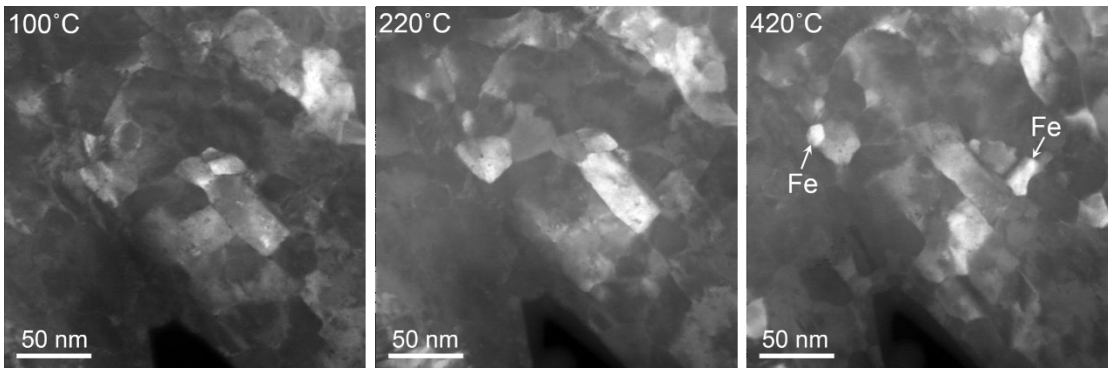

Supplementary Figure 3: *In-situ* observation of microstructure change of 75Cu-25Fe annealed at different temperatures with ADF-STEM image.

Supplementary Note 3: *In-situ* observation of microstructure change of 75Cu-25Fe alloy.

Supplementary Fig. 3 shows the ADF-STEM images of 75Cu-25Fe alloy taken at different temperatures. Intuitively, the grains hardly coarsen as the temperature increases. After the sample was annealed at 420 °C, we carried out EDXS line scans on the newly-grown grains,

which were determined to be Fe grains as indicated by white arrows in the right-hand side image.

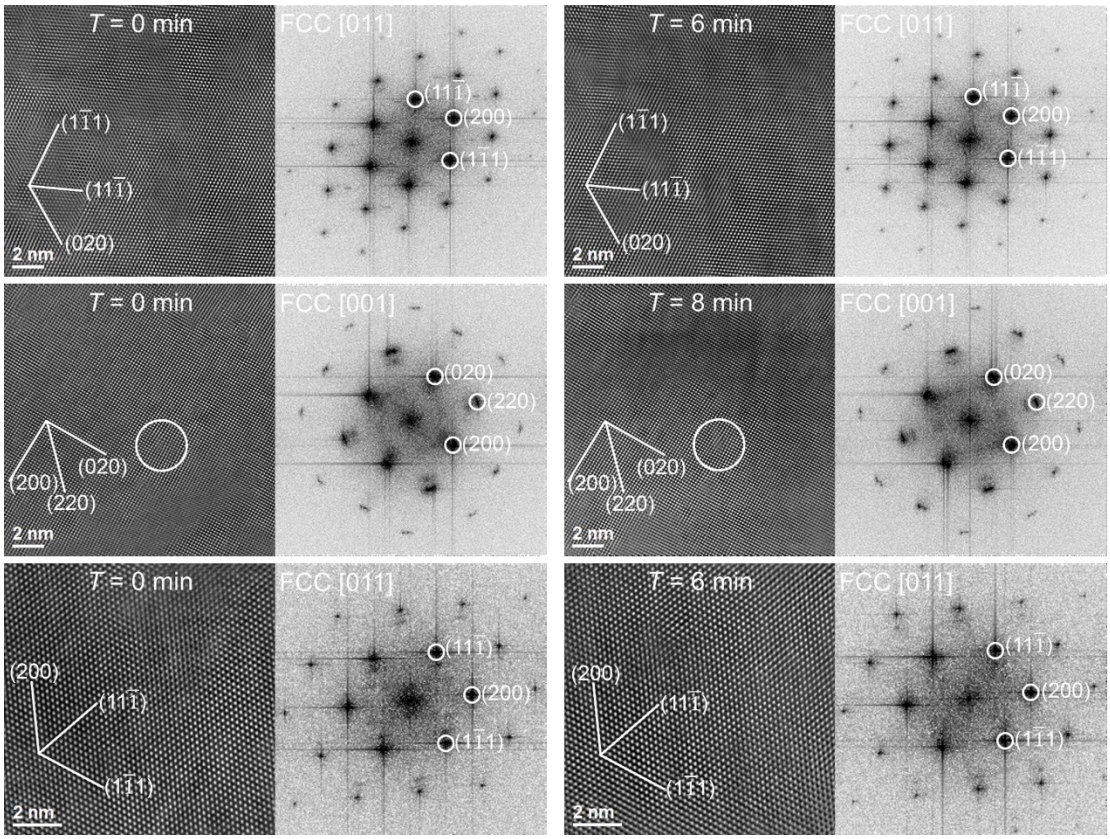

Supplementary Figure 4: Electron beam irradiation test on three different grains (each row represents one grain) with irradiation time of 6 – 8 min.

Supplementary Note 4: Electron beam irradiation test on different grains.

To verify that oxidation and decomposition are not caused by e-beam irradiation, a series of comparative experiments were carried out with a sample exposed to electron beam under the same dose conditions as those in the *in-situ* experiment being performed. The corresponding images under different acquisition time are shown in Supplementary Fig. 4. Electron beam was diverged to a specific size as same as the large fluorescent screen during irradiation. The result shows that after exposure for several minutes, no obvious change has happened. Despite of the complexity of electron beam effects, our systematic experiments proved that beam effects under current conditions are negligible.

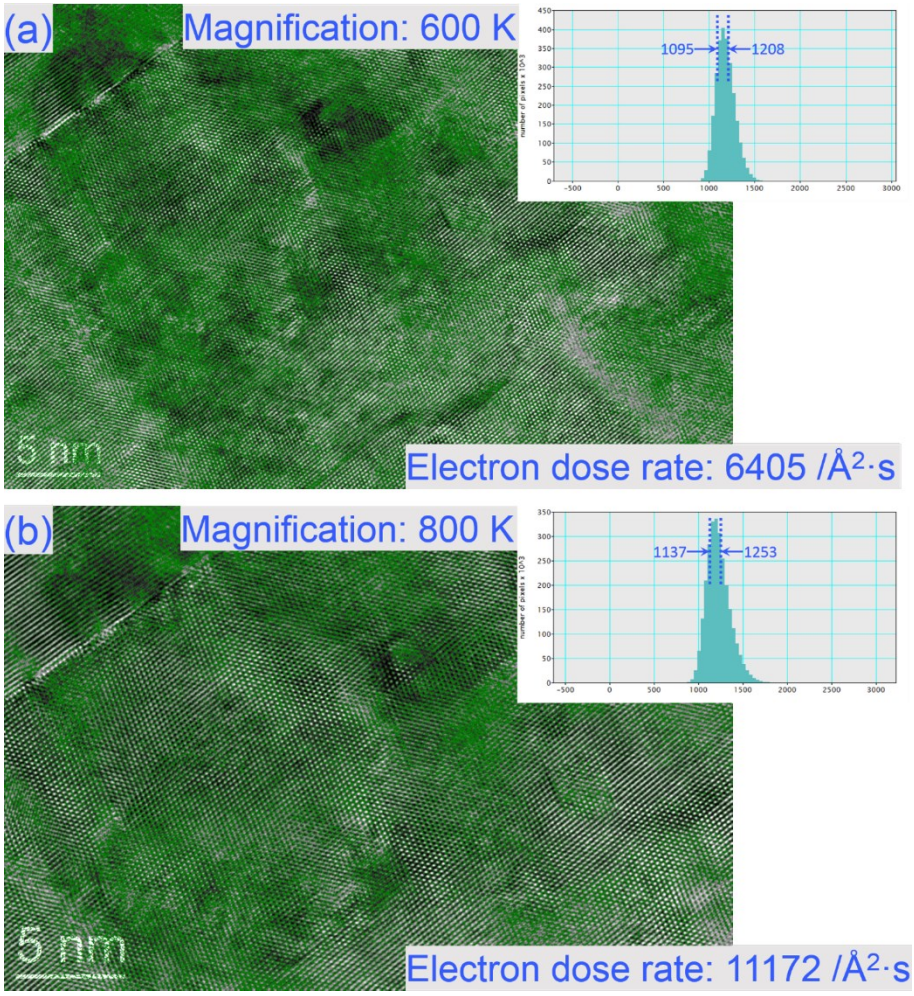

Supplementary Figure 5: Electron dose rate analyses of HRTEM images of the same area taken at magnification of (**a**) 600K and (**b**) 800K. The insets are distributions of the number of pixels versus the counts.

Supplementary Note 5: Electron dose rate analyses of HRTEM images.

In addition, we have quantified the electron dose rate on two images with magnifications of 600K and 800K, respectively, recorded on the same area as shown in Supplementary Fig. 5. The two insets are distributions of the number of pixels versus the counts. The green coverage areas shown in two HRTEM images correspond to the majorities of pixel intensities within a region shown in two insets. With the exposure time of 1 s and beam spreading to fit to the size of fluorescent screen, the electron dose rate for the image taken at magnification of 600K is 6405 /Å^2·s while it is 11172 /Å^2·s for image with the magnification of 800K. Under the imaging conditions as mentioned and configurations of CCD applied, the converted current density is about 68.8 pA/cm^2 for magnification of 600K and 69.2 pA/cm^2 for magnification of 800K respectively. Moreover, because the TEM sample is very thin, the heat dissipation usually proceeds very fast.

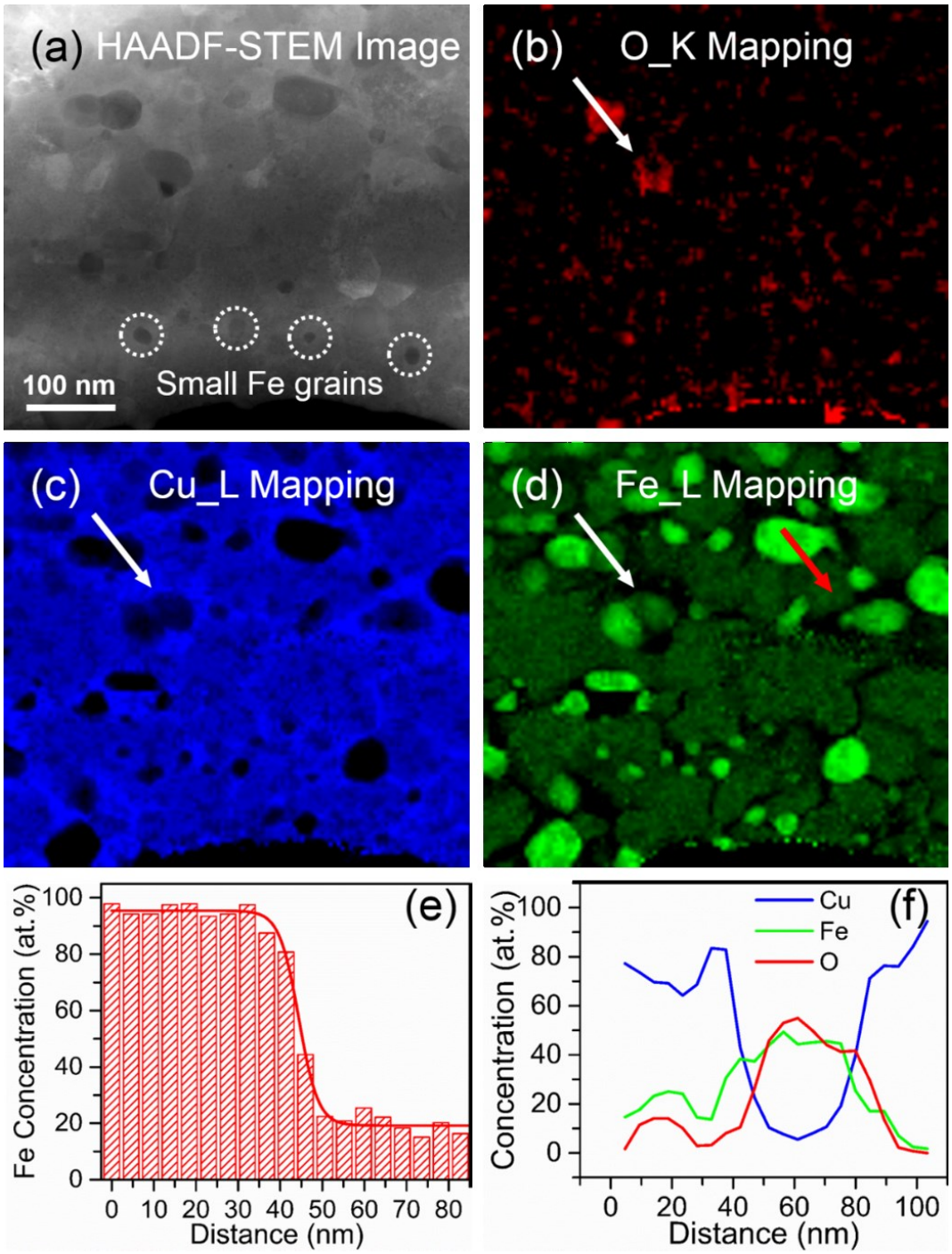

Supplementary Figure 6: EELS elemental mapping of *ex-situ* annealed sample at 420 °C. (**a**) HAADF-STEM image. (**b**) O_K mapping. (**c**) Cu_L mapping. (**d**) Fe_L mapping. (**e**) Fe concentration histogram obtained from line scan along red arrow displayed in (**d**). (**f**) Cu, Fe and O concentration profiles extracted from line scan of the same position indicated by the white arrows in (**b-d**).

Supplementary Note 6: EELS elemental mapping of *ex-situ* annealed sample at 420 °C.

EELS mapping of the *ex-situ* annealed sample was implemented to confirm the EELS mapping results from the *in-situ* heating sample. Supplementary Fig. 6 shows the EELS elemental mapping of the sample *ex-situ* annealed at 420 °C. From the Fe L mapping in Supplementary Fig. 6d, it can be seen that Fe grains grown due to the decomposition usually have rounded corner shapes. The morphologies of Fe grains are almost the same as the *in-situ* annealing results, with grain size of 20 – 50 nm. By comparing the Fe_L mapping, it can be seen that the dark areas in Supplementary Fig. 6a correspond to the Fe grains as marked with white circles. Supplementary Fig. 6b shows the O_K mapping, from which our conclusion on oxides formation during annealing with dimensions from several nanometers to tens of nanometers is proved. Besides some oxide precipitates present at the grain boundaries, many small oxide clusters formed inside the grains as observed by HRTEM images. The Fe concentration histogram shown in Supplementary Fig. 6e was extracted along a red arrow in Supplementary Fig. 6d from a pure Fe grain to the Cu matrix. It can be seen that after *ex-situ* annealing at 420 °C, the residual Fe in Cu matrix amounts to 18 – 20 at.% which is consistent with the result reported in Fig. 3c in the main text. Supplementary Fig. 6f shows line profiles crossing a Fe oxide particle formed within the sample as indicated by the white arrows in Supplementary Fig. 6b-d. It is clearly shown that the Fe and O concentrations reach maxima while Cu concentration is at a minimum, which is a strong indication that Fe oxide forms within the grain instead of on the surface of the sample.

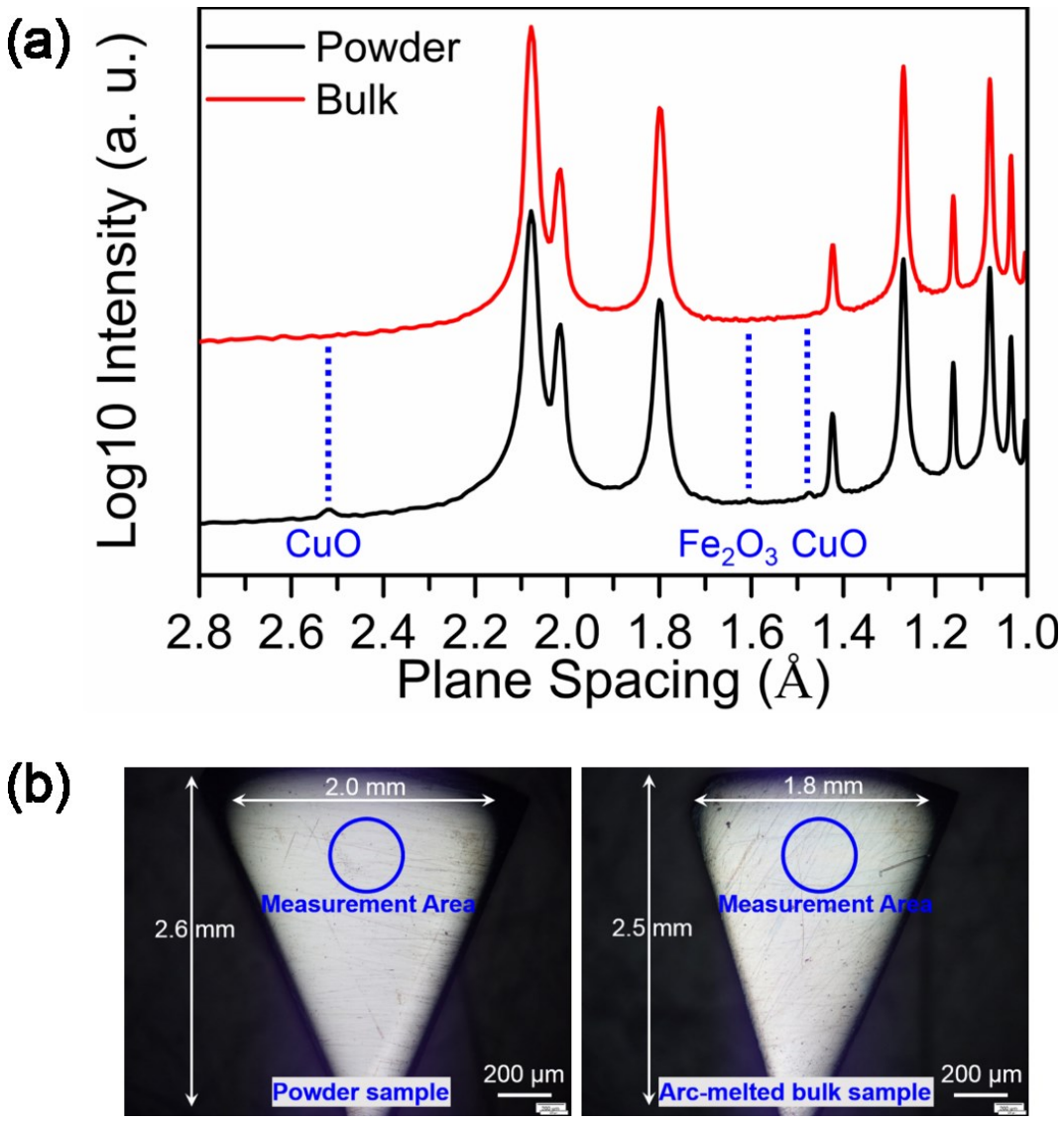

Supplementary Figure 7: (**a**) Synchrotron X-ray diffraction profiles of *ex-situ* annealed 75Cu-25Fe samples at 420 °C, which were deformed from powders and arc-melted bulk respectively. (**b**) Images of powder and arc-melted bulk samples with blue circles indicating the measurement areas.

Supplementary Note 7: Synchrotron XRD measurements of 75Cu-25Fe samples deformed from powders and arc-melted bulk respectively.

To verify that the oxides formed inside materials after annealing, we measured the *ex-situ* annealed samples using synchrotron X-ray diffraction which has an extremely powerful energy to generate peaks even for tiny amounts of components. Synchrotron X-ray diffraction experiments were performed at the PETRA III P07 beamline at the DESY Photon Science facility (Hamburg, Germany). First, we melted a reference sample with the same composition of 75Cu-25Fe using the high purity commercial Cu and Fe rods (nominal purity: 99.99%). Because large pieces of Cu and Fe rods were used in arc-melting process, the potential

influences of the surface oxides could be effectively reduced. Second, the powder sample and arc-melted sample with composition of 75Cu-25Fe were deformed by HPT to the same strains, followed by *ex-situ* annealing in Ar atmosphere at 420 °C at the same time. Then these two samples were cut and polished to the same shape and thickness. Synchrotron X-ray diffraction measurements were implemented on these two samples at the same conditions. Supplementary Fig. 7a shows the synchrotron profiles of *ex-situ* annealed 75Cu-25Fe samples at 420 ˚C, which were deformed from powders and arc-melted bulk respectively. Supplementary Fig. 7b shows the images of powder and arc-melted bulk samples with blue circles indicating the XRD measurement areas. From the diffraction profiles, we can see that except all Cu and Fe peaks locating at almost the same positions, for the profile of the powder sample, some extra peaks appear at the left side of $(111)_{Cu}$ peak as well as between $(200)_{Cu}$ and $(200)_{Fe}$ peaks, which fit to planes of CuO and Fe_2O_3 very well. The obvious peak with spacing of 2.529 Å is indexed as $(002)_{CuO}$, and the peaks at positions of 1.603 Å and 1.475 Å can be indexed as $(120)_{CuO}$/$(122)_{Fe2O3}$ and $(124)_{Fe2O3}$ respectively. We used the arc-melted sample with the same composition as a reference, and the oxides can be only detected for the powder sample. So the synchrotron X-ray diffraction measurements provide a strong evidence that the oxides formed inside the sample after annealing. The detailed results and discussion of the differences between powder sample and arc-melted bulk sample will be given in our next paper.

Supplementary Note 8: DFT Calculations.

Vienna Ab-initio Simulation Package (VASP) was employed to calculate the formation enthalpies of CuO and Fe_2O_3. The projector augmented wave (PAW) method[1] was used to treat the interaction between ion and core electrons. The valence electrons were described using the local density approximation (LDA) and the generalized gradient approximation (GGA) with the exchange-correlation functional of Perdew, Burke and Enzerhof (PBE)[2]. Considering the strong correlation effects between transition metal elements and oxygen, Hubbard U model[3] was also employed. Here in our calculations, for Cu and Fe, U = 3 eV. Convergence tests indicated that 600 eV was a suitable cutoff energy for the PAW potential to obtain sufficient precision in the oxide systems. Brillouin-zone gridding was performed using the Monkhorst-Pack method[4,5] with 23×23×23 (Cu), 21×21×21 (*fcc*-structured Fe), 15×21×13 (CuO) and 17×17×3 (Fe_2O_3) k-point meshes, which were sufficient for structural optimization and static calculation. Energy of oxygen was calculated within a box of 12 Å×12 Å×12 Å. Spin polarization was considered in the Fe and Fe_2O_3 calculations. Using the optimal parameters, the calculated formation enthalpy changes converge to better than 0.1 meV/atom. The results are shown in Supplementary Table 2, which are in reasonable agreements with previous results [6].

Supplementary Table 2: Calculated formation enthalpies of different oxides (eV/atom).

	LDA	LDA+U	GGA	GGA+U
Cu_2O	-0.703	-0.767	-0.599	-0.666
CuO	-1.091	-1.086	-0.873	-0.874
Fe_2O_3	-1.947	-1.980	-1.523	-1.563
FeO	-1.257	-1.745	-1.171	-1.576

Supplementary References

1. Kresse, G. & Joubert, D. From ultrasoft pseudopotentials to the projector augmented-wave method. *Phys*. *Rev*. *B* **59**, 1758–1775 (1999).
2. Perdew, J. P., Burke, K. & Ernzerhof, M. Generalized gradient approximation made simple. *Phys*. *Rev*. *Lett*. **77**, 3865–3868 (1996).
3. Anisimov, V. I., Zaanen, J. & Andersen, O. K. Band theory and Mott insulators: Hubbard U instead of Stoner I. *Phys*. *Rev*. *B* **44**, 943–954 (1991).
4. Monkhorst, H. J. & Pack, J. D. Special points for Brillouin-zone integrations. *Phys*. *Rev*. *B* **13**, 5188–5192 (1976).
5. Cococcioni, M. & De Gironcoli, S. Linear response approach to the calculation of the effective interaction parameters in the LDA+U method. *Phys*. *Rev*. *B* **71**, 035105 (2005).
6. Stevanović, V., Lany, S., Zhang, X. & Zunger, A. Correcting density functional theory for accurate predictions of compound enthalpies of formation : Fitted elemental-phase reference energies. *Phys*. *Rev*. *B* **85**, 115104, (2012).

References

1. Wang, Y., Chen, M., Zhou, F. & Ma, E. High tensile ductility in a nanostructured metal. *Nature* **419**, 912–915 (2002).
2. Yip, S. Nanocrystals: The strongest size. *Nature* **391**, 532–533 (1998).
3. Lu, L., Sui, M. L. & Lu, K. Superplastic extensibility of nanocrystalline copper at room temperature. *Science* **287**, 1463–1466 (2000).
4. Poudel, B. *et al.* High-thermoelectric performance of nanostructured bismuth antimony telluride bulk alloys. *Science* **320**, 634–638 (2008).
5. Valiev, R. Z., Islamgaliev, R. K. & Alexandrov, I. V. Bulk nanostructured materials from severe plastic deformation. *Prog. Mater. Sci.* **45**, 103–189 (2000).
6. Langdon, T. G. Twenty-five years of ultrafine-grained materials: Achieving exceptional properties through grain refinement. *Acta Mater.* **61**, 7035–7059 (2013).
7. Valiev, R. Z. *et al.* Fundamentals of superior properties in bulk nanoSPD materials. *Mater. Res. Lett.* **3831**, 1–21 (2015).
8. Guo, J., Rosalie, J., Pippan, R. & Zhang, Z. On the phase evolution and dissolution process in Cu-Cr alloys deformed by high pressure torsion. *Scr. Mater.* **133**, 41–44 (2017).
9. Guo, J., Rosalie, J., Pippan, R. & Zhang, Z. Revealing the microstructural evolution in Cu-Cr nanocrystalline alloys during high pressure torsion. *Mater. Sci. Eng. A* **695**, 350–359 (2017).
10. Rosalie, J., Guo, J., Pippan, R. & Zhang, Z. On nanostructured molybdenum-copper composites produced by high pressure torsion. *J. Mater. Sci.* **52**, 9872–9883 (2017).
11. Bachmaier, A., Kerber, M., Setman, D. & Pippan, R. The formation of supersaturated solid solutions in Fe-Cu alloys deformed by high-pressure torsion. *Acta Mater.* **60**, 860–871 (2012).
12. Ma, E. Instabilities and ductility of nanocrystalline and ultrafine-grained metals. *Scr. Mater.* **49**, 663–668 (2003).
13. Bachmaier, A. & Pippan, R. Effect of oxide particles on the stabilization and final microstructure in aluminium. *Mater. Sci. Eng. A* **528**, 7589–7595 (2011).
14. Ma, E. Alloys created between immiscible elements. *Prog. Mater. Sci.* **50**, 413–509 (2005).
15. Bachmaier, A., Hohenwarter, A. & Pippan, R. New procedure to generate stable nanocrystallites by severe plastic deformation. *Scr. Mater.* **61**, 1016–1019 (2009).
16. Csiszár, G., Kurz, S. J. B. & Mittemeijer, E. J. Stability of nanosized alloy thin films: Faulting and phase separation in metastable Ni/Cu/Ag-W films. *Acta Mater.* **110**, 324–340 (2016).
17. Wei, L. S., Kim, H. Y., Koyano, T. & Miyazaki, S. Effects of oxygen concentration and temperature on deformation behavior of Ti-Nb-Zr-Ta-O alloys. *Scr. Mater.* **123**, 55–58 (2016).
18. Marvel, C. J., Cantwell, P. R. & Harmer, M. P. The critical influence of carbon on the

thermal stability of nanocrystalline Ni-W alloys. *Scr*. *Mater*. **96**, 45–48 (2015).

19. Hirata, A. *et al.* Atomic structure of nanoclusters in oxide-dispersion-strengthened steels. *Nat*. *Mater*. **10**, 922–926 (2011).

20. Hirata, A., Fujita, T., Liu, C. T. & Chen, M. W. Characterization of oxide nanoprecipitates in an oxide dispersion strengthened 14YWT steel using aberration-corrected STEM. *Acta Mater*. **60**, 5686–5696 (2012).

21. Liu, G. *et al.* Nanostructured high-strength molybdenum with unprecedented tensile ductility. *Nat*. *Mater*. **12**, 344–350 (2013).

22. Ribis, J. & De Carlan, Y. Interfacial strained structure and orientation relationships of the nanosized oxide particles deduced from elasticity-driven morphology in oxide dispersion strengthened materials. *Acta Mater*. **60**, 238–252 (2012).

23. Miller, M. K., Russell, K. F. & Hoelzer, D. T. Characterization of precipitates in MA/ODS ferritic alloys. *J*. *Nucl*. *Mater*. **351**, 261–268 (2006).

24. Mukhopadhyay, D. K., Froes, F. H. & Gelles, D. S. Development of oxide dispersion strengthened ferritic steels for fusion. *J*. *Nucl*. *Mater*. **258–263**, 1209–1215 (1998).

25. Alinger, M. J., Odette, G. R. & Hoelzer, D. T. On the role of alloy composition and processing parameters in nanocluster formation and dispersion strengthening in nanostuctured ferritic alloys. *Acta Mater*. **57**, 392–406 (2009).

26. Miller, M. K., Hoelzer, D. T., Kenik, E. A. & Russell, K. F. Stability of ferritic MA/ODS alloys at high temperatures. *Intermetallics* **13**, 387–392 (2005).

27. Ukai, S. & Fujiwara, M. Perspective of ODS alloys application in nuclear environments. *J*. *Nucl*. *Mater*. **307–311**, 749–757 (2002).

28. Dawson, K., Haigh, S. J., Tatlock, G. J. & Jones, A. R. Nano-particle precipitation in mechanically alloyed and annealed precursor powders of legacy PM2000 ODS alloy. *J*. *Nucl*. *Mater*. **464**, 200–209 (2015).

29. Dawson, K. & Tatlock, G. J. The influence of deformation, annealing and recrystallisation on oxide nanofeatures in oxide dispersion strengthened steel. *J*. *Nucl*. *Mater*. **486**, 361–368 (2017).

30. He, M. R., Yu, R. & Zhu, J. Reversible wurtzite-tetragonal reconstruction in ZnO($10\bar{1}0$) surfaces. *Angew*. *Chem*. *Int*. *Ed*. **51**, 7744–7747 (2012).

31. Fei, L. *et al.* Direct TEM observations of growth mechanisms of two-dimensional MoS_2 flakes. *Nat*. *Commun*. **7**, 12206 (2016).

32. Zheng, H. *et al.* Observation of transient structural-transformation dynamics in a Cu_2S nanorod. *Science* **333**, 206–209 (2011).

33. Wang, S. J. *et al.* Deformation-induced structural transition in body-centred cubic molybdenum. *Nat*. *Commun*. **5**, 3433 (2014).

34. Yue, Y. *et al.* Atomic scale observation of oxygen delivery during silver-oxygen nanoparticle catalysed oxidation of carbon nanotubes. *Nat*. *Commun*. **7**, 12251 (2016).

35. Wang, J. *et al. In situ* atomic-scale observation of twinning-dominated deformation in nanoscale body-centred cubic tungsten. *Nat*. *Mater*. **14**, 594–600 (2015).

36. Xu, W. *et al. In-situ* atomic-scale observation of irradiation-induced void formation. *Nat*. *Commun*. **4**, 2288 (2013).

37. Liao, H. G. *et al.* Facet development during platinum nanocube growth. *Science* **345**, 916–919 (2014).

38. Bachmaier, A., Pfaff, M., Stolpe, M., Aboulfadl, H. & Motz, C. Phase separation of a supersaturated nanocrystalline Cu-Co alloy and its influence on thermal stability. *Acta Mater*. **96**, 269–283 (2015).

39. Gammer, C., Mangler, C., Rentenberger, C. & Karnthaler, H. P. Quantitative local profile analysis of nanomaterials by electron diffraction. *Scr*. *Mater*. **63**, 312–315 (2010).

40. Ching, W. Y., Xu, Y. N. & Wong, K. W. Ground-state and optical-properties of Cu_2O and CuO crystals. *Phys*. *Rev*. *B* **40**, 7684–7695 (1989).

41. Cao, M. *et al.* Single-crystal dendritic micro-pines of magnetic α-Fe_2O_3: Large-scale synthesis, formation mechanism, and properties. *Angew*. *Chem*. *Int*. *Ed*. **44**, 4197–4201 (2005).

42. Wu, C., Yin, P., Zhu, X., Ouyang, C. & Xie, Y. Synthesis of hematite (α-Fe_2O_3) nanorods: Diameter-size and shape effects on their applications in magnetism, lithium ion battery, and gas sensors. *J*. *Phys*. *Chem*. *B* **110**, 17806–17812 (2006).

43. Zeng, Z. *et al.* Visualization of electrode-electrolyte interfaces in $LiPF_6$/EC/DEC electrolyte for lithium ion batteries via in situ TEM. *Nano Lett*. **14**, 1745−1750 (2014).

44. Tian, D., Jona, F. & Marcus, P. Structure of ultrathin films of Fe on Cu {111} and Cu {110}. *Phys*. *Rev*. *B* **45**, 11216–11221 (1992).

45. Jiang, D. E. & Carter, E. A. Carbon dissolution and diffusion in ferrite and austenite from first principles. *Phys*. *Rev*. *B* **67**, 214103 (2003).

46. Barouh, C., Schuler, T., Fu, C. & Nastar, M. Interaction between vacancies and interstitial solutes (C, N, and O) in α-Fe: From electronic structure to thermodynamics. *Phys*. *Rev*. *B* **90**, 054112 (2014).

47. Fu, C. L., Krčmar, M., Painter, G. S. & Chen, X. Q. Vacancy mechanism of high oxygen solubility and nucleation of stable oxygen-enriched clusters in Fe. *Phys*. *Rev*. *Lett*. **99**, 225502 (2007).

48. Schuler, T., Barouh, C., Nastar, M. & Fu, C. C. Equilibrium vacancy concentration driven by undetectable impurities. *Phys*. *Rev*. *Lett*. **115**, 015501 (2015).

49. Anisimov, V. I., Zaanen, J. & Andersen, O. K. Band theory and Mott insulators: Hubbard U instead of Stoner I. *Phys*. *Rev*. *B* **44**, 943–954 (1991).

50. Cococcioni, M. & De Gironcoli, S. Linear response approach to the calculation of the effective interaction parameters in the LDA+U method. *Phys*. *Rev*. *B* **71**, 035105 (2005).

51. Stevanović, V., Lany, S., Zhang, X. & Zunger, A. Correcting density functional theory for accurate predictions of compound enthalpies of formation : Fitted elemental-phase reference energies. *Phys*. *Rev*. *B* **85**, 115104, (2012).

V

Oxygen-mediated deformation and grain refinement in nanocrystalline alloys

Jinming Guo[1], María Jazmin Duarte[2], Yong Zhang[1,3], Gerhard Dehm[2], Reinhard Pippan[1], Zaoli Zhang[1]

[1]*Erich Schmid Institute of Materials Science, Austrian Academy of Sciences, A-8700 Leoben, Austria.*

[2]*Max-Planck Institut für Eisenforschung GmbH, Max-Planck-Straße 1, D-40237 Düsseldorf, Germany.*

[3]*Center for High Resolution Electron Microscopy, College of Materials Science and Engineering, Hunan University, 410082 Changsha, China.*

Light elements play a crucial role on the microstructure and properties of alloys and steels. We show that high pressure torsion can fragment the oxides formed during powder-processing and eventually cause oxygen dissolution in matrix. A comparative investigation on a series of Cu-Fe nanocrystalline alloys reveal that oxygen enrichment at grain boundaries effectively decreases the grain boundary mobility, markedly facilitating grain refinement. The dissolved oxygen atoms as interstitials in the matrix lead to lattice expansion and dramatic decrease of stacking fault energy locally. Such oxygen-mediated microstructure gives rise to enhanced strength at the expense of ductility, and superior structural stability. The remarkable tailoring effect of oxygen can be employed to engineer nanocrystalline materials with desired properties for applications.

Production of applicable bulk ultrafine-grained and nanocrystalline materials using severe plastic deformation (SPD) is drawing growing interest for materials scientists [1,2]. Combined with powder-processing technique, SPD can effectively transform compacted powders into homogeneous and composition-adjustable bulk nanocomposites without further sintering for consolidation [3,4]. Unfortunately, one prominent problem raised during the consolidation and straining processes is the unavoidable contamination from gaseous species, especially oxygen, which generates discrepant microstructures and properties [5].

It is well known that the large fraction of material residing at grain boundaries in nanocrystalline alloys is responsible for their ultrahigh strength, but also undesirable microstructural instability under thermal and mechanical loads. However, they can be manipulated via solute decoration enabling changes in energy, mobility, structure, and cohesion, which can be referred to as "segregation engineering" [6]. Solute decoration is not regarded as an undesired phenomenon but is instead utilized to manipulate specific grain boundary structures, compositions and properties that enable useful material behavior. Hence, apart from the conventional alloying metal elements, ubiquitous "oxygen contamination" can be ingeniously designed to tailor materials' microstructures and attendant properties enriching as clusters at grain boundaries or acting as interstitials. Actually oxygen's decoration role has been preliminarily exemplified by the improved stress-driven stability of pure Al thin films. While shear stress has been pinpointed as the driving force governing mechanically induced grain growth [7], a critical O impurity concentration in Al thin film appears to be required to pin grain boundaries against the coupling of applied stress [8–10]. Molecular dynamics simulations of an Al tilt grain boundary decorated with O atoms also support the notion of a changing critical stress required for coupled grain boundary migration due to an O impurity pinning atmosphere [11]. The simulations found that, the increase in this critical stress was a linear function of the number of oxygen atoms, which was attributed to the additive effect of the local stress signature of each O atom during collective boundary motion.

The general realization that smaller grain-sized materials possessing a higher density of grain boundaries are stronger has led to the often-cited Hall-Petch relation [12,13], which assumes that grain boundaries act as obstacles to plastic deformation within the material. It is well acknowledged that the grains are in a dynamic balance between the continuous refinement and attendant recrystallization during SPD, namely, a competition between hardening rate introduced by dislocation generation and the recovery rate arising from dislocation annihilation and recombination. Therefore, deliberately introducing oxygen atoms at grain boundaries is rationalized to hinder their migration by decreasing grain boundary energy [9], which can facilitate grain refinement and finally lead to finer grains in deformed materials.

Furthermore, besides the light elements enrichment at grain boundaries, it has been reported that cold-drawing of pearlitic steel can result in carbon supersaturation in the Fe matrix which far exceeds the equilibrium solubility limit, and a spontaneous tetragonal distortion of the ferrite unit cell [14]. Therefore it is assumed that a high density of vacancies and dislocations in SPD-generated nanocrystalline bulk alloys can similarly accommodate the excess oxygen which has a smaller atomic radius than carbon. Yu *et al*. revealed that the strengthening effect of dilute oxygen solutes in pure *a*-Ti due to the interaction between oxygen and the core of screw dislocations, which is derived from the distortion of the interstitial sites at the screw dislocation core creating a very strong but short-range repulsion to oxygen [15]. The initially oxygen contaminant can be dissolved into the matrix under SPD, and act as the obstacles to dislocation motion, akin to the impeding effect of intergranular oxygen enrichments on grain

boundary migration. These two aspects are extremely favorable for strengthening materials as well as improving structural stabilities.

Although previous studies have tried to approach the oxygen effects in SPD generated bulk composites by qualitative observations [16,17], a detailed investigation of oxygen's influences on microstructural evolution and resultant mechanical properties is still lacking. Moreover, the deformation and grain refinement mechanisms in oxygen-involved nanocrystalline alloys, and the consequent microstructural changes related to defects, interfaces and boundaries are still controversial.

Our previous work via *in-situ* heating in a transmission electron microscope (TEM) showed that for Cu-Fe nanocrystalline alloys fabricated by SPD using initial powder materials, nanometer-sized CuO and Fe_2O_3 clusters formed inside the grains even at low annealing temperatures [18]. Since oxygen is inevitably involved in the powder processing procedures, it is of great importance to explore the oxygen effects in nanocrystalline alloys. To this end, here, a series of Cu-Fe alloys incorporated with different contents of Fe are severely deformed via high pressure torsion (HPT) until reaching ultimate strain-saturated states with single face-centered cubic (*fcc*) structures from two types of initial materials, blended powders and arc-melted bulk, which contain different levels of oxygen content. The systematical atomic-resolution investigation uncovers the governing deformation mechanism in oxygen-existed nanocrystalline alloys involving theories of grain boundary migration, stacking fault energy and solid solution hardening. In addition, atomic-scale observations of nanotwins and stacking faults give a first experimental evidence to indicate that dissolved oxygen interstitials by SPD can significantly decrease stacking fault energy locally, generating higher fraction of nanotwins. Our findings present a role of potent strengthener on tailoring nanocrystalline materials' microstructure and properties.

Results

Microstructure discrepancies between powder and bulk samples. Results of the microstructure characterizations are shown in Fig. 1 for as-deformed samples from both blended powders (abbreviated as powder samples) and arc-melted bulk (abbreviated as bulk samples). After severe deformation, Fe is fully dissolved into the Cu matrix forming a single *fcc* phase for all Cu-Fe samples. The lattice parameters calculated based on $(111)_{fcc}$, $(200)_{fcc}$, $(220)_{fcc}$, $(311)_{fcc}$, $(222)_{fcc}$ diffraction planes for both powder and bulk samples increase with increasing Fe content (see Fig. 1a), i.e., Fe dissolution facilitates the expansion of the *fcc* matrix. Simultaneously, oxygen impurities also play a big role on the lattice parameter of the as-deformed alloys. Powder samples which have higher oxygen concentrations possess larger lattice parameters compared to bulk samples with the same compositions. For example, the lattice parameter of the bulk sample increases from 3.6176 Å for composition of 95Cu-5Fe to 3.6309 Å for 65Cu-35Fe, while for powder samples of the same compositions, the change is from 3.6203 Å to 3.6379 Å. In sum, incorporation of Fe and O can both effectively promote the lattice expansion of the final nanocrystalline alloys.

The obtained average grain sizes based on large population statistics are shown in Fig. 1b for all compositions. It is quite evident that Fe solutes can significantly refine the grains, that is, higher Fe concentration results in finer grains. Especially, for samples with Fe additions of less than 15 at.%, the refinement effect is extremely pronounced. Similarly as the influence of oxygen impurity on the lattice parameter, powder sample has an obviously smaller grain size as compared to the same composition sample deformed from arc-melted bulk. Therefore, on

the whole, except for the influence from Fe, even with the same composition, the samples deformed from different initial materials have large differences on morphologies, which are obviously related to the oxygen impurity in the materials.

Both Fig. 1c and Fig. 1d show the TEM bright-field images of 75Cu-25Fe powder and bulk samples respectively. It can be seen that the powder sample has many grains with nanotwins (see white arrows in Fig. 1c), while nearly no twins are detected in the bulk sample. To characterize the twin density in single *fcc* phase Cu-Fe alloys, the known method of calculating twin probability β from the X-ray diffraction (XRD) patterns is used, which is defined as the probability of finding a twin boundary between any two neighboring {111} planes [19–22]. It is found that the twin probability is indeed higher in the powder sample, e.g. about 1.08%, than that in bulk sample, e.g. about 0.06%. This is in accordance with the TEM observations.

Moreover, many atomic-scale nanotwins and stacking faults are observed in powder samples as shown in Fig. 1e-g, which supports the observation from the low magnification images as well as the XRD calculation. Fig. 1e is a high resolution TEM (HRTEM) image along $[0\bar{1}1]$ with a stacking fault several atomic layers far away from a nanotwin. Fig. 1f displays a interlock of nanotwins which are activated on two slip {111} planes inside a grain under progressive strain, and Fig. 1g exhibits a deformation twin highly interacted with defects forming twin steps. It can be seen that twins are thickened by passage of some steps as shown by white circles in Fig. 1f,g. The twin steps are associated with a few Shockley partial dislocations. Such deformation twin is believed to grow via the well-known pole mechanism in *fcc* materials [23,24]. Once a twin is nucleated, the twin dislocation (Shockley partial dislocation) moves from one slip plane spirally to the next, making the twin thicker and finally lenticular-shaped [23].

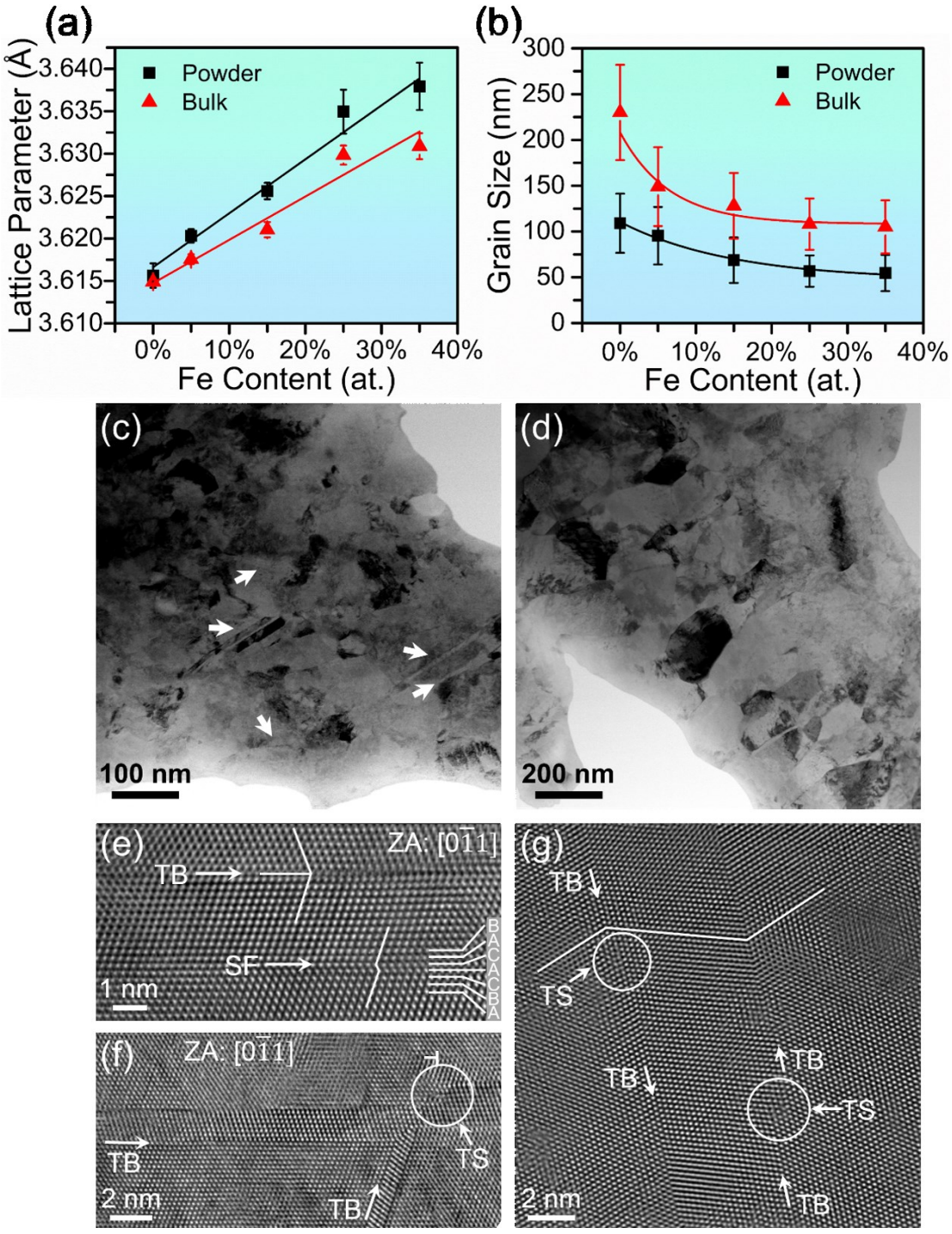

Fig. 1 Microstructure characterization of as-deformed Cu-Fe alloys. (a) Lattice parameter and (b) grain size changes as a function of Fe content. (c),(d) TEM bright-field images of 75Cu-25Fe powder and bulk samples. (e) HRTEM image on zone axis (ZA) of [0$\bar{1}$1] shows a stacking fault (SF) and a nanotwin. (f) Interlock of nanotwins inside a grain. (g) Deformation twin highly interacted with defects forming twin steps (TS).

Mechanical properties of powder and bulk samples. The hardness values of all Cu-Fe alloys deformed from powders and arc-melted bulk with various Fe contents are shown in Fig. 2a. The hardness improvement with increasing Fe content is found for both powder and bulk samples. Simultaneously, the bulk sample shows a significantly lower hardness compared to the powder sample of the same Fe content. Fig. 2b plots the relationship of hardness and grain size following the Hall-Petch equation [25–27], where k_p and k_b are slopes of the fitted lines for powder and bulk samples respectively. The slope of the bulk samples is much larger than that of powder samples with a k_b value of 6556 $HV \cdot nm^{-1/2}$ compared to k_p of 3159 $HV \cdot nm^{-1/2}$. Since grain boundaries represent obstacles for dislocation motion and dislocations can pile up at grain boundaries, the smaller value of k_p denotes that the hindering effect of grain boundaries in powder sample is comparatively less pronounced than in the bulk sample. Here it should be noted that the plot of relationship between hardness and grain size (Fig. 2b) is to simply embody the differences of mechanical properties between powder and bulk samples. Solid solution hardening of Fe alloying and interstitial oxygen's impeding effect on the dislocations are another two aspects which also contribute to the hardness improvements in powder samples [15,28,29]. However, Edalati *et al*. concluded that in the single-phase alloys the contribution of solid-solution hardening is less than 15% of total hardening [29]. In addition, oxygen atoms impose a impeding action on the dislocation motion and then strengthen the materials, as exemplified by the hardening effect of oxygen solutes pinning dislocations in pure α-Ti [15]. Considering the relatively small amount of dissolved oxygen, i.e. less than 0.31 at.%, we can deduce that the most important hardening mechanism in current Cu-Fe alloys is still ascribed to a decrease of grain size, obeying grain boundary hardening mechanism. Another two above-mentioned hardening effects are reflected in the difference of the slopes. Besides, it is worth emphasizing that oxygen hardening effect should be discriminated from the solid solution hardening, which could be better termed as "interstitial light element hardening".

The stress-strain curves shown in Fig. 2c provide the maximum stress and strain to fracture of 75Cu-25Fe powder and bulk samples. The powder sample has an ultimate tensile strength of about 1300 MPa and a failure strain of 2.6%, while for the bulk sample the ultimate strength and failure strain are 910 MPa and 7.8%. Hence, the pronounced influence of oxygen on the tensile properties contributes to a 43% higher ultimate tensile strength while it deteriorates the ductility by about 67%. Fracture surfaces of the tensile tested specimens are examined in detail by scanning electron microscope. Fig. 2d and 2e display the fractographs of powder and bulk samples respectively. Obviously, the bulk sample possesses much deeper and larger dimples with an average size of about 2 μm compared to that of 0.2 μm for powder sample, which also accounts for the much better ductility for bulk sample [30,31].

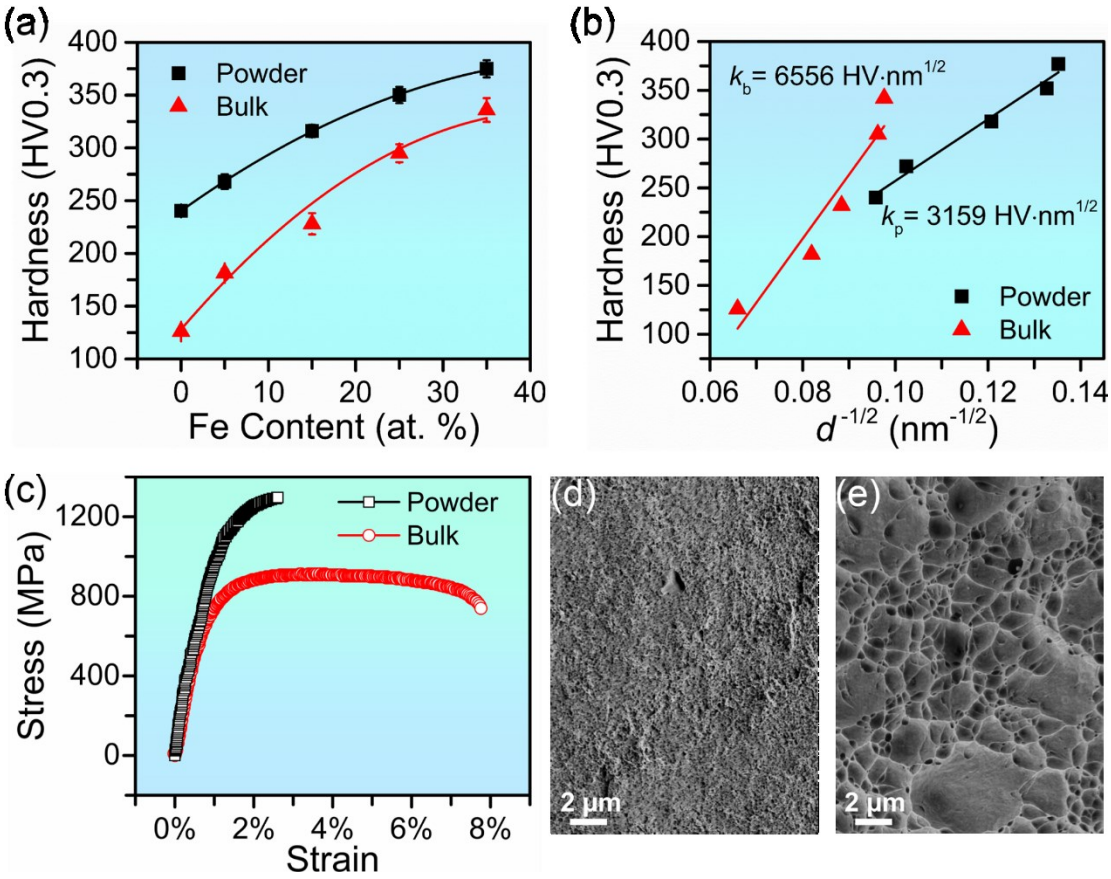

Fig. 2 Mechanical properties of as-deformed Cu-Fe alloys. (a) Hardness change as a function of Fe content. (b) Hall-Petch relationship between hardness and grain size. (c) Tensile experiment results of 75Cu-25Fe powder and bulk samples. (d),(e) Fractographs of 75Cu-25Fe powder and bulk tensile-testing samples respectively.

Oxygen distribution and theoretical calculations. To check the oxygen state at the atomic scale after severe deformation, we annealed both powder and bulk samples at 300 °C and performed atom probe tomography (APT) measurements. Fig. 3a displays the overview image and O distribution of a 75Cu-25Fe powder sample. The overview image shows a mixture of Fe and O clusters embedded in the Cu matrix due to thermal decomposition. It can be seen from the bottom APT O distribution image that in addition to a rather homogeneous oxygen distribution some clusters with sizes of 3 – 8 nm exist at the grain boundaries. APT shows a strong evidence that oxygen atoms can be dissolved by SPD into the matrix. Quantification of the oxygen content provides a value of 0.310 at. % O for the powder sample while 0.047 at.% O are contained in the bulk sample. X-ray photoelectron spectroscopy provides similar results confirming that the O content of the powder sample exceeds more than ten times that of the bulk sample.

In order to confirm the oxygen effect on the lattice expansion shown in Fig. 1a, we carried out density functional theory (DFT) calculations to obtain the relationship between lattice parameters and different contents of interstitial oxygen in the *fcc* matrix. Here to simplify the explanation, a pure Cu unit cell containing 32 atoms is employed as a reference, followed by

introducing 1 (3.03 at.%) and 2 (5.88 at.%) interstitial oxygen atoms, respectively. For each oxygen concentration, 5 different combinations of interstitial sites are considered for oxygen atoms, and in addition 5 nodes are included in the calculations for each combination of atom sites. The calculated results of lattice parameter as a function of oxygen concentration are displayed in Fig. 3b, where the lattice parameter of each oxygen concentration is the average value of all 5 conditions mentioned above. Generally, it can be seen that the lattice parameters increase linearly as the increment of oxygen concentration, while the lattice distortion appears with *c* axis elongating faster than *a* and *b* axes at the oxygen concentration of 5.88 at.%. Here, we should emphasize that the DFT calculation in a 32 atoms unit cell with highest oxygen concentration of 5.88 at.% is only to testify the oxygen-induced lattice expansion effect. Actually it is unknown whether such a high amount of oxygen can be fully dissolved into matrix lattices as interstitials by severe plastic deformation, so it needs further experimental confirmation. In our Cu-Fe powder samples, we have measured the oxygen concentration of about 0.31 at.%, so it is valid to regard that the lattice cell expands linearly as shown in Fig. 3b.

Discussion

As for the grain size in strain-saturated state displayed in Fig. 1b, different mechanisms can be attributed to the variations for HPT deformed nanocrystalline alloys. Stacking fault energy (SFE), solid solution hardening and grain boundary migration theories are supported by different reports and it is still under debates which one dominates the grain refinement process during SPD [29,32–39]. It is well documented that in SPD approaches, grain size (or subgrain size) of the deformed material decreases with increasing applied strain, and finally reaches a steady-state value d_{min} [34,37,39]. d_{min} is governed by a dynamic balance between the hardening rate introduced by dislocation generation and the recovery rate arising from dislocation annihilation and recombination [39], so it seems natural that SFE and solid solution hardening play decisive roles in grain refinement because they generally affect dislocation mobility and storage. In addition, numerous studies on Cu-Zn, Cu-Al and Al-based alloys attempted to bridge the steady-state grain size with stacking fault energy, and indeed obtained reasonable success [34–36,40,41]. For instance, as reported in pure aluminum or aluminum-based alloys where the SFEs are high, the grains of these materials can only be refined invariably down to the range of ~200 nm to ~1.5 μm. By contrast, deformation twinning and twin fragmentation in low SFE materials can refine the grain size to several tens of nanometers during severe plastic deformation [35–37,43].

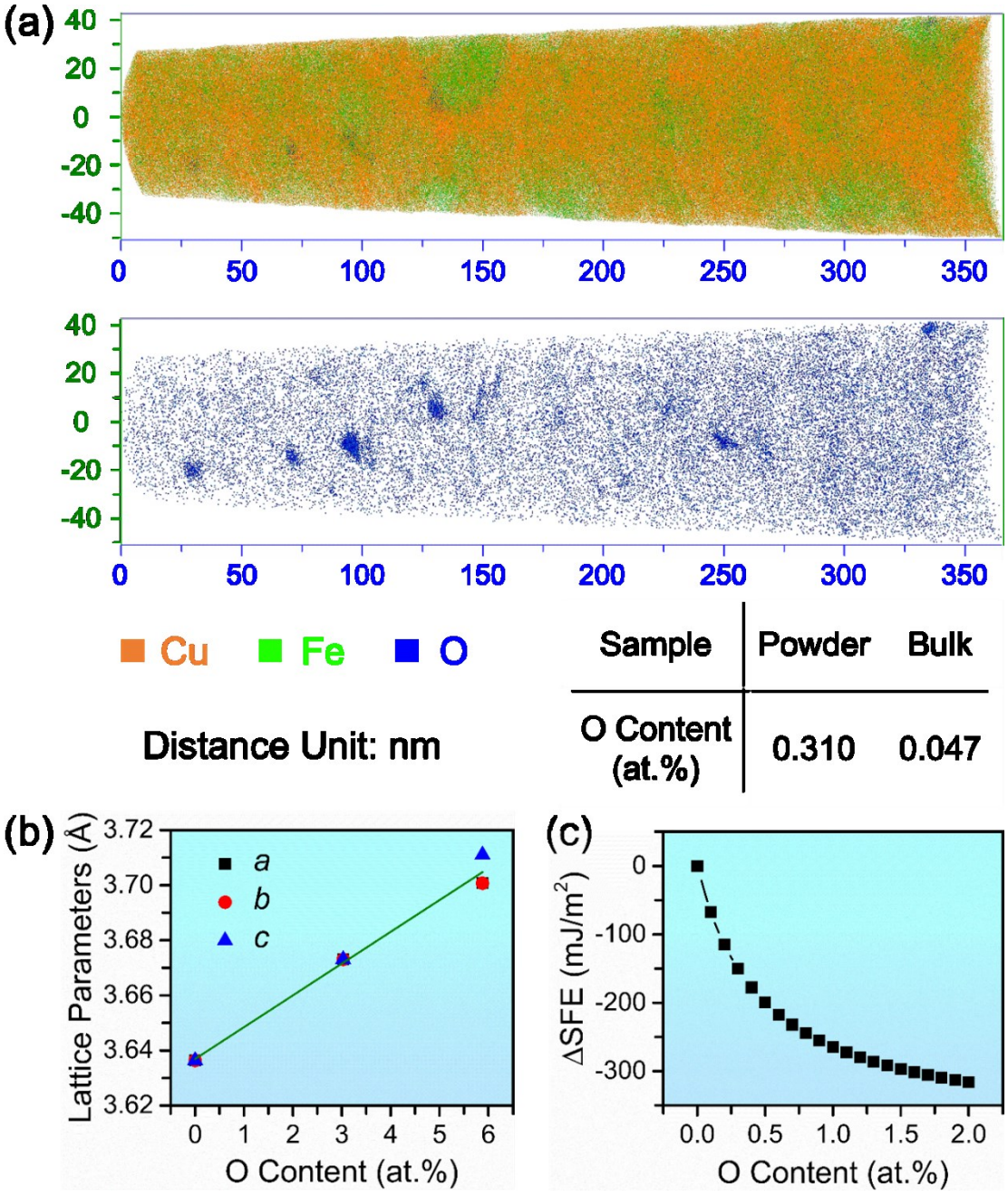

Fig. 3 (a) APT results of annealed 75Cu-25Fe powder sample. Upper image is an overview image containing Fe and O clusters, and the bottom image shows the O-rich distribution. The O contents in powder and bulk samples are listed in the table. (b),(c) DFT calculations show the lattice parameter and SFE changes as a function of O content, respectively.

Oxygen's lowering effect on stacking fault energy. To investigate the oxygen's influence on the SFE, we conducted DFT calculation of the SFE change as a function of oxygen concentration as shown in Fig. 3c. The SFE of pure Cu is 54 mJ/m^2 and the calculation model can be referred to references [43–45]. It can be clearly seen that the intrinsic SFE decreases seriously as the increase of oxygen concentration. The calculation regards that oxygen atoms occupy octahedral-interstitial sites, and the distribution of oxygen atoms at each (111) slip plane follows the Fermi-Dirac rule [43,44]. This calculation gives an evidence of that the dissolved oxygen can drastically decrease the SFE of Cu-based nanocrystalline alloys. It is well known that the light elements such as C, N, O and H have strong correlation effects with transitional metals, therefore these interstitial atoms can be strongly trapped by the stacking fault structures due to the quite large attractive interactions [43]. Therefore it is possible for the sharp decrease of SFE to even get negative values [43], if a twinned structure triggered e.g. by impurities is more stable than the untwinned structure. By means of HPT with extremely large strains, a certain amount of oxygen can be dissolved into the matrix forming nonequilibrium solid solution. Furthermore, DFT calculation has proved that light elements only have short-range attractive interactions with {111} planes, within a distance of two (111) atomic layers [43]. Hence, it can be reasonably speculated that the nanotwins and stacking faults mainly reside at the vicinity of oxygen solutes due to the locally drastic decrease of SFE, while it needs further experimental investigations. Anyway, a calculated decrease trend and magnitude of SFE can be of sufficient significance to interpret the discriminative microstructures in powder and bulk samples, which is consistent with the previously reported SFE lowering effects by C, N, O and H interstitials in Cu- and Al-based alloys [43,44].

According to the TEM observations and XRD results, although a much higher fraction of nanotwins and stacking faults are observed in the powder samples than in the bulk samples, their amounts are still in a low amount range in general compared to the pure twinning deformation dominated systems [41,46]. In our powder samples, the dissolved oxygen content is less than 0.31 at.% (roughly equivalent to 1 oxygen atom in a Cu-Fe matrix with 320 atoms) because of the oxygen enrichment at the grain boundaries. Based on the assumption of that all dissolved oxygen atoms are homogeneously distributed inside Cu-Fe matrix, it can be easily estimated that the mean distance between two oxygen atoms is larger than ten (111) atomic layers. However, in reality many oxygen atoms will agglomerate together forming oxygen clusters inside the grains, so the real distance between two oxygen atoms must be much larger than this estimated value. Thus, the current dissolved amount of oxygen is still not high enough to generate a large fraction of nanotwins and stacking faults, and to dominate the deformation. In conclusion, there is no doubt that lowering SFE can generate more planar defects in grains, and influence the deformation behavior, while it is not a predominant deformation mechanism in current materials. Meanwhile, it is worth noting that this study delivers an effective pathway to adjust the density of planar defects by dissolving a certain amount of oxygen atoms, which may subsequently affect the deformation in nanocrystalline materials.

Solid solution hardening effect. The mechanism of solid solution hardening suggests the atomic-size and modulus mismatch effects of solutes, which increase the resistance to the motion of edge dislocations [29]. For alloys, solute atoms play a role in enhancing the shear stress required for dislocation movement. Labusch suggested a model calculating the shear stress change $\Delta\tau$ based on the atomic size mismatch ε_b and the modulus mismatch $\varepsilon_G^{'}$ [47]:

$$\Delta\tau = \frac{G\left[\varepsilon_G^{'\,2}+(15\varepsilon_b)^2\right]^{2/3} c^{2/3}}{\varphi} \quad (1)$$

where G is the shear modulus, c is the solute concentration, $\varphi = 550$ for *fcc* alloys. According to this equation, Edalati *et al*. plotted the steady-state grain size against the term of the influence of atomic size mismatch and modulus mismatch [29], and found the decreasing trend of the steady-state grain size as the increasing shear stress. Cu and Fe have shear moduli G of 48 GPa and 82 GPa, atomic radii of 127.8 pm and 126 pm respectively. These differences can be responsible for the solid solution hardening effect in Cu-Fe alloys, and the steady-state grain size reduces as the increase of Fe solute concentration. Nonetheless, this can hold for the Fe alloying effect if we only compare the steady-state grain size as a function of Fe content, without considering the influence of oxygen.

Influence of interstitial oxygen hardening. As mentioned previously, besides the solid solution hardening from Fe alloying, oxygen's effect seems to be more pronounced than that of Fe solutes. For instance, when the Fe concentration increases from 5 at.% to 25 at.% for bulk samples, the grains get refined from mean value of 149 nm down to 108 nm by decreasing 27.5%. While a relatively small amount of oxygen is introduced into 75Cu-25Fe alloy, the grain size dramatically decreases to 57 nm by dropping off 47.2%. Based on the equation (1) of Labusch model and the formula (1) in a reference [9], the calculated shear stress induced by oxygen could be underestimated, because these models considered conditions of substitutional solutes rather than interstitials. The large atomic size mismatch and electronegativity of oxygen atoms will generate strong interactions with Cu(Fe) lattices, akin to the strong trapping effect of stacking faults to oxygen atoms within a distance of two atomic layers. The dominant factor for extra grain refinement by both of the substitutional alloying and dissolved oxygen's hardening is the effect of atomic-size and modulus mismatch on the mobility of edge dislocations. The solute atoms increase the localized stress needed for dislocation motion, and thus diminish the dislocation recovery, recrystallization and grain boundary migration. Taking into account the relatively low dissolved oxygen amount of 0.14 at.%, albeit dissolved oxygen impedes the motion of edge dislocations and thus weakens their recovery process, "interstitial oxygen hardening" cannot account for the large decrease of steady-state grain size in powder samples. We have calculated that dislocation density of 75Cu-25Fe powder sample is about 7.53×10^{15} m^{-2}. Assuming the edge dislocations randomly distribute in the matrix, and the oxygen atoms with content of 0.14 at.% homogeneously dissolve as interstitials, only about 1.9% of dislocations can interact with oxygen atoms based on a simple mathematical probability model, where oxygen can only trap dislocations within a short distance of two (220) planes. If oxygen's hindering effect is to be the predominant mechanism of deformation with impeding more than 50% edge dislocations, a minimum dissolved content of 8.4 at.% oxygen is needed (details of calculation can be referred to Supplementary Information). The limited "interstitial oxygen hardening" is consistent with the view of Ref. [9] according to its prediction of oxygen's strengthening effect.

The dominant mechanism of grain boundary migration effect. The above-mentioned effects of stacking fault energy, solid solution hardening and interstitial oxygen hardening contribute to the grain refinement, while they are not dominant mechanism in oxygen-involved Cu-Fe alloys. It is known that in the saturation regime, the generation of defects, i.e., dislocations, vacancies, and new boundaries, has to be in equilibrium with the annihilation of these defects, which represents that the continuous refinement rate is equivalent to that of recovery process. Grain boundary migration during deformation embodies the so-called recovery process, which limits further grain refinement during SPD. Segregations at grain boundaries is an effective measure to lower grain boundary energy, and in turn limit grain boundary migration, which is usually called pining of grain boundaries. By appropriate

decoration of the grain boundaries, nanocrystalline materials can be engineered to achieve specific microstructures and resultant properties.

As shown in Fig. 3a of APT image, some oxygen enrichments are found in the powder samples which locate at the grain boundaries. To detect the fragmentation process and the distribution of the oxides, the technique of diffraction contrast imaging via virtual apertures [48] is employed, as displayed in Fig. 4a-d. The sources of oxygen can be from native oxide layers coated on the micron-sized particles of raw powders, which are introduced during powders premixing and residual air voids after the compaction. Because of the nature of brittleness, oxide particles are fragmented in the deformation process. Fig. 4a is a bright-field image and Fig. 4b shows the corresponding diffraction pattern, where diffraction spots of oxides (CuO and Fe_2O_3) are present. Fig. 4c displays a dark-field image of two neighboring Cu grains, and Fig. 4d shows the oxide distribution recorded with the diffraction spots marked in the blue circle in Fig. 4b. These images clearly show that the elongated oxides locate at the grain boundaries with a dimension of about 10 nm even only after deformation of 5 rotations. Nevertheless, quite a large proportion of oxides are dissolved into the grains and can be barely detected any more by this technique after deformation of 25 rotations (shown in Supplementary Information). Fig. 4e displays a schematic diagram of oxide fragmentation and dissolution processes as described above.

The high density of grain boundaries in nanocrystalline materials creates a vastly increased quantity of enrichment sites making it possible to raise solute concentration levels far beyond the conventional solubility limit. The oxygen enrichment at grain boundaries serves to decrease the grain boundary energy γ, as described by Gibbs' adsorption equation [49]:

$$d\gamma = -\Gamma d\mu_{sol.} \tag{2}$$

where Γ is the solute coverage on the grain boundary plane, $\mu_{sol.}$ is the chemical potential of the solute. Eq. (2) can be rewritten in the dilute limit in terms of the solute concentration in the lattice c and the enthalpy of segregation (enrichment) $\Delta H_{seg.}$ as [9,50]:

$$\gamma = \gamma_0 - \Gamma(RT \ln c + \Delta H_{seg.}) \tag{3}$$

where γ_0 is the grain boundary energy of the pure solvent, R is the ideal gas constant, and T is the temperature. Eq. (3) demonstrates the decrease of γ from γ_0 with increasing solute enrichment at the grain boundary, allowing for $\gamma \leq 0$ with sufficiently high combinations of $\Delta H_{seg.}$ and/or Γ. In a nanocrystalline system with solute enrichment at the grain boundary, grain growth would establish a competition between the energy loss due to decreasing grain boundary area and the energy gain owing to the banishment of solutes to the lattice caused by decreased enrichment sites [50]. Therefore, a metastable equilibrium will exist with $\gamma = 0$, which corresponds to a particular grain size, $\Delta H_{seg.}$ and Γ. Based on the research of Millett *et al*. [50], when the solute density at the grain boundary reaches 2 – 4 atoms/nm^2, for most of cases the grain boundary energy is reduced to 0 or even a negative value. Combining our experimental results with these theories, it can be concluded again that the oxides at grain boundaries are the predominant factor responsible for the finer steady-state grain size in powder samples by lowering grain boundary energy.

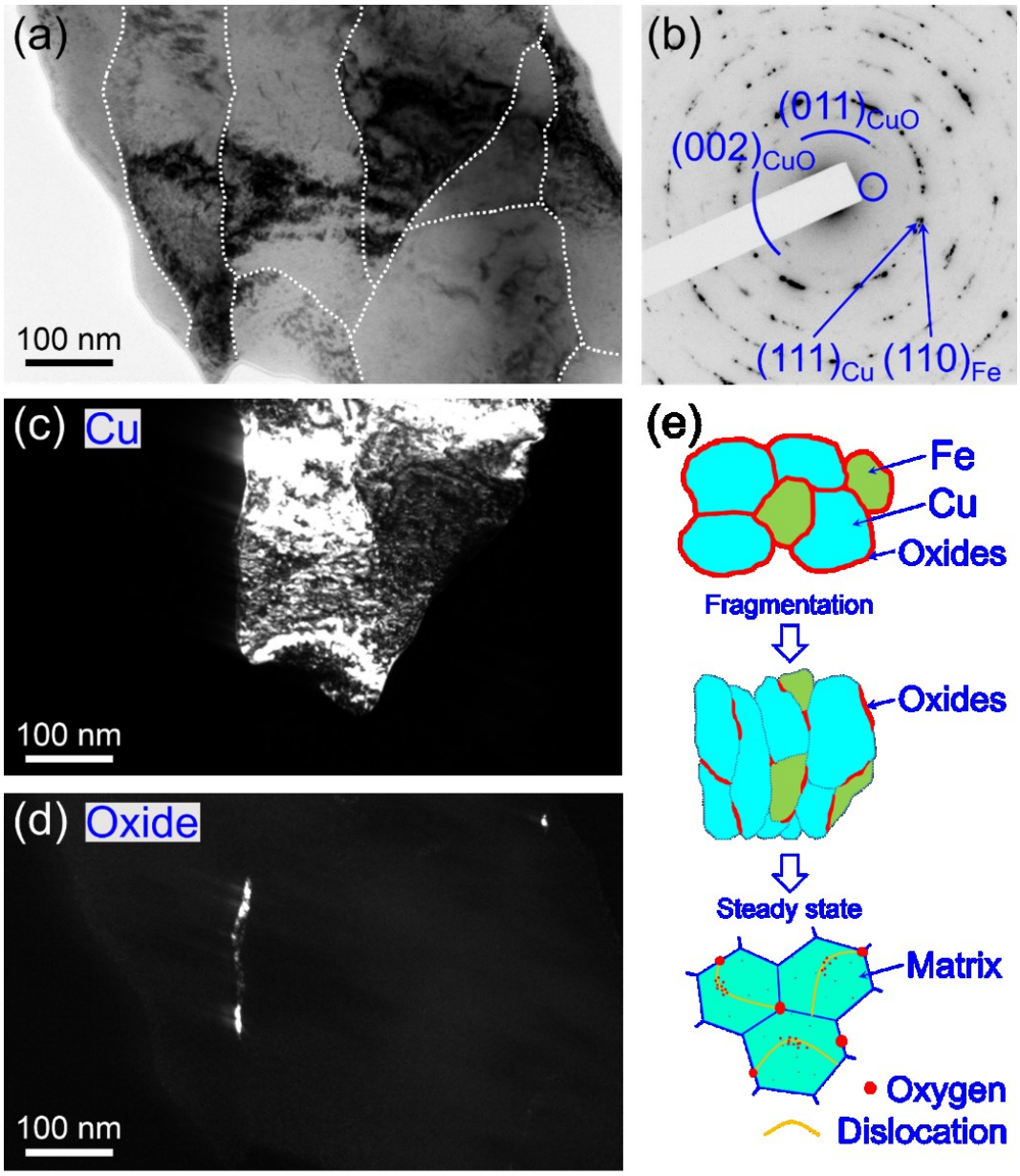

Fig. 4 Oxides' information of 75Cu-25Fe powder sample deformed with 5 rotations. (a) Bright-field TEM image. (b) Diffraction pattern corresponding to the area shown in (a). (c) Dark-field image of two neighboring Cu grains. (d) Dark-field image of Fe_2O_3 particles. (e) Schematic diagram of oxides' fragmentation and dissolution processes.

To summarize, in this study, the oxygen effects on nanocrystalline alloys have been systematically investigated. The Cu-Fe nanostructured alloys with different compositions are prepared by HPT from blended powders and arc-melted bulk, which possess different contents of oxygen. It is found that oxygen introduced during the powder pre-mixing can be partially dissolved into the matrix via extreme deformation. The residual proportion of oxygen enriched at grain boundaries can effectively facilitate the grain refinement predominantly by lowering grain boundary energy. The mechanisms of oxygen-mediated grain refinement in HPT deformed Cu-Fe powder samples are analyzed in detail for the first time. Grain boundary migration is the dominant mechanism in current alloys, assisted by the effects of SFE, solid solution hardening and "interstitial oxygen hardening". Largely decreased grain size is mainly responsible for increasing hardness and strength while deteriorating the ductility. In addition, what's more interesting is the finding of locally lowering SFE of nanocrystalline alloy by the interstitial oxygen atoms, which presents a guidance for the future design of materials via introducing controllable planar defects. Our findings show that the oxygen contamination introduced during powder processing is not always detrimental, and pose a promising route to manipulate the microstructures and properties of nanocrystalline alloys by intentionally incorporating oxygen into initial materials.

Methods

Sample deformation by high pressure torsion. The initial materials of nominal compositions of (100–x) at.%Cu - x at.%Fe (x = 0, 5, 15, 25, 35, abbreviated as (100–x)Cu-xFe) were mixed from Cu and Fe powders produced by Alfa Aesar (Karlsruhe, Germany) with purity of 99.95+% and generated by arc-melting process using Cu ingot (Goodfellow, Huntingdon, UK, purity 99.95%) and Fe rod (Alfa, Royston, UK, purity 99.99+%) respectively. The as-generated initial materials were then deformed by HPT with 100 rotations at room temperature accompanied by air cooling for the whole process.

X-ray diffraction and transmission electron microscopy characterizations. Lattice parameters of as-deformed materials were derived from X-ray diffraction profiles which were measured using a Smartlab X-ray diffractometer (Rigaku, Japan) with Cu $K_{\alpha 1}$ radiation (λ = 1.5406 Å). Field emission gun transmission electron microscope (TEM, JEOL JEM-2100F, Japan) equipped with an imaging spherical aberration corrector was employed to check the microstructures of as-deformed samples. All microstructural investigations in this work were undertaken at radius of 3.0 mm from the torsional axis of the HPT deformed disks.

Atom probe tomography characterization. APT measurements were conducted in a local electrode atom probe, LEAP 3000X HR™ from Cameca Instruments. The measurements were set up in laser mode with energy of 0.8 nJ and a pulse repetition rate of 250 kHz, base temperature of 60 K and a detection rate of 0.005 atom per pulse. The specimens were prepared by standard sample lift out and annular milling, using a focused ion beam (FIB) FEI Helios 600i Dual Beam workstation. A final cleaning of the tip with low ion energy of 3 kV ensured a Ga content in the analyzed volumes below 0.05 at. %.

Hardness measurements and tensile experiments. Vickers microhardness measurements were conducted on a Buehler Mircomet 5100 using a load of 500 g (HV0.5). Average values of six individual measurements at the same strain condition on deformed disks were reported in this work. Details of tensile testing specimen preparation, tensile loading and data evaluation can be referred to Ref. [51]. Fracture surfaces were examined by scanning electron microscope LEO Gemini 1525 (Carl Zeiss, Oberkochen, Germany).

Density-functional theory calculation procedures are presented in detail in Supplementary Information.

Acknowledgements

This work was financially supported by the Austrian Science Fund (FWF): No. P27034 - N20. The authors are grateful to Dr. Andrea Bachmaier and Dr. Christoph Gammer at Erich Schmid Institute of Materials Science, Austrian Academy of Sciences for conducting tensile experiments and recording diffraction contrast images.

Author Contributions

Z. Z. oversaw the whole project. J. G. conducted the experiments and wrote the manuscript with input from all authors. M.J. D. and G. D. carried out the APT characterization. Y. Z. performed theoretical calculations. J. G. and Z. Z. analyzed the experimental results. G. D and R. P. made helpful comments on the manuscript. All authors read through the manuscript and contributed to the discussions of the results.

Supplementary Information

Supplementary 1: APT result of bulk sample.

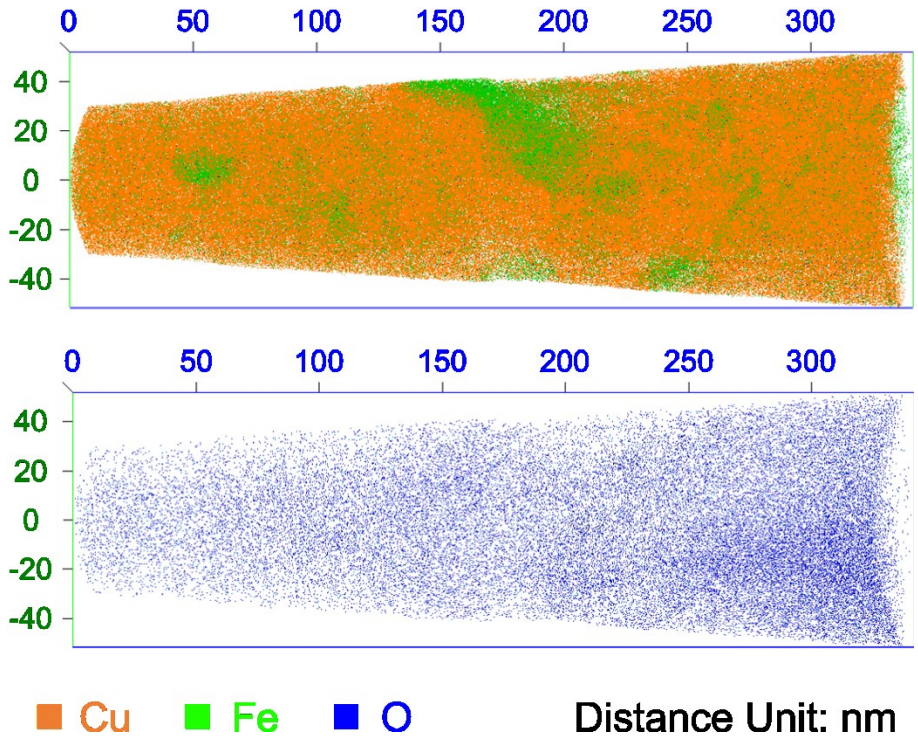

Fig. S1 APT results of annealed 75Cu-25Fe bulk sample. Upper image is an overview image containing Fe and O distributions, and the bottom image shows the O-rich distribution.

Oxygen clusters were not found in this bulk sample. The distribution of oxygen is similar in all regions. As the concentration of oxygen is very low and the background is high, the signal to noise ratio is below 2, making that a large amount of depicted oxygen comes also from the background signal. The quantified O content in bulk sample is about 0.047 at.%.

Supplementary 2: Mathematical model for calculating the probability of dislocation's hindering effect.

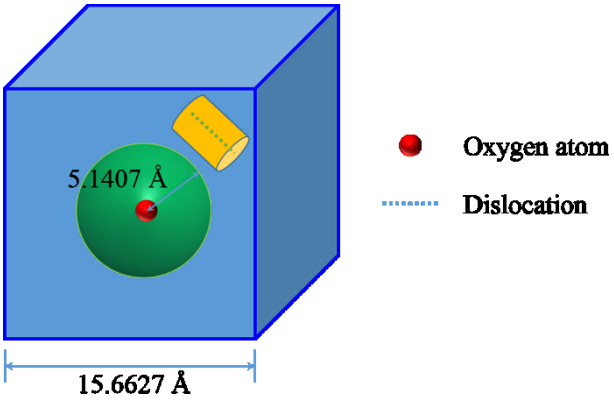

Fig. S2 A schematic diagram shows the oxygen's influence to the dislocation in a cell lattice with 320 atoms. The green sphere represents the influence region with the radius of a distance of two (110) lattice planes. The yellow cylinder is the sensing volume of an edge dislocation.

If the dissolved oxygen content is assumed to be 0.31 at.%, it is roughly equivalent to the concentration of 1 oxygen atom in a cell lattice with 320 matrix atoms. Considering that every *fcc* unit cell has 4 atoms, the above-mentioned cell lattice possesses 80 unit cells.

The length of the cell lattice: $\sqrt[3]{80} \times 3.6350\ \text{Å} = 15.6627\ \text{Å}$

Volume of the cell lattice: $(15.6627\ \text{Å})^3 = 3.8424\ \text{nm}^3$

The calculated dislocation density is $7.53 \times 10^{15}\ \text{m}^{-2}$, so the dislocation length in the cell lattice is $3.8424 \times 10^{-27}\ \text{m}^3 \times 7.53 \times 10^{15}\ \text{m}^{-2} = 28.9331 \times 10^{-12}\ \text{m} = 0.0289331\ \text{nm}$.

It can be calculated that the spacing of 2 (220) planes is 2.5703 Å = 0.25703 nm.

A dislocation's sensing volume: $\pi \times (0.25703\ \text{Å})^2 \times 0.0289331\ \text{nm} = 0.0060\ \text{nm}^3$

The whole cell lattice can be divided into $\frac{3.8424\ \text{nm}^3}{0.0060\ \text{nm}^3} = 640.4$ pieces.

An oxygen atom's influence volume: $\frac{4}{3} \times \pi \times (0.25703\ \text{nm})^3 = 0.0711\ \text{nm}^3$

This oxygen atom's influence volume can be $\frac{0.0711\ \text{nm}^3}{0.0060\ \text{nm}^3} = 11.9$ times of the dislocation's sensing volume.

So about $\frac{11.9}{640.4} = 1.9\%$ of dislocations can be influenced by the oxygen atoms.

Based on the same method, it can be estimated that an amount of 8.4 at.% oxygen needs to be dissolved into the matrix if 50% of dislocations will be hindered. Here it should be pointed out that two (220) atomic layers are considered in this model. If the oxygen atom can totally influence 4 (220) planes, the probability will increase to 14.8%.

Supplementary 3: Diffraction contrast images of 75Cu-25Fe sample deformed with 25 rotations.

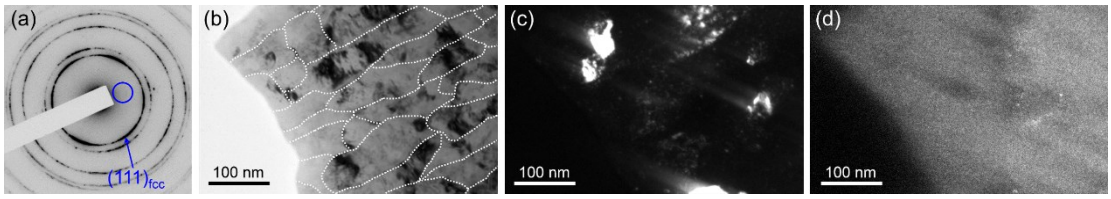

Fig. S3 (e) Diffraction patterns, (f) Bright-field image, (g) Dark-field image of Cu grains, (h) Dark-field image of oxides of 75Cu-25Fe powder samples after deformation of 25 rotations. The oxide particles can be barely detected after deformation of 25 rotations.

Supplementary 4: DFT calculation methods.

The DFT calculation method of SFE can be referred to [1,2].

The interaction energy E_{n-int} between SF and solute atom is defined as the variation in total energy of SF system when solute atom substituted at the nth layer with respect to the fault plane, and can be calculated as following:

$$E_{n\text{-}int} = (E_{solution\text{-}SF} - E_{solution\text{-}perfect}) - (E_{Cu\text{-}SF} - E_{Cu\text{-}perfect})$$

where $E_{solution-SF}$ and $E_{solution-perfect}$ are, respectively, the energies of Cu solid solution supercells with and without SFs, while E_{Cu-SF} and $E_{Mg-perfect}$ are the energies of supercells for pure Cu with and without SFs, respectively.According to the uniform distribution of solute atoms at the SF, the SFEs of Cu solid solutions are calculated by:

$$\gamma = \gamma_{Cu} + c_{SF}E_{SF\text{-}int}/A$$

where γ_{Cu}, E_{SF-int} and c_{SF} are the SFE of pure Cu, interaction energy for SF with the solute atom in the SF and concentration of solute atoms in the SF plane, respectively. A is the area of unit cell of basal plane.

Based on the interaction energy, the concentration c_n at the nth plane with respect to the fault plane can be obtained from Fermi–Dirac distribution function of solute:

$$c_n = \frac{1}{1 + \exp\left\{\left[E_{n\text{-}int} - kT \ln\frac{c_0}{1-c_0}\right]/kT\right\}}$$

with c_0 the nominal uniform concentration in the region where $E_{n-int} = 0$. Then the SFE of solid solution at finite temperature considering the concentration distribution of solutes can be calculated using:

$$\gamma = \gamma_{Cu} + \sum_{n} c_n E_{n\text{-}int}/A$$

Then the change of SFE $\Delta\gamma$ caused by solute atoms can be expressed as:

$$\Delta\gamma = \gamma\text{-}\gamma_{Cu} = \sum_{n} c_n E_{n\text{-}int}/A$$

The following description is the calculation method of lattice parameters using VASP.

Vienna Ab-initio Simulation Package (VASP) was employed to obtain the Cu lattice parameters with different oxygen contents. A supercell containing 32 Cu atoms is employed. 1 (3.03 at.%) oxygen atom and 2 oxygen atoms (5.88 at.%) were added to the octahedral sites of the supercell respectively. For each oxygen concentration, 5 different combinations of interstitial sites are considered. The shape and the atoms coordinates of the oxygen-contained supercell were both relaxed. The projector augmented wave (PAW) method [3] was used to treat the interaction between ion and core electrons. The valence electrons were described using the generalized gradient approximation (GGA) with the exchange-correlation function of Perdew, Burke and Ernzerhof (PBE) [4]. Convergence tests indicated that 600 eV was a suitable cutoff energy for the PAW potential to obtain sufficient precision in the current systems. Brillouin-zone gridding was performed using the Monkhorst-Pack method [5] with 7×7×7 k-point meshes, which were sufficient for structural optimization. Using the optimal parameters, the calculated formation enthalpy changes converge to better than 0.1 meV/atom.

References of Supplementary Information

1. Fan, T., Wei, L., Tang, B., Peng, L. & Ding, W. Effect of temperature-induced solute distribution on stacking fault energy in Mg-X (X = Li, Cu, Zn, Al, Y and Zr) solid solution: a first-principles study. *Philos. Mag.* **94**, 1578–1587 (2014).
2. Liu, L. H. et al. The possibilities to lower the stacking fault energies of aluminum materials investigated by first-principles energy calculations. *Comp. Mater. Sci.* **108**, 136–146 (2015).
3. Kresse, G. & Joubert, D. From ultrasoft pseudopotentials to the projector augmented-wave method. *Phys. Rev. B* **59**, 1758–1775 (1999).
4. Perdew, J. P., Burke, K. & Ernzerhof, M. Generalized gradient approximation made aimple. *Phys. Rev. Lett.* **77**, 3865–3868 (1996).
5. Monkhorst, H. J. & Pack, J. D. Special points for Brillouin-zone integrations. *Phys. Rev. B* **13**, 5188–5192 (1977).

References

1. Valiev, R. Z. et al. Fundamentals of superior properties in bulk nanoSPD materials. *Mater. Res. Lett.* **4**, 1–21 (2016).
2. Langdon, T. G. Twenty-five years of ultrafine-grained materials: achieving exceptional properties through grain refinement. *Acta Mater.* **61**, 7035–7059 (2013).
3. Bachmaier, A., Kerber, M., Setman, D. & Pippan, R. The formation of supersaturated solid solutions in Fe-Cu alloys deformed by high-pressure torsion. *Acta Mater.* **60**, 860–871 (2012).
4. Xia, K. & Wu, X. Back pressure equal channel angular consolidation of pure Al particles. *Scr. Mater.* **53**, 1225–1229 (2005).
5. Ma, E. Alloys created between immiscible elements. *Prog. Mater. Sci.* **50**, 413 (2005).
6. Raabe, D. et al. Grain boundary segregation engineering in metallic alloys: a pathway to the design of interfaces. *Curr. Opin. Solid St. M.* **18**, 253–261 (2014).
7. Rupert, T. J., Gianola, D. S., Gan, Y. & Hemker, K. J. Experimental observations of stress-driven grain boundary migration. *Science* **326**, 1686–1690 (2009).
8. Gianola, D. S., Mendis, B. G., Cheng, X. M. & Hemker, K. J. Grain-size stabilization by impurities and effect on stress-coupled grain growth in nanocrystalline Al thin films. *Mater. Sci. Eng. A* **483–484**, 637–640 (2008).
9. Tang, F., Gianola, D. S., Moody, M. P., Hemker, K. J. & Cairney, J. M. Observations of grain boundary impurities in nanocrystalline Al and their influence on microstructural stability and mechanical behaviour. *Acta Mater.* **60**, 1038–1047 (2012).
10. He, M. R. et al. Linking stress-driven microstructural evolution in nanocrystalline aluminium with grain boundary doping of oxygen. *Nat. Commun.* **7**, 11225 (2016).
11. Elsener, A., Politano, O., Derlet, P. M. & Swygenhoven, H. V. Variable-charge method applied to study coupled grain boundary migration in the presence of oxygen. *Acta Mater.* **57**, 1988–2001 (2009).
12. Hall, E. O. The deformation and ageing of mild steel: discussion of results. *Proc. Phys. Soc. B* **64**, 747–753 (1951).
13. Petch, N. J. The cleavage strength of polycrystals. *J. Iron Steel Inst.* **174**, 25–28 (1953).
14. Djaziri, S. et al. Deformation-induced martensite: a new paradigm for exceptional steels. *Adv. Mater.* **28**, 7753–7757 (2016).
15. Yu, Q. et al. Origin of dramatic oxygen solute strengthening effect in titanium. *Science* **347**, 635–639 (2015).
16. Bachmaier, A., Hohenwarter, A. & Pippan, R. New procedure to generate stable nanocrystallites by severe plastic deformation. *Scr. Mater.* **61**, 1016–1019 (2009).
17. Bachmaier, A. & Pippan, R. Effect of oxide particles on the stabilization and final microstructure in aluminium. *Mater. Sci. Eng. A* **528**, 7589–7595 (2011).
18. Guo, J. et al. In-situ atomic-scale observation of oxidation and decomposition processes in nanocrystalline alloys. *Nat. Commun.* Accepted, in press.
19. Sun, P. L. et al. Effect of stacking fault energy on strength and ductility of

nanostructured alloys: an evaluation with minimum solution hardening. *Mater. Sci. Eng. A* **525**, 83–86 (2009).

20. Zhao, Y. H., Horita, Z., Langdon, T. G. & Zhu, Y. T. Evolution of defect structures during cold rolling of ultrafine-grained Cu and Cu-Zn alloys: influence of stacking fault energy. *Mater. Sci. Eng. A* **474**, 342–347 (2008).

21. Cohen, J. B. & Wagner, C. N. J. Determination of twin fault probabilities from the diffraction patterns of fcc metals and alloys. *J. Appl. Phys.* **33**, 2073–2077 (1962).

22. Zhao, Y. H. et al. Simultaneously increasing the ductility and strength of ultra-fine-grained pure copper. *Adv. Mater.* **18**, 2949–2953 (2006).

23. Venables, J. A. Deformation twinning in face-centred cubic metals. *Philos. Mag.* **6**, 379–396 (1961).

24. Huang, C. X. et al. Deformation twinning in polycrystalline copper at room temperature and low strain rate. *Acta Mater.* **54**, 655–665 (2006).

25. Hahn, H., Mondal, P. & Padmanabhan, K. A. Plastic deformation of nanocrystalline materials. *Nanostruct. Mater.* **9**, 603–606 (1997).

26. Chang, C. I., Lee, C. J. & Huang, J. C. Relationship between grain size and Zener-Holloman parameter during friction stir processing in AZ31 Mg alloys. *Scr. Mater.* **51**, 509–514 (2004).

27. Wollmershauser, J. A. et al. An extended hardness limit in bulk nanoceramics. *Acta Mater.* **69**, 9–16 (2014).

28. Lu, K., Lu, L. & Suresh, S. Strengthening materials by engineering coherent internal boundaries at the nanoscale. *Science* **349**, 349–352 (2009).

29. Edalati, K. et al. Influence of dislocation-solute atom interactions and stacking fault energy on grain size of single-phase alloys after severe plastic deformation using high-pressure torsion. *Acta Mater.* **69**, 68–77 (2014).

30. Qin, E. W., Lu, L., Tao, N. R. & Lu, K. Enhanced fracture toughness of bulk nanocrystalline Cu with embedded nanoscale twins. *Scr. Mater.* **60**, 539–542 (2009).

31. Qin, E. W., Lu, L., Tao, N. R., Tan, J. & Lu, K. Enhanced fracture toughness and strength in bulk nanocrystalline Cu with nanoscale twin bundles. *Acta Mater.* **57**, 6215–6225 (2009).

32. Estrin, Y. & Vinogradov, A. Extreme grain refinement by severe plastic deformation: a wealth of challenging science. *Acta Mater.* **61**, 782–817 (2013).

33. Mohamed, F. A. & Dheda, S. S. On the minimum grain size obtainable by high-pressure torsion. *Mater. Sci. Eng. A* **558**, 59–63 (2012).

34. Zhao, Y. H., Liao, X. Z., Zhu, Y. T., Horita, Z. & Langdon, T. G. Influence of stacking fault energy on nanostructure formation under high pressure torsion. *Mater. Sci. Eng. A* **410–411**, 188–193 (2005).

35. Zhao, Y. et al. Influence of stacking-fault energy on microstructural characteristics of ultrafine-grain copper and copper-zinc alloys. *Acta Mater.* **56**, 809–820 (2008).

36. Huang, C. X. et al. The effect of stacking fault energy on equilibrium grain size and tensile properties of nanostructured copper and copper-aluminum alloys processed by

equal channel angular pressing. *Mater. Sci. Eng. A* **556**, 638–647 (2012).

37. Pippan, R. et al. Saturation of fragmentation during severe plastic deformation. *Annu. Rev. Mater. Res.* **40**, 319–343 (2010).

38. Bruder, E. et al. Influence of solute effects on the saturation grain size and rate sensitivity in Cu-X alloys. *Scr. Mater.* **144**, 5–8 (2018).

39. Mohamed, F. A. A dislocation model for the minimum grain size obtainable by milling. *Acta Mater.* **51**, 4107–4119 (2003).

40. Roy, B., Maity, T. & Das, J. Tuning of nanostructure by the control of twin density, dislocation density, crystallite size, and stacking fault energy in $Cu_{100-x}Zn_x$ ($0 \leq x \leq 30$ wt%). *Mater. Sci. Eng. A* **672**, 203–215 (2016).

41. Qu, S. et al. Microstructural evolution and mechanical properties of Cu-Al alloys subjected to equal channel angular pressing. *Acta Mater.* **57**, 1586–1601 (2009).

42. Ma, X. L. et al. Alloying effect on grain-size dependent deformation twinning in nanocrystalline Cu-Zn alloys. *Philos. Mag.* **95**, 301–310 (2015).

43. Shao, Q. Q., Liu, L. H., Fan, T. W., Yuan, D. W. & Chen, J. H. Effects of solute concentration on the stacking fault energy in copper alloys at finite temperatures. *J. Alloys Compd.* **726**, 601–607 (2017).

44. Liu, L. H. et al. The possibilities to lower the stacking fault energies of aluminum materials investigated by first-principles energy calculations. *Comp. Mater. Sci.* **108**, 136–146 (2015).

45. Fan, T., Wei, L., Tang, B., Peng, L. & Ding, W. Effect of temperature-induced solute distribution on stacking fault energy in Mg-X (X = Li, Cu, Zn, Al, Y and Zr) solid solution: a first-principles study. *Philos. Mag.* **94**, 1578–1587 (2014).

46. Scheriau, S., Zhang, Z., Kleber, S. & Pippan, R. Deformation mechanisms of a modified 316L austenitic steel subjected to high pressure torsion. *Mater. Sci. Eng. A* **528**, 2776–2786 (2011).

47. Labusch, R. Statistical theories of solid solution hardening. *Acta Metall.* **20**, 917–927 (1972).

48. Gammer, C., Ozdol, V. B., Liebscher, C. H. & Minor, A. M. Diffraction contrast imaging using virtual apertures. *Ultramicroscopy* **155**, 1–10 (2015).

49. Gibbs, J. W. The collected works of J.W. Gibbs. Longmans, Green and Co. (1928).

50. Millett, P. C., Selvam, R. P., Saxena, A. Stabilizing nanocrystalline materials with dopants. *Acta Mater.* **55**, 2329–2336 (2007).

51. Rathmayr, G. B., Bachmaier, A. & Pippan, R. Development of a new testing procedure for performing tensile tests on specimens with sub-millimetre dimensions. *J. Test. Eval.* **41**, 635–646 (2013).